

Markovian transport through few-level quantum systems

vorgelegt von
Diplom-Physiker
Christian Nietner
aus Eberswalde

Von der Fakultät II - Mathematik und Naturwissenschaften
der Technischen Universität Berlin

zur Erlangung des akademischen Grades

Doktor der Naturwissenschaften

— **Dr. rer. nat.** —

genehmigte Dissertation

Promotionsausschuss

Vorsitzender: Prof. Dr. rer. nat. Otto Dopfer
1. Gutachter: Prof. Dr. rer. nat. Tobias Brandes
2. Gutachter: Prof. Dr. rer. nat. Andreas Wacker

Tag der wissenschaftlichen Aussprache: 24.01.2014

Berlin 2014

D 83

*This dissertation is lovingly dedicated to my mother
Petra Rudolph. Her support, encouragement, and
constant love have sustained me throughout my life.*

Table of contents

Kurzzusammenfassung	ix
Abstract	xi
1 Introduction	1
1.1 Mesoscopic solid-state systems	1
1.2 Trapped ultracold gases	3
1.3 Structure of the thesis	5
2 Open quantum systems in nonequilibrium	7
2.1 System-bath Hamiltonian	8
2.2 Interaction picture	9
2.3 Born approximation	11
2.4 Markov approximation	13
2.5 Secular approximation	14
2.6 Lindblad master equation	15
2.7 Effective rate equation	17
2.8 Liouville space	18
2.9 Multi-terminal setups	20
2.10 Conditioned master equation	21
2.11 Full counting statistics	24
2.12 Steady-state currents	25
2.13 Entropy production	27
2.14 Onsager theorem	30
2.14.1 Constant chemical potential	30
2.14.2 Temperature and density dependent chemical potential	33
3 Interacting transport qubits	39
3.1 System Hamiltonian	40
3.2 Liouvillian	44
3.3 Transport characteristics	45
3.3.1 Full transport characteristics	46
3.3.2 Ultra-strong Coulomb blockade regime	49
3.3.2.1 High-bias currents	51

Table of contents

3.3.3	Strong Coulomb blockade regime	53
3.3.3.1	High-bias currents	54
3.3.4	Current anti-correlation	54
3.3.5	Coulomb diamond gaps	56
3.4	Preparation of pure states	58
3.4.1	Purity of the full system	59
3.4.2	Purity of the charge-qubit	61
3.5	Entanglement	63
3.5.1	Eigenstate concurrence	64
3.5.2	Generalized transport concurrence	66
4	Transport with ultracold atoms	67
4.1	Ideal quantum gases at constant density	68
4.1.1	Grand-canonical chemical potential	69
4.1.2	Bose-Einstein condensation	73
4.2	Transport with ultracold fermions	76
4.2.1	Transport system	76
4.2.2	Liouvillian	79
4.2.3	Steady-state currents	80
4.2.4	Linear transport coefficients	85
4.2.4.1	Matter conductance	86
4.2.4.2	Heat conductance	88
4.2.4.3	Thermopower	90
4.2.4.4	Thermodynamic performance	93
4.3	Transport with ultracold bosons	96
4.3.1	Transport system	96
4.3.2	Liouvillian	99
4.3.3	Steady-state currents	100
4.3.4	Linear transport coefficients	103
4.3.4.1	Matter conductance	104
4.3.4.2	Heat conductance	106
4.3.4.3	Thermopower	108
4.3.4.4	Thermodynamic performance	110
5	Summary	115
	Bibliography	117
	Acknowledgements	135
	List of figures	134

Kurzzusammenfassung

In der vorliegenden Dissertation wird der Markov'sche quantenmechanische Mastergleichungsansatz benutzt, um die Transporteigenschaften unterschiedlicher experimenteller Aufbauten zu untersuchen.

Motiviert durch die Suche nach möglichen physikalischen Implementierungen die Quanteneigenschaften für zukünftige Maschinen zur Quanteninformationsverarbeitung und Quantenkommunikation nutzbar machen können, untersuchen wir zunächst ein spezielles System aus Quantenpunkten, dass als Basis für solche Apparaturen dienen könnte. Bei der industriellen Produktion großflächiger Strukturen lässt sich jedoch das Auftreten ungewollter Defekte kaum vermeiden. Daher untersuchen wir speziell den Fall von elektronischem Transport durch zwei parallele Doppelquantenpunkte, die sowohl kapazitiv, als auch durch ein senkrecht zwischen ihnen liegendem Ladungsqubit gekoppelt sind. Dieses Ladungsqubit repräsentiert dabei einen ungewollten Defekt in einer regelmäßigen Struktur aus Doppelquantenpunkten, welcher die kohärenten Tunnelamplituden der Doppelquantenpunkte modifiziert. In der Folge, studieren wir den Einfluss des Qubits auf die stationären Ströme durch das System, die Verschränkung der Doppelquantenpunkte und deren Rückwirkung auf das Ladungsqubit. Ein Resultat dieser Untersuchung, ist die Beobachtung eindeutiger Signaturen des Ladungsqubits in den stationären Strömen. Zusätzlich finden wir, dass der stationäre Qubitzustand durch extern angelegte Spannungen justiert werden kann und sowohl reine Qubitzustände als auch reine, verschränkte Doppelquantenpunktzustände erzeugt werden können.

Angeregt durch die eindrucksvollen Fortschritte in der Produktion und Manipulation kalter Atome und dem im bosonischen Fall auftretenden kritische Phänomen der Bose-Einstein Kondensation, untersuchen wir zusätzlich die Transporteigenschaften eines Aufbaus, bei dem Bäder aus ultrakalten bosonischen und fermionischen Teilchen an ein Quantensystem mit nur wenigen Energieniveaus gekoppelt sind. Um das kritische Verhalten in den Bädern korrekt beschreiben zu können, leiten wir zunächst das temperatur- und dichteabhängige chemische Potential der Reservoirs im großkanonischen Ensemble ab. Anschließend bestimmen wir die stationären Ströme durch das System unter Berücksichtigung dieser abhängigen chemischen Potentiale. Sowohl im Falle fermionischer als auch bosonischer Teilchen beobachten wir stationäre Ströme die gegen den externen Temperaturgradienten zwischen den Bädern fließen. Zur weiteren Charakterisierung dieser Ströme stellen wir das linearisierte Onsager-Gleichungssystem auf und berechnen die linearen Transportkoeffizienten. Diese Koeffizienten zeigen im Fall des bosonischen Transportes eindeutige Signaturen der Bose-Einstein-Kondensation.

Abstract

In this thesis we first review the Markovian quantum master equation approach and its underlying theoretical arguments and, subsequently, utilize it in order to investigate two different transport setups.

On the one hand, motivated by the ongoing search for physical implementations of possible information processing or communication devices which can harness quantum mechanical properties, we first investigate a candidate for a basic building block of such a machine based on quantum dots. Large-scale structures of many such quantum dots have been suggested as fundamental architecture for quantum computers. However, a large-scale industrial production is likely to face the problem of unwanted defects. Therefore, we particularly study the electronic transport through a system of two parallel double quantum dots coupled both capacitively and via a perpendicularly aligned charge-qubit. We assume that the presence of the qubit leads to a modification of the coherent tunneling amplitudes of each double-quantum dot. Subsequently, we study the influence of the qubit on the electronic steady-state currents through the system, the entanglement between the transport double quantum dots, and the back action on the charge-qubit. As a result we find that the obtained steady-state currents show signatures of the qubit. Additionally, the stationary qubit state may be tuned and even rendered pure by applying suitable voltages and we find that it is also possible to stabilize pure entangled states of the transport double-quantum dots in the Coulomb diamonds.

On the other hand, motivated by impressive advances in the field of ultra-cold atoms and the phenomenon of Bose-Einstein condensation, we also study transport setups, where reservoirs of massive fermionic or bosonic particles are in contact with a few-level quantum system. In order to resolve a potentially critical behavior in these atomic reservoirs, we review the properties of ultra-cold quantum gases in the grand-canonical ensemble and derive their temperature- and density-dependent chemical potentials. Consequently, we calculate the steady-state particle and energy currents through the system. Considering ideal Fermi and Bose gas reservoirs, we observe steady-state currents against the thermal bias as a result of the non-linearities introduced by the constraint of a constant particle density in the reservoirs. Applying a linear response argument, we establish the corresponding Onsager system of equations from which we are able to extract the transport coefficient that characterizes the steady-state currents. Most importantly, we find signatures of the on-set of Bose-Einstein condensation in the transport coefficients of the bosonic setup.

Chapter 1

Introduction

Transport processes, where energy and/or matter is exchanged between connected subsystems, are very widespread and commonly occur in many fields of physics, e.g., nonequilibrium thermodynamics [1], of chemistry, e.g., reaction-diffusion systems [2] and of biology, e.g., biological metabolism processes [3]. Ever since their discovery they have drawn the attention of both theorists and experimentalists, who try to gain a better insight into the laws of nature, and, based on their research, develop new applications. In fact, the advances over the last decades have considerably deepened our knowledge of the underlying physical mechanisms and allowed us to strongly improve the experimental capabilities to model such systems. Especially, these technical improvements have allowed not only to study macroscopic systems but to design systems of smaller and smaller dimensions. Nowadays, one can routinely produce and manipulate systems with dimensions of the order of a few nanometers, a length scale comparable to the size of a few atoms or molecules, the wavelength of visible light, or the wavelength of the electron envelope wave function in semiconductors [4]. Consequently, the transport processes through such tiny structures are affected by their quantum properties which can not be neglected any longer. Therefore, quantum transport in contrast to the classical transport incorporates quantum effects such as superposition of states, interference, entanglement, nonlocality and uncertainty. The fundamentally different nature of quantum systems compared to classical systems has raised an immense interest and lead to a complete new field of physics, namely the study of mesoscopic transport through open quantum system.

1.1 Mesoscopic solid-state systems

Most prominent examples for experimental systems where quantum transport can be observed are mesoscopic solid-state systems like quantum wells [5], quantum dots [6–8], nanowires / nanotubes [9–11], nanocrystals [12] or optical microcavities [13], to name but a few. We especially point out the systems defined in two-dimensional electron-gases (2DEG) which are generated in doped semiconductors. They can be used to define a wide range of different quantum dot setups. To this

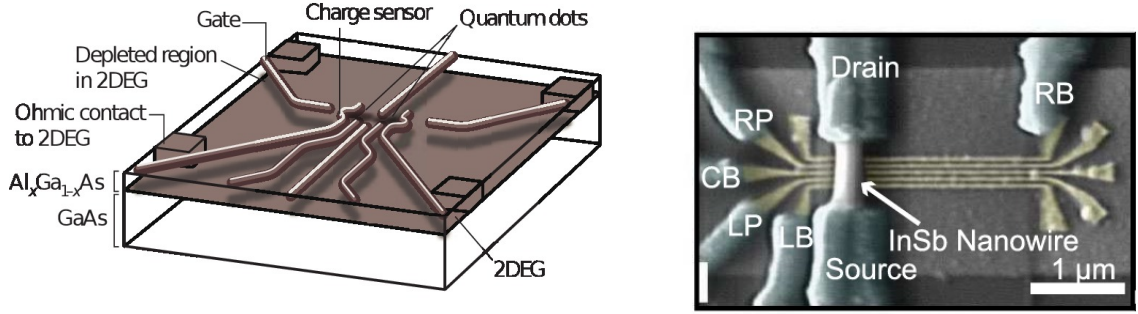


Figure 1.1: Left picture taken from Ref. [18]: Metallic surface gates deplete the 2DEG in the semiconductor substrate and define a DQD in the central region. Additional gates on the left and right side of the DQD define QPCs as charge sensors. Right picture taken from Ref. [11]: InSb nanowire hanging between metallic source and drain leads. The metallic gates LB, CB, and RB below the beam define a DQD within the nanowire. Additionally, one can tune the electron number in each dot via the gates LP and RP.

end, one usually applies additional metallic surface gates on top of the semiconductor substrate containing the 2DEG, as can be seen in Fig. 1.1. Applying a voltage to these additional gates locally depletes the 2DEG and, thus, enables one to define almost arbitrary nanostructures within the 2DEG such as single quantum dots (QD), quantum-point contacts (QPC) [14, 15], double-quantum dots (DQD) [16–18], triple-quantum dots [19, 20] or even more complicated structures. Furthermore, the afore mentioned transport systems allow for a high degree of control over all relevant system parameters, due to their tuneability via the external gates. Other methods which are used nowadays to produce quantum dots on a large scale are, for example, lithographic methods [21–23] or self-assembled growth [12].

Based on these experimental advances a multitude of new effects and applications have been developed over the recent decades. They cover a wide field reaching from single electron-, spin- and photon-sources [24, 25], detectors [26–28], sources of entangled electrons [29], to many-body quantum simulators [30–32] and artificial atoms and molecules [33]. Especially the capability to harness the potential power of quantum properties, such as superposition of states and entanglement, for quantum information and communication technologies [34–36], has raised the interest in such experimental implementations. Encouraged by the latest progress in their fabrication and manipulation, semiconductor quantum dots have been proposed as possible candidates [37, 38]. Scalability, the feasibility of coherent control, and non-destructive read out of quantum states, as well as robustness against decoherence are among the key features for such candidates [39, 40].

For these reasons double quantum dots [41], which are used to model two-level qubit states [42–44], are of special interest. It has been shown that coherent control

[33, 45–47] and read out [28, 48, 49] are achievable in these systems. Together, this allows to implement electronically accessible quantum gates based on quantum dots [35, 36, 50]. Even entanglement, which is crucial for quantum computation, can be produced [27], manipulated [51] and detected [52, 53] in several quantum-dot setups. In consequence, quantum dots provide a promising candidate for a quantum computation architecture [54].

Unfortunately, all these fabrication methods can not completely avoid unwanted defects that might destroy the desired properties of the double quantum dots. This problem inspired some recent studies of the effects of impurities in such systems. The effects of charge impurities on coupled quantum-dot systems have been recently studied theoretically using molecular orbital and configuration interaction methods [55]. Furthermore, the possibility of screening charge impurities by using multi-electron quantum dots were theoretically investigated [56]. In addition, spin impurities have been observed experimentally via transport spectroscopy in a carbon nanotube DQD [57].

However, more research is still necessary in order to pave the way to scalable quantum dot systems, which could be used in large scale quantum communication and quantum information devices. This is our motivation to study another kind of elementary defect which is commonly present in a large scale production of mesoscopic solid-state systems, namely charge-qubit (CQB) impurities. In contrast to the static charge impurity studied in Ref. [55], this defect also possesses a dynamical degree of freedom that introduces coherences in the impurity states. The dynamical behavior of the charge in the defect region can influence the properties of nearby quantum dot structures. Therefore, having possible quantum computation devices in mind, we investigate the influence of such a CQB impurity on a system of coupled parallel DQDs. We especially consider its effect on the entanglement properties of the DQDs since entanglement provides a valuable resource for quantum computation [58, 59].

1.2 Trapped ultracold gases

Parallel to the advances in the production and control of mesoscopic solid-state systems, there also has been a lot of progress in the production and manipulation of trapped ultracold quantum gases. Here, a cloud of massive particles is held in a magneto-optical trap in a ultrahigh vacuum chamber and subsequently is cooled down to ultracold temperatures, just a few nano-Kelvin above absolute zero. Depending on the density of the cloud, in this low temperature regime the de Broglie wavelength of the massive particles can become of the same order as their mean free path. Hence, the quantum properties of the particles become relevant, as it has been impressively shown by the Nobel Prize awarded creation of the first Bose-Einstein condensate (BEC) of cold atoms [60–62]. In order to give an impression of the formation of a Bose-Einstein condensate, we show some experimental data

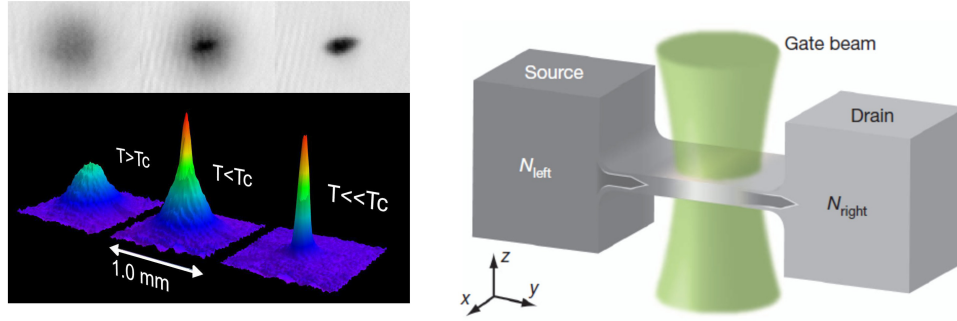


Figure 1.2: Left picture taken from Ref. [61]: Formation of a Bose-Einstein condensate of bosonic atoms below a critical temperature T_c in the velocity-distribution of the particles. The upper row shows the experimentally observed absorption images. Right picture taken from Ref. [84]: Sketch of a transport setup for ultracold particles. Two particle reservoirs with different temperatures are connected by a quasi 2D channel. The particle flow through the channel can be tuned by an external gate laser-beam. The channel itself is defined by a laser TEM mode (not shown) applied perpendicular to the gate beam.

obtained in the group of W. Ketterle in the left picture of Fig. 1.2.

This groundbreaking experiment has initiated an intense research of the properties of ultracold gases and especially BECs in different setups. For example, one has investigated the interference of BEC clouds [63, 64], rotating BECs [65, 66], spinor condensates [67], Bose-Fermi mixtures [68] and probed the properties of BECs in zero gravity [69]. Furthermore, it boosted the development of new techniques for the manipulation and control of three-dimensional (3D) cold gases using standing light fields. Here, counter propagating laser fields generate a standing electromagnetic wave pattern which interacts with the ultracold atoms. This method allows to superpose various structures on the particle cloud with a very high degree of control. An example is the realization of cold bosonic [70, 71] and fermionic [72] atoms trapped in optical lattices which allow for a simulation of many-body systems with Hubbard-like dynamics [73]. Since their experimental realization, optical-lattice systems have been used to successfully study, e.g., the entanglement of atoms [74, 75], quantum teleportation [76], Bell state experiments [77], disorder [78–81] or ultra cold molecules [82, 83].

In fact, after these systems have been studied in quasi equilibrium situations for quite a while and with huge success nowadays the focus shifts to investigating the nonequilibrium properties of such systems. The good experimental control of the relevant parameters, as well as the possibility to produce different lattice geometries in 1D, 2D or 3D, make these kind of systems an interesting candidates for quantum-transport setup.

First attempts successfully induced diffusive processes in the closed setup without additional reservoirs by introducing density inhomogeneities, i.e., disorder [80, 85] or local losses [86–88], applying a potential gradient via the optical lattice [89, 90], distortion [91] or displacement [92] of the confining potential, using interactions within the system [93, 94] or by external driving [95, 96]. Accompanying this experimental advances, there has been also theoretical research [97–101] predicting different interesting effects that might soon be observable experimentally.

More recently there have been first investigations of transport experiments with ultra cold fermionic and bosonic atoms that explicitly involve additional particle reservoirs as sketched in the right picture of Fig. 1.2. In these setups, the transport processes are driven by at least two reservoirs which are initialized in different equilibrium states and attached to the system of interest, e.g., a lattice system [102], a potential trap [103–106] or even quantum dot systems [107].

An interesting feature of this approach is the fact that the reservoirs themselves can possess critical quantum properties and, for example, undergo a phase transition to an BEC. However, in order to correctly model this critical behavior, especially for the case of bosonic particles, the chemical potential can not be treated as a free parameter but becomes a function of the temperature and particle number in the trap [108].

1.3 Structure of the thesis

We start this dissertation by presenting the fundamental theoretical concepts which we use throughout this thesis in Chap. 2. Here, we show that the transport setups discussed in Sec. 1.1 and Sec. 1.2 can be described by Markovian master equations under the assumption of weak system-bath couplings. Subsequently, we use these master equations to calculate the steady-state of the system from which we derive several interesting steady-state properties such as the particle current, transport coefficients and the entropy production.

In Chap. 3 we apply this theoretical formalism to a setup of two coupled parallel DQDs that are disturbed by an additional CQB. We investigate the steady-state currents through the DQD. In particular, we focus on the effect of the CQB impurity on the purity of the system and its entanglement properties.

In Chap. 4 we apply the theoretical formalism from Chap. 2 to a transport setup for ultracold atoms. Here, we consider two, either fermionic or bosonic, particle reservoirs which are connected to a few-level quantum system. In order to correctly describe the particle reservoirs, we review the properties of ultracold quantum gases in the grand-canonical ensemble. Subsequently, we investigate the steady-state transport properties of the setups. We particularly study the difference between fermionic and bosonic transport through such systems and especially focus on the signatures of a critical behavior in the reservoirs.

Finally, we summarize our results within Chap. 5.

Chapter 2

Open quantum systems in nonequilibrium

Within this chapter, we review the system-bath theory under a weak coupling assumption. The results and derivations presented herein provide the basic theoretical framework we use throughout this thesis.

The main idea behind the system-bath theory (see, e.g., [109]) is to divide a given thermodynamic system into two parts. One part is the system in whose dynamics one is interested. The other part is the environment in whose dynamics one is usually not so interested. In general, the small system will have considerably less degrees of freedom than the environment. In fact, we will often treat the environment in the thermodynamic limit which assumes an infinitely large volume V filled with infinitely many particles N under the constraint that the particle density $n = N/V$ remains constant.

The environment is usually coupled to the system by some matter- or energy-exchange processes. Hence, it can act as a reservoir providing particles and energy to the system. This fact makes it in general more difficult to extract the system dynamics of interest as they tend to be influenced by the reservoir. One possibility to analyze the influence of the environment on the system in a controlled way is to apply a perturbation theory in the system-bath interaction. For a sufficiently weak coupling one can truncate the perturbation series at low orders. Such approaches are called weak coupling approximations. They have been proven to be very successful since in many experimental setups one can isolate the system of interest quiet well from its surrounding. Furthermore, one can in principle include higher orders of the perturbation series which results in corrections to the weak coupling limit.

Unfortunately, analyzing a given setup by means of a perturbation theory can still be very complicated. To obtain analytic or numeric results one might need further

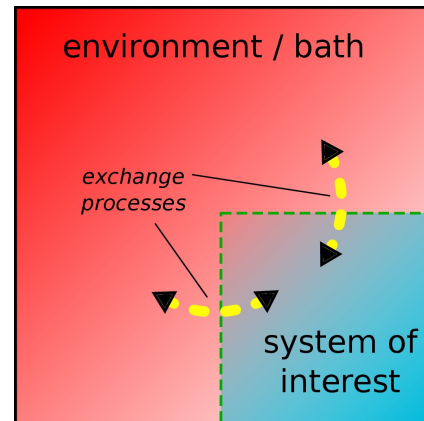


Figure 2.1: Sketch of the system-bath decomposition.

approximations regarding the system and/or the environment. Within this chapter, we derive a master equation in the weak coupling limit which describes the reduced system dynamics of a few-level quantum system coupled to multiple reservoirs. In order to establish this weak coupling approach, we need the so-called Born, Markov and secular approximations which we derive in the following sections.

Note that throughout this thesis we make use of the natural units. Therefore, we set in the following $c = k_B = \hbar = 1$.

2.1 System-bath Hamiltonian

In the spirit of the system-bath theory, we assume that the whole Hamiltonian of a given setup can be written as a sum

$$\hat{\mathcal{H}} = \hat{\mathcal{H}}_S + \hat{\mathcal{H}}_I + \hat{\mathcal{H}}_B. \quad (2.1)$$

The small system of interest is described by the Hamiltonian $\hat{\mathcal{H}}_S$ which we assume to be diagonalizable in a suitable basis such that

$$\hat{\mathcal{H}}_S |n\rangle = E_n |n\rangle, \quad (2.2)$$

with eigenvector $|n\rangle$ and corresponding eigenvalue E_n . Thus, a general system state is described by the density matrix $\hat{\rho}_S = \sum_n p_n |n\rangle \langle n|$ which is normalized such that $\text{Tr} \{\hat{\rho}_S\} = 1$. Here, the coefficients p_n represent the probability to find the system in the eigenstate $|n\rangle$.

The system is coupled to the surrounding bath, described by the Hamiltonian $\hat{\mathcal{H}}_B$, via the interaction Hamiltonian $\hat{\mathcal{H}}_I$. We assume that the reservoir is in a grand-canonical thermal equilibrium state

$$\bar{\rho}_B = \frac{e^{-\beta(\hat{\mathcal{H}}_B - \mu \hat{N}_B)}}{\text{Tr} \left\{ e^{-\beta(\hat{\mathcal{H}}_B - \mu \hat{N}_B)} \right\}}, \quad (2.3)$$

which is characterized by the inverse temperature $\beta = 1/T$ and the chemical potential μ . The operator \hat{N}_B is the total number operator of the particles in the bath. Obviously, when $[\hat{\mathcal{H}}_B, \hat{N}_B] = 0$, this density matrix commutes with the bath Hamiltonian, i.e., $[\hat{\mathcal{H}}_B, \bar{\rho}_B] = 0$, as expected for an equilibrium state.

For completeness, we also mention that a general state of the whole system, i.e., the system of interest plus the surrounding bath, is given by the corresponding density matrix

$$\hat{\chi} = \sum_j c_j |\psi_j\rangle \langle \psi_j|. \quad (2.4)$$

From this density matrix one could in principle obtain the evolution of the whole system and calculate all desired expectation values. However, the states $|\psi_j\rangle$ involving both system and bath are usually very hard to find due to the large amount of the bath degrees of freedom involved. Thus, in general one has to rely on approximation methods.

2.2 Interaction picture

A systematic approximation method which describes the transport through the few-level system, starts by considering the dynamics of the full density matrix $\hat{\chi}$. To describe its evolution, we first note that the eigenstates $|\psi_j\rangle$ evolve according to the Schrödinger equation

$$i \frac{\partial}{\partial t} |\psi_j\rangle = \hat{\mathcal{H}} |\psi_j\rangle. \quad (2.5)$$

From this observation and the definition of the density matrix in Eq. (2.4) follows that the evolution of the density matrix is described by the Liouville-von-Neumann equation

$$i \frac{\partial}{\partial t} \hat{\chi} = [\hat{\mathcal{H}}, \hat{\chi}]. \quad (2.6)$$

Assuming that we can diagonalize the system and bath Hamiltonians separately, it is convenient to switch to the Dirac interaction picture. Then, the evolution of the now explicitly time dependent density matrix is only governed by the interaction Hamiltonian. This structure allows to derive a perturbation series in powers of the interaction Hamiltonian.

The density operator in the Dirac interaction picture is obtained via a unitary transformation and reads as

$$\hat{\chi}(t) = e^{+i(\hat{\mathcal{H}}_S + \hat{\mathcal{H}}_B)t} \hat{\chi}(0) e^{-i(\hat{\mathcal{H}}_S + \hat{\mathcal{H}}_B)t}. \quad (2.7)$$

Here and in the following sections, we denote operators in the interaction picture by bold characters. The transformed density matrix from Eq. (2.7) now obeys the Liouville-von-Neumann equation in the interaction picture

$$\frac{\partial}{\partial t} \hat{\chi}(t) = -i [\hat{\mathcal{H}}_I(t), \hat{\chi}(t)]. \quad (2.8)$$

In order to proceed further, we need to assume a specific structure of the interaction Hamiltonian. A quite general structure of this Hamiltonian can be obtained if we suppose that it is composed of a sum over direct products of system and bath operators, respectively. Hence, we define the interaction Hamiltonian as

$$\hat{\mathcal{H}}_I = \sum_{\alpha} \hat{A}_{\alpha} \otimes \hat{B}_{\alpha}, \quad (2.9)$$

where the system operators \hat{A}_α and the bath operators \hat{B}_α act on their respective Hilbert spaces only. Here, we want to point out that the hermiticity of the interaction Hamiltonian $\hat{\mathcal{H}}_I = \hat{\mathcal{H}}_I^\dagger$ imposes some restrictions on the system and bath operators. Splitting these operators into hermitian and anti-hermitian parts

$$\hat{A}_\alpha = \hat{A}_\alpha^H + \hat{A}_\alpha^A, \quad \text{and} \quad \hat{B}_\alpha = \hat{B}_\alpha^H + \hat{B}_\alpha^A, \quad (2.10)$$

with

$$\hat{A}_\alpha^H = \frac{1}{2} (\hat{A}_\alpha + \hat{A}_\alpha^\dagger), \quad \hat{A}_\alpha^A = \frac{1}{2} (\hat{A}_\alpha - \hat{A}_\alpha^\dagger), \quad (2.11)$$

$$\hat{B}_\alpha^H = \frac{1}{2} (\hat{B}_\alpha + \hat{B}_\alpha^\dagger), \quad \hat{B}_\alpha^A = \frac{1}{2} (\hat{B}_\alpha - \hat{B}_\alpha^\dagger), \quad (2.12)$$

respectively, leads to

$$\hat{\mathcal{H}}_I = \frac{1}{2} (\hat{\mathcal{H}}_I + \hat{\mathcal{H}}_I^\dagger) = \sum_\alpha (\hat{A}_\alpha^H \otimes \hat{B}_\alpha^H - i \hat{A}_\alpha^A \otimes i \hat{B}_\alpha^A). \quad (2.13)$$

For an anti-hermitian operator \hat{O}^A we have $(\hat{O}^A)^\dagger = -\hat{O}^A$ and, thus, we see that $(i\hat{O}^A)^\dagger = i\hat{O}^A$ is hermitian. This allows us to always redefine the system and bath operators in terms of hermitian operators

$$\tilde{A}_\alpha = \hat{A}_\alpha^H, \quad \tilde{B}_\alpha = \hat{B}_\alpha^H. \quad (2.14)$$

Therefore, we can safely assume in the following, that the interaction Hamiltonian consists of hermitian system and bath operators

$$\hat{\mathcal{H}}_I = \sum_\alpha \hat{A}_\alpha \otimes \hat{B}_\alpha = \sum_\alpha \tilde{A}_\alpha \otimes \tilde{B}_\alpha = \sum_\alpha \tilde{A}_\alpha^\dagger \otimes \tilde{B}_\alpha^\dagger \quad (2.15)$$

In fermionic systems one usually needs to perform an additional Jordan-Wigner transformation of the annihilation and creation operators to establish an interaction Hamiltonian of the form assumed in Eq. (2.9) (see Sec. 3.2). This decomposition yields for the interaction Hamiltonian in the Dirac picture the expression

$$\hat{\mathcal{H}}_I(t) = \sum_\alpha e^{i\hat{\mathcal{H}}_S t} \hat{A}_\alpha e^{-i\hat{\mathcal{H}}_S t} \otimes e^{i\hat{\mathcal{H}}_B t} \hat{B}_\alpha e^{-i\hat{\mathcal{H}}_B t} \quad (2.16)$$

$$= \sum_\alpha \hat{\mathbf{A}}_\alpha(t) \otimes \hat{\mathbf{B}}_\alpha(t). \quad (2.17)$$

Note that the system and bath operators are transformed in the interaction picture by an unitary transformation with respect to their corresponding Hamiltonian only. Now, we can proceed and formally integrate the Liouville-von-Neumann equation in Eq. (2.8) which results in

$$\hat{\chi}(t) = \hat{\chi}_0 - i \int_0^t dt' [\hat{\mathcal{H}}_I(t'), \hat{\chi}(t')], \quad (2.18)$$

with the initial density matrix $\hat{\chi}_0 = \hat{\chi}(0)$. Thus, we obtain the time dependent density matrix of the whole system in the Dirac picture. However, usually one is interested in the dynamics of the system only. To obtain an expression for the time dependent system density matrix only, we introduce the partial trace $\text{Tr}_B \{\bullet\}$ over the bath degrees of freedom. Applying this partial trace to the total density operator leads to the reduced system density matrix

$$\hat{\rho}(t) = \text{Tr}_B \{\hat{\chi}(t)\}. \quad (2.19)$$

Reinserting the formal solution from Eq. (2.18) together with the von-Neumann equation in Eq. (2.8) in the above definition of the reduced system density matrix yields

$$\frac{\partial}{\partial t} \hat{\rho}(t) = -i \text{Tr}_B \{[\hat{\mathcal{H}}_I(t), \hat{\chi}_0]\} - \int_0^t dt' \text{Tr}_B \{[\hat{\mathcal{H}}_I(t), [\hat{\mathcal{H}}_I(t'), \hat{\chi}(t')]]\}. \quad (2.20)$$

Here, we could insert Eq. (2.18) again for the density matrix $\hat{\chi}(t')$ and so on and so forth. This procedure results in an infinite power series for the reduced system density matrix with respect to the interaction Hamiltonian. In general, this power series can not be solved exactly. Hence, we need to apply additional approximations in order to close the above integro-differential equation. One possible approximation is the so-called Born approximation, which we discuss in more detail within the following paragraph.

2.3 Born approximation

First, we note that the evolution of the density operator described in Eq. (2.20) explicitly depends on the initial state $\hat{\chi}_0$ of the whole system. If we assume that initially system and bath are well separated such that they can not interact with each other, the initial state of the whole system can be written as a direct product state

$$\hat{\chi}_0 = \hat{\rho}_0 \otimes \bar{\rho}_B. \quad (2.21)$$

Here, $\hat{\rho}_0$ is the initial state of the system and $\bar{\rho}_B$ is the initial bath equilibrium density matrix from Eq. (2.3). Furthermore, we assume that the bath is very large and interacts only weakly with the system. This implies that the bath approximately remains in its respective equilibrium state during the evolution of the whole system. Thus, we use the approximation

$$\hat{\chi}(t) = \hat{\rho}(t) \otimes \bar{\rho}_B + \mathcal{O}(\hat{\mathcal{H}}_I). \quad (2.22)$$

This assumption is known as Born approximation. More specifically, this approximation assumes that there is no back-action from the system on the state of the

reservoir. Inserting this result into the evolution of the system density matrix in Eq. (2.20) yields

$$\frac{\partial}{\partial t} \hat{\rho}(t) = -i \text{Tr}_B \left\{ [\hat{\mathcal{H}}_I(t), \hat{\rho}_0 \otimes \bar{\rho}_B] \right\} - \int_0^t dt' \text{Tr}_B \left\{ [\hat{\mathcal{H}}_I(t), [\hat{\mathcal{H}}_I(t'), \hat{\rho}(t') \otimes \bar{\rho}_B]] \right\} + \mathcal{O}(\hat{\mathcal{H}}_I^3). \quad (2.23)$$

Assuming that the weak coupling approximation which is comprised in Eq. (2.21) and Eq. (2.22) is valid, we can neglect the higher order terms $\mathcal{O}(\hat{\mathcal{H}}_I^3)$ in the above integro-differential equation. Using the definition of the interaction Hamiltonian from Eq. (2.9) and the properties of the trace, the above relation simplifies to

$$\begin{aligned} \frac{\partial}{\partial t} \hat{\rho}(t) &= -i \sum_{\alpha} \text{Tr}_B \left\{ \hat{\mathbf{B}}_{\alpha}(t) \bar{\rho}_B \right\} [\hat{\mathbf{A}}_{\alpha}(t), \hat{\rho}_0] \\ &\quad - \sum_{\alpha\beta} \int_0^t dt' \left\{ [\hat{\mathbf{A}}_{\alpha}(t), \hat{\mathbf{A}}_{\beta}(t') \hat{\rho}(t')] \text{Tr}_B \left\{ \hat{\mathbf{B}}_{\alpha}(t) \hat{\mathbf{B}}_{\beta}(t') \bar{\rho}_B \right\} \right. \\ &\quad \left. + [\hat{\rho}(t') \hat{\mathbf{A}}_{\beta}(t'), \hat{\mathbf{A}}_{\alpha}(t)] \text{Tr}_B \left\{ \hat{\mathbf{B}}_{\beta}(t') \hat{\mathbf{B}}_{\alpha}(t) \bar{\rho}_B \right\} \right\} \\ &= \sum_{\alpha\beta} \int_0^t dt' \left\{ [\hat{\mathbf{A}}_{\beta}(t') \hat{\rho}(t'), \hat{\mathbf{A}}_{\alpha}(t)] C_{\alpha\beta}(t, t') + [\hat{\mathbf{A}}_{\alpha}(t), \hat{\rho}(t') \hat{\mathbf{A}}_{\beta}(t')] C_{\beta\alpha}(t', t) \right\}. \end{aligned} \quad (2.24)$$

In the second equality we introduced the equilibrium bath correlation functions of the reservoir which are defined as

$$C_{\alpha\beta}(t, t') = \text{Tr}_B \left\{ \hat{\mathbf{B}}_{\alpha}(t) \hat{\mathbf{B}}_{\beta}(t') \bar{\rho}_B \right\}. \quad (2.25)$$

Additionally, we used the fact that the equilibrium expectation values over single bath operators vanish, i.e.,

$$\langle \hat{\mathbf{B}}_{\alpha}(t) \rangle = \text{Tr}_B \left\{ \hat{\mathbf{B}}_{\alpha}(t) \bar{\rho}_B \right\} = 0. \quad (2.26)$$

This can always be achieved by a suitable transformation of the bath operators and the system Hamiltonian. The transformation

$$\hat{\mathcal{H}}_S \rightarrow \hat{\mathcal{H}}'_S = \hat{\mathcal{H}}_S + \sum_{\alpha} \hat{A}_{\alpha} \langle \hat{B}_{\alpha} \rangle, \quad (2.27)$$

$$\hat{B}_{\alpha} \rightarrow \hat{B}'_{\alpha} = \hat{B}_{\alpha} - \langle \hat{B}_{\alpha} \rangle, \quad (2.28)$$

leaves the total Hamiltonian $\hat{\mathcal{H}}$ invariant and guarantees the vanishing of the expectation values of the bath operators.

Obviously, the Born approximation closes the integro-differential equation (2.20) as both sides of Eq. (2.23) involve the reduced system density matrix only. This approximation corresponds to the second order perturbation theory in the system-bath interaction Hamiltonian.

2.4 Markov approximation

Although the integro-differential equation in Eq. (2.24) is closed, it still depends on the reduced system density matrix of previous times $\hat{\rho}(t')$. This memory effect of the reduced system density matrix makes it still difficult to determine its evolution even in Born approximation. Therefore, we utilize an additional assumption known as the Markov approximation.

In the Markov approximation we suppose that the variation of the reduced density matrix is slower than the decay of the bath correlation function. Then, only system states close to the time t contribute to the memory kernel such that we can in a first step substitute $\hat{\rho}(t') \rightarrow \hat{\rho}(t)$ and find

$$\frac{\partial}{\partial t} \hat{\rho}(t) = \sum_{\alpha\beta} \int_0^t dt' \left\{ [\hat{A}_\beta(t') \hat{\rho}(t), \hat{A}_\alpha(t)] C_{\alpha\beta}(t, t') + [\hat{A}_\alpha(t), \hat{\rho}(t) \hat{A}_\beta(t')] C_{\beta\alpha}(t', t) \right\}. \quad (2.29)$$

This assumption is especially well satisfied for large reservoirs with many degrees of freedom. Here, the bath correlations can rapidly decay due to scattering processes. The resulting time-local expression in Eq. (2.29) for the reduced system density matrix is known in the literature as the Redfield equation [110–112].

Using the fact that $[\hat{\mathcal{H}}_B, \bar{\rho}_B] = 0$, and that the trace remains invariant under cyclic permutation, one can show that the bath correlations depend only on time differences

$$C_{\alpha\beta}(t, t') = \text{Tr} \left\{ e^{+i\hat{\mathcal{H}}_B(t-t')} \hat{B}_\alpha e^{-i\hat{\mathcal{H}}_B(t-t')} \hat{B}_\beta \bar{\rho}_B \right\} = C_{\alpha\beta}(t - t'). \quad (2.30)$$

Moreover, recalling the argument from Eq. (2.15), we note that for hermitian bath operators one additionally obtains the relation

$$C_{\alpha\beta}^*(\tau) = C_{\beta\alpha}(-\tau), \quad (2.31)$$

which describes the time-reversal symmetry of the reservoir correlations.

We can rewrite Eq. (2.29) by substituting $\tau = t - t'$ which yields

$$\frac{\partial}{\partial t} \hat{\rho} = \sum_{\alpha\beta} \int_0^t d\tau \left\{ [\hat{A}_\beta(t - \tau) \hat{\rho}(t), \hat{A}_\alpha(t)] C_{\alpha\beta}(\tau) + [\hat{A}_\alpha(t), \hat{\rho}(t) \hat{A}_\beta(t - \tau)] C_{\beta\alpha}(-\tau) \right\}. \quad (2.32)$$

In a second step, we now shift the upper integration limit to infinity assuming that the value of the time integration remains unchanged. As before, this is well justified if the bath correlations decay sufficiently fast. Thus, we obtain the Born-Markov master equation in its full Markovian form

$$\frac{\partial}{\partial t} \hat{\rho} = \sum_{\alpha\beta} \int_0^\infty d\tau \left\{ [\hat{A}_\beta(t - \tau) \hat{\rho}(t), \hat{A}_\alpha(t)] C_{\alpha\beta}(\tau) + [\hat{A}_\alpha(t), \hat{\rho}(t) \hat{A}_\beta(t - \tau)] C_{\beta\alpha}(-\tau) \right\}. \quad (2.33)$$

Here, the reduced system density matrix at time t is completely uninfluenced by the system state at former times. Unfortunately, this master equation does not necessarily preserve the positivity of the density matrix [113, 114]. This may lead to unphysical results as for example discussed by Yu et al. in Ref. [115]. In order to obtain a Lindblad master equation which, according to G. Lindblad [116], by definition preserves the properties of a density matrix, we additionally need the so-called secular approximation.

2.5 Secular approximation

The secular approximation is needed in order to obtain a master equation that preserves the positivity of the density matrix. This approximation is widely used in the field of quantum optics where it is sometimes synonymously termed as the rotating-wave approximation [117]. The essence of this simplification is to neglect the fast oscillating terms in the master equation. To be able to identify these fast oscillating terms, we evaluate the Markovian master equation presented in Eq. (2.33) using the system eigenbasis from Eq. (2.2). Inserting the completeness relation of the system eigenstates we obtain

$$\begin{aligned} \frac{\partial}{\partial t} \hat{\rho}(t) = & - \sum_{\alpha\beta} \sum_{abcd} \int_0^\infty d\tau \left\{ C_{\alpha\beta}(\tau) \left[|a\rangle \langle a| \hat{A}_\alpha(t) |b\rangle \langle b|, |c\rangle \langle c| \hat{A}_\beta(t-\tau) |d\rangle \langle d| \hat{\rho}(t) \right] \right. \\ & \left. + C_{\beta\alpha}(-\tau) \left[\hat{\rho}(t) |c\rangle \langle c| \hat{A}_\beta(t-\tau) |d\rangle \langle d|, |a\rangle \langle a| \hat{A}_\alpha(t) |b\rangle \langle b| \right] \right\}. \end{aligned} \quad (2.34)$$

Furthermore, using the definition in Eq. (2.16) of the system- and bath operators in the interaction picture, we find

$$\begin{aligned} \frac{\partial}{\partial t} \hat{\rho} = & - \sum_{\alpha\beta} \sum_{abcd} \int_0^\infty d\tau \langle a| \hat{A}_\alpha |b\rangle \langle c| \hat{A}_\beta |d\rangle e^{i(E_a-E_b)t} e^{i(E_c-E_d)(t-\tau)} \\ & \times \left\{ C_{\alpha\beta}(\tau) \left[|a\rangle \langle b|, |c\rangle \langle d| \hat{\rho}(t) \right] + C_{\beta\alpha}(-\tau) \left[\hat{\rho}(t) |c\rangle \langle d|, |a\rangle \langle b| \right] \right\}. \end{aligned} \quad (2.35)$$

Now, we can identify the oscillating terms in the Markovian master equation. We note that for large times t the terms proportional to $e^{i\omega t}$ average out. Therefore, the secular approximation is performed by neglecting all terms that oscillate with time t . Hence, we replace $e^{i\omega t} \rightarrow \delta_{\omega,0}$ and get

$$\frac{\partial}{\partial t} \hat{\rho} = - \sum_{\alpha\beta} \sum_{abcd} \langle a| \hat{A}_\alpha |b\rangle \langle c| \hat{A}_\beta |d\rangle \left\{ \int_0^\infty d\tau C_{\alpha\beta}(\tau) e^{i(E_d-E_c)\tau} \left[|a\rangle \langle b|, |c\rangle \langle d| \hat{\rho}(t) \right] \right.$$

$$\begin{aligned}
 & + \int_0^\infty d\tau C_{\beta\alpha}(-\tau) e^{i(E_d - E_c)\tau} \left[\hat{\rho}(t) |c\rangle \langle d|, |a\rangle \langle b| \right] \Bigg\} \delta_{E_a - E_b, E_d - E_c} \\
 & = - \sum_{\alpha\beta} \sum_{abcd} \langle a| \hat{A}_\alpha |b\rangle \langle c| \hat{A}_\beta |d\rangle \left\{ \Gamma_{\alpha\beta}^+(E_d - E_c) \left[|a\rangle \langle b|, |c\rangle \langle d| \hat{\rho}(t) \right] \right. \\
 & \quad \left. + \Gamma_{\beta\alpha}^-(E_c - E_d) \left[\hat{\rho}(t) |c\rangle \langle d|, |a\rangle \langle b| \right] \right\} \delta_{E_a - E_b, E_d - E_c}. \tag{2.36}
 \end{aligned}$$

In the last equality we introduced the half-sided Fourier transformed bath correlations functions which are defined as

$$\Gamma_{\alpha\beta}^\pm(\omega) = \int_{-\infty}^\infty d\tau \Theta(\pm\tau) C_{\alpha\beta}(\tau) e^{i\omega\tau}. \tag{2.37}$$

In order to further shorten our notation, we now introduce the operator

$$\hat{\Pi}_{ab} = |a\rangle \langle b|, \tag{2.38}$$

and the transition frequencies

$$\omega_{a,b} = E_a - E_b. \tag{2.39}$$

With these definitions, we can rewrite the master equation in Eq. (2.36) as

$$\begin{aligned}
 \frac{\partial}{\partial t} \hat{\rho} = & - \sum_{\alpha\beta} \sum_{abcd} \langle a| \hat{A}_\alpha |b\rangle \langle c| \hat{A}_\beta |d\rangle \left\{ \Gamma_{\alpha\beta}^+(\omega_{d,c}) \left[\hat{\Pi}_{ab}, \hat{\Pi}_{cd} \hat{\rho}(t) \right] \right. \\
 & \left. + \Gamma_{\beta\alpha}^-(\omega_{d,c}) \left[\hat{\rho}(t) \hat{\Pi}_{cd}, \hat{\Pi}_{ab} \right] \right\} \delta_{\omega_{a,b}, \omega_{d,c}}. \tag{2.40}
 \end{aligned}$$

This equation preserves the positivity of the reduced system density matrix. However, it still involves the rather unconventional half-sided Fourier transformed bath correlations which we like to link to the Fourier transforms. This representation also enables one to show that Eq. (2.40) is of Lindblad form.

2.6 Lindblad master equation

To obtain the Lindblad form of the Born-Markov-Secular (BMS) master equation from Eq. (2.40), we split the half-sided Fourier transformed correlations into hermitian ($\gamma_{\alpha\beta}$) and anti-hermitian ($\sigma_{\alpha\beta}$) parts according to

$$\Gamma_{\alpha\beta}^\pm(\omega) = \frac{1}{2} \gamma_{\alpha\beta}(\omega) \pm \frac{1}{2} \sigma_{\alpha\beta}(\omega). \tag{2.41}$$

The full even and odd Fourier transformed bath correlation functions are defined by

$$\gamma_{\alpha\beta}(\omega) = \Gamma_{\alpha\beta}^+(\omega) + \Gamma_{\alpha\beta}^-(\omega) = \int_{-\infty}^{+\infty} d\tau C_{\alpha\beta}(\tau) e^{i\omega\tau}, \quad (2.42)$$

$$\sigma_{\alpha\beta}(\omega) = \Gamma_{\alpha\beta}^+(\omega) - \Gamma_{\alpha\beta}^-(\omega) = \int_{-\infty}^{+\infty} d\tau C_{\alpha\beta}(\tau) \text{sgn}(\tau) e^{i\omega\tau}, \quad (2.43)$$

where

$$\text{sgn}(x) = \begin{cases} +1, & \text{for } x > 0, \\ -1, & \text{for } x < 0, \end{cases} \quad (2.44)$$

is the sign function. Inserting these results in Eq. (2.40), we obtain

$$\begin{aligned} \frac{\partial}{\partial t} \hat{\rho} = & -\frac{1}{2} \sum_{\alpha\beta} \sum_{abcd} \langle a | \hat{A}_\alpha | b \rangle \langle c | \hat{A}_\beta | d \rangle \left\{ [\gamma_{\alpha\beta}(\omega_{d,c}) + \sigma_{\alpha\beta}(\omega_{d,c})] [\hat{\Pi}_{ab}, \hat{\Pi}_{cd} \hat{\rho}] \right. \\ & \left. + [\gamma_{\beta\alpha}(-\omega_{d,c}) - \sigma_{\beta\alpha}(-\omega_{d,c})] [\hat{\rho} \hat{\Pi}_{cd}, \hat{\Pi}_{ab}] \right\} \delta_{\omega_{a,b}, \omega_{d,c}}. \end{aligned} \quad (2.45)$$

Subsequently, by shifting the summation indices and collecting the terms which are proportional to the even and odd Fourier transform, respectively, we get the desired master equation in Lindblad form [116] which reads as

$$\frac{\partial}{\partial t} \hat{\rho} = -i [\hat{\mathcal{H}}_{\text{LS}}, \hat{\rho}] + \sum_{abcd} \gamma_{ab,cd} \left[\hat{\Pi}_{cd} \hat{\rho} \hat{\Pi}_{ba}^\dagger - \frac{1}{2} \{ \hat{\Pi}_{ba}^\dagger \hat{\Pi}_{cd}, \hat{\rho} \} \right]. \quad (2.46)$$

Here, we introduced the so-called Lamb-Shift Hamiltonian

$$\hat{\mathcal{H}}_{\text{LS}} = \frac{1}{2i} \sum_{\alpha\beta} \sum_{abcd} \sigma_{\alpha\beta}(\omega_{d,c}) \langle a | \hat{A}_\alpha | b \rangle \langle c | \hat{A}_\beta | d \rangle \hat{\Pi}_{ba}^\dagger \hat{\Pi}_{cd} \delta_{\omega_{a,b}, \omega_{d,c}}, \quad (2.47)$$

and the rates

$$\gamma_{ab,cd} = \sum_{\alpha\beta} \gamma_{\alpha\beta}(\omega_{d,c}) \langle a | \hat{A}_\alpha | b \rangle \langle c | \hat{A}_\beta | d \rangle \delta_{\omega_{a,b}, \omega_{d,c}}. \quad (2.48)$$

The Lamb-shift Hamiltonian in Eq. (2.47) renormalizes the system Hamiltonian due to the interaction with the environment. Using the properties of the bath correlation functions and the definitions of their even and odd Fourier transforms, one can show that the Lamb-shift Hamiltonian is a self-adjoint operator, i.e., $\hat{\mathcal{H}}_{\text{LS}} = \hat{\mathcal{H}}_{\text{LS}}^\dagger$, and it commutes with the system Hamiltonian, i.e., $[\hat{\mathcal{H}}_{\text{LS}}, \hat{\mathcal{H}}_S] = 0$.

Furthermore, the rate matrix $\gamma_{\alpha\beta}(\omega)$ is positive definite and, therefore, the BMS master equation presented in Eq. (2.46) is of Lindblad form and preserves the positivity of the density matrix [118].

In order to gain physical insight to the effect of the Lamb-shift Hamiltonian, we assume that the system eigenstates are orthogonal, i. e. $\langle a|b \rangle = \delta_{ab}$. Then, we find that the Lamb-shift Hamiltonian in Eq. (2.47) becomes

$$\hat{\mathcal{H}}_{\text{LS}} = \frac{1}{2i} \sum_{\alpha\beta} \sum_{abd} \sigma_{\alpha\beta}(\omega_{db}) \langle a| \hat{A}_\alpha |b \rangle \langle b| \hat{A}_\beta |d \rangle \hat{\Pi}_{ad} \delta_{E_a, E_d}. \quad (2.49)$$

Additionally, if the system has non-degenerate eigenvalues, i. e. $\delta_{E_a, E_d} = \delta_{a,d}$, we find that the Lamb-shift Hamiltonian becomes diagonal in the system eigenbasis and reads as

$$\hat{\mathcal{H}}_{\text{LS}} = \frac{1}{2i} \sum_{\alpha\beta} \sum_{ab} \sigma_{\alpha\beta}(\omega_{a,b}) \langle a| \hat{A}_\alpha |b \rangle \langle b| \hat{A}_\beta |a \rangle |a \rangle \langle a|. \quad (2.50)$$

Hence, for systems where the density matrix $\hat{\rho}$ is also diagonal with respect to their eigenbasis, the commutator in Eq. (2.46) vanishes. Within the next section, we show that for systems with non-degenerate eigenvalues an effective rate equation for the reduced system density matrix can be established. From this rate equation description follows that the reduced system density matrix is also diagonal in the system eigenbasis. Consequently, systems with non-degenerate eigenvalues are described by the Lindblad master equation

$$\frac{\partial}{\partial t} \hat{\rho} = \sum_{abcd} \gamma_{ab,cd} \left[\hat{\Pi}_{cd} \hat{\rho} \hat{\Pi}_{ba}^\dagger - \frac{1}{2} \{ \hat{\Pi}_{ba}^\dagger \hat{\Pi}_{cd}, \hat{\rho} \} \right]. \quad (2.51)$$

Throughout this thesis, we investigate transport systems that can be described by the above Lindblad master equation.

2.7 Effective rate equation

The appearance of the operators $\hat{\Pi}_{ab}$ in Eq. (2.46) suggests to evaluate the above equation in the system eigenbasis. We assume that this eigenbasis consists of orthogonal eigenstates and non-degenerate eigenvalues. Then, by calculating the matrix elements in the system eigenbasis, i.e., determining $\rho_{nm} = \langle n| \hat{\rho} |m \rangle$, the commutator with the Lamb-shift Hamiltonian in Eq. (2.46) vanishes and we find

$$\begin{aligned} \dot{\rho}_{nm} &= \sum_{abcd} \gamma_{ab,cd} \left[\delta_{n,c} \delta_{b,m} \rho_{da} - \frac{1}{2} \delta_{b,c} \{ \delta_{n,a} \rho_{dm} + \delta_{m,d} \rho_{na} \} \right] \\ &= \sum_{ad} \gamma_{am,nd} \rho_{da} - \frac{1}{2} \sum_{ab} [\gamma_{nb,ba} \rho_{am} + \gamma_{ab,bm} \rho_{na}]. \end{aligned} \quad (2.52)$$

Using the assumption that the system eigenspectrum is non-degenerate together with the definition of the rates in Eq. (2.48), we see that some of the rates become

proportional to Kronecker deltas, e.g., $\gamma_{nb,ba} \sim \delta_{a,n}$ and $\gamma_{ab,bm} \sim \delta_{a,m}$. This leads to the simplified equation

$$\dot{\rho}_{nm} = \sum_{ab} \gamma_{bm,na} \rho_{ab} - \frac{1}{2} \sum_b [\gamma_{nb,bn} + \gamma_{mb,bm}] \rho_{nm}. \quad (2.53)$$

If we just consider the populations of the system density matrix, i.e., $\rho_n = \langle n | \hat{\rho} | n \rangle$, the above equation collapses to an effective rate equation which reads as

$$\dot{\rho}_n = \sum_b [\gamma_{bn,nb} \rho_b - \gamma_{nb,bn} \rho_n], \quad (2.54)$$

with positive rates $\gamma_{bn,nb} \geq 0$. Obviously, the populations do not couple to the coherences. We obtain two systems of coupled differential equations for the populations and the coherences, respectively. Consequently, for long times the coherences just decay and the system steady-state is determined by the dynamics of the populations only. Note that since the rates $\gamma_{nb,bn}$ are just the diagonal elements of the rate matrix $\gamma_{ab,cd}$ the above equation (2.54) also preserves the positivity of the density matrix.

2.8 Liouville space

In formal analogy to the Schrödinger equation one commonly rewrites the Lindblad master equation in Eq. (2.51) in the form

$$\frac{\partial}{\partial t} \hat{\rho} = \hat{\mathcal{L}} [\hat{\rho}]. \quad (2.55)$$

Here, we introduced the Liouville super-operator $\hat{\mathcal{L}} [\hat{\rho}]$ that acts on the system density matrix. This super-operator is defined as

$$\hat{\mathcal{L}} [\hat{\rho}] = \sum_{abcd} \gamma_{ab,cd} \left[\hat{\Pi}_{cd} \hat{\rho} \hat{\Pi}_{ba}^\dagger - \frac{1}{2} \{ \hat{\Pi}_{ba}^\dagger \hat{\Pi}_{cd}, \hat{\rho} \} \right]. \quad (2.56)$$

Due to the linearity of the Liouville super-operator with respect to the reduced density matrix it is convenient to switch to the so-called Liouville space representation. In this representation one transforms the system density matrix to a vector, i.e., $\hat{\rho} \rightarrow \rho$, and the Liouville super-operator to a matrix. For a system of dimension d the density matrix in the Liouville space is a vector with d^2 entries and the Liouvillian $\hat{\mathcal{L}} \rightarrow \mathcal{W}$ becomes a $(d^2 \times d^2)$ matrix. This matrix is in general not self-adjoint and has complex eigenvalues.

The transformation to Liouville space is achieved by choosing a specific ordering of the elements of the density matrix in a vector. Normally, one chooses an ordering where the populations come first followed by the coherences in increasing order of

the system eigenstates:

$$\hat{\rho} = \begin{pmatrix} \rho_{11} & \rho_{12} & \cdots & \rho_{1d} \\ \rho_{21} & \rho_{22} & \cdots & \rho_{2d} \\ \vdots & \vdots & \cdots & \vdots \\ \rho_{d1} & \rho_{d2} & \cdots & \rho_{dd} \end{pmatrix} \Rightarrow \rho = \left(\begin{array}{c} \rho_{11} \\ \vdots \\ \rho_{dd} \\ \rho_{12} \\ \vdots \\ \rho_{1d} \\ \rho_{21} \\ \vdots \\ \rho_{dd-1} \end{array} \right) \begin{array}{l} \left. \vphantom{\begin{pmatrix} \rho_{11} \\ \vdots \\ \rho_{dd} \end{pmatrix}} \right\} d \text{ populations} \\ \left. \vphantom{\begin{pmatrix} \rho_{12} \\ \vdots \\ \rho_{1d} \\ \rho_{21} \\ \vdots \\ \rho_{dd-1} \end{pmatrix}} \right\} d(d-1) \text{ coherences} \end{array} \quad (2.57)$$

Of course this choice of ordering is not unique. However, in this specific choice the Liouvillian corresponding to Eq. (2.53) assumes block form, immediately indicating the decoupling of populations and coherences.

Another advantage of the Liouville space representation is that the evolution of the reduced system density matrix now reads as

$$\frac{\partial}{\partial t} \rho = \mathcal{W} \rho, \quad (2.58)$$

and can thus be formally solved by the matrix exponential

$$\rho(t) = e^{\mathcal{W}t} \rho(0). \quad (2.59)$$

Solving the matrix exponential is in general a rather difficult task since the Liouvillian is non-hermitian and there is no spectral decomposition. However, for systems that can be described by an effective rate equation consistent with Eq. (2.53), the Liouvillian assumes block-form with at least two decoupled blocks, \mathcal{W}^{pop} for the populations and \mathcal{W}^{coh} for the coherences of the reduced system density matrix. For such systems the calculation of a matrix exponent $e^{\mathcal{W}^{\text{pop}}t}$ involving only the population block of the Liouvillian is much easier to calculate than the full expression from Eq. (2.59).

Comparing Eq. (2.58) with Eq. (2.54), we see that the matrix elements of the block \mathcal{W}^{pop} , which describes the evolution of the populations of the reduced system density matrix, is given by

$$\mathcal{W}_{nn}^{\text{pop}} = \gamma_{nn,nn} - \sum_b \gamma_{nb,bn}, \quad (2.60)$$

$$\mathcal{W}_{nm}^{\text{pop}} = \gamma_{mn,nm}, \quad \text{for } m \neq n. \quad (2.61)$$

It is straightforward to show that this implies the property

$$\sum_n \mathcal{W}_{nn}^{\text{pop}} = 0, \quad (2.62)$$

which guarantees the preservation of the trace of the reduced density matrix.

2.9 Multi-terminal setups

So far we only considered a single reservoir which is weakly coupled to the system. Since the reservoir is in the thermal equilibrium state given by Eq. (2.3), such a setup never results in a nonequilibrium steady-state. In fact, letting the system density matrix evolve for sufficiently long times one always observes a thermalization with the surrounding bath. The steady-state of the system would be a thermal state with the same temperature and chemical potential as the reservoir. This behavior can be traced back to the property

$$C_{\alpha,\beta}(\tau) = C_{\beta,\alpha}(-\tau - i\beta), \quad (2.63)$$

of the equilibrium bath correlation functions known as the Kubo-Martin-Schwinger condition [119–121].

In order to generate the more interesting case of nonequilibrium steady-states of the system, one needs at least two reservoirs with different thermal equilibrium states. Here, the system tries to thermalize with each reservoir separately which is of course not possible. Provided that there is a steady-state for such a two-terminal setup, it is in general not a thermal state. However, there are counterexamples where the system equilibrates with respect to a single effective, but in general non-thermal, reservoir [122–124]. Analogously, this argumentation holds for setups with more than two terminals.

If we assume a multi-terminal transport setup with M reservoirs as sketched in Fig. 2.2, we first note that the respective reservoirs enter the whole Hamiltonian $\hat{\mathcal{H}}$ from Eq. (2.1) additively such that the full bath Hamiltonian is given by

$$\hat{\mathcal{H}}_B = \sum_{\nu} \hat{\mathcal{H}}_B^{(\nu)}. \quad (2.64)$$

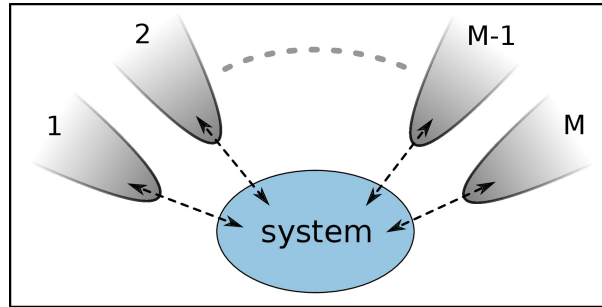


Figure 2.2: Sketch of a multi-terminal setup.

The corresponding equilibrium state of the full environment can be written as a tensor product $\bar{\rho} = \bar{\rho}_B^{(1)} \otimes \dots \otimes \bar{\rho}_B^{(M)}$ where each reservoir ν is characterized by its corresponding thermal state

$$\bar{\rho}_B^{(\nu)} = \frac{e^{-\beta_{\nu}(\hat{\mathcal{H}}_B^{(\nu)} - \mu_{\nu} \hat{N}_B^{(\nu)})}}{\text{Tr} \left\{ e^{-\beta_{\nu}(\hat{\mathcal{H}}_B^{(\nu)} - \mu_{\nu} \hat{N}_B^{(\nu)})} \right\}}, \quad (2.65)$$

with its respective inverse temperature $\beta_{\nu} = 1/T_{\nu}$ and chemical potential μ_{ν} . These reservoirs are weakly coupled to the system by their respective coupling Hamiltoni-

ans $\hat{\mathcal{H}}_I^{(\nu)}$, which sum up to the total interaction Hamiltonian

$$\hat{\mathcal{H}}_I = \sum_{\nu} \hat{\mathcal{H}}_I^{(\nu)} = \sum_{\alpha} \hat{A}_{\alpha} \otimes \sum_{\nu} \hat{B}_{\alpha}^{(\nu)}. \quad (2.66)$$

Due to the tensor product form of the above interaction Hamiltonian the M reservoirs enter the Lindblad master equation in Eq. (2.46) via the bath correlation functions $C_{\alpha\beta}(\tau)$ defined in Eq. (2.25). These multi-terminal bath correlation functions become

$$C_{\alpha\beta}(\tau) = \sum_{\nu} C_{\alpha\beta}^{(\nu)}(\tau), \quad (2.67)$$

with the respective reservoir correlation function

$$C_{\alpha\beta}^{(\nu)}(\tau) = \text{Tr}_B^{(\nu)} \left\{ \hat{B}_{\alpha}^{(\nu)}(\tau) \hat{B}_{\beta}^{(\nu)} \bar{\rho}_B^{(\nu)} \right\}. \quad (2.68)$$

In consequence, the BMS master equation (2.46) is formally not changed and the total Liouvillian in Eq. (2.58) can be decomposed into a sum over the respective single reservoir Liouvillians, i.e.,

$$\mathcal{W} = \sum_{\nu} \mathcal{W}^{(\nu)}. \quad (2.69)$$

Using these results, we can now analyze the transport properties of multi-terminal setups for weak coupling in the framework of a BMS master equation in Lindblad form.

2.10 Conditioned master equation

Often, one finds that the full system composed of all reservoirs and the small system of interest obey some conservation laws. The most prominent examples are the conservation of particle number and energy. Except for some generic models which fulfill $[\hat{\mathcal{H}}_S, \hat{\mathcal{H}}_I] = 0$ and $[\hat{\mathcal{H}}_B, \hat{\mathcal{H}}_I] \neq 0$, like pure dephasing models as discussed, e.g., in Refs. [125–127], this observation implies that a loss of particles and/or energy in the system is accompanied by a corresponding gain in the attached reservoirs and vice versa. Hence, in order to characterize the flow of particles and energy between the system and a specific reservoir it is sufficient to count the quantities that enter or leave the respective bath. Since the reservoirs enter the master equation additively, we can uniquely identify the contributions from each reservoir. Therefore, it suffices for now to consider the transfer of particles and/or energy between the system and a single reservoir only.

To resolve the number of particles and energy quanta that are exchanged between the system and the surrounding environment, we rewrite the rate equation for the

populations in Liouville space from Eq. (2.58), as a rate equation for the evolution of the probability p_i to find the system in state $|i\rangle$ which yields

$$\dot{p}_i = \sum_j \mathcal{W}_{ij} p_j. \quad (2.70)$$

Hence, the probability changes according to

$$dp_i = \sum_j \mathcal{W}_{ij} p_j dt. \quad (2.71)$$

Here, we can interpret the expression $\mathcal{W}_{ij} p_j dt$ as the probability to reach the state $|i\rangle$ starting from the state $|j\rangle$ via a jump \mathcal{W}_{ij} within the time dt . Then, we see that the change dp_i of the probability to find the system in state $|i\rangle$ is given as a sum over the probabilities for all possible jumps which result in state $|i\rangle$ within the time dt . Furthermore, we note that due to the conservation of the total number of particles and the total amount of energy each jump \mathcal{W}_{ij} in the system is accompanied by an exchange of a certain number of particles $\Delta n_{ij} = n_i - n_j$ and a certain amount of energy $\Delta E_{ij} = E_i - E_j$ with the reservoir.

Now, we denote the probability to find the system in state $|i\rangle$ under the condition that n particles and the energy E have been transferred to the reservoir as $p_i^{(n,E)}$. Obviously, this probability has to fulfill the relation

$$p_i = \sum_{n=-\infty}^{\infty} \sum_{E=-\infty}^{\infty} p_i^{(n,E)}. \quad (2.72)$$

From our discussion of the Eq. (2.71), we now find that these conditioned probabilities $p_i^{(n,E)}$ obey a rate equation of the form

$$dp_i^{(n,E)} = \sum_j \mathcal{W}_{ij}^{(\Delta n_{ij}, \Delta E_{ij})} p_j^{(n+\Delta n_{ij}, E+\Delta E_{ij})} dt. \quad (2.73)$$

We can interpret the right hand side of the above rate equation as follows: Before the jump occurs, the system is in state $|j\rangle$ with n_j particles and an energy E_j in the system. At the same time there are $(n + \Delta n_{ij})$ particles and the energy $(E + \Delta E_{ij})$ in the bath. When the jump occurs Δn_{ij} particles and the energy ΔE_{ij} are transferred between bath and system. After the jump the system is in state $|i\rangle$ with n_i particles and the energy E_i whereas in the bath there are now n particles and the energy E .

Since, in the summation in Eq. (2.73) only the allowed system transitions contribute, we additionally assume that the jump operators $\mathcal{W}_{ij}^{(\Delta n_{ij}, \Delta E_{ij})}$ change the particle number in the system at most by one, i.e., $\Delta n_{ij} \in \{-1, 0, 1\}$. Thus, we explicitly neglect pair tunneling and higher order tunneling processes which is well justified for most microscopically derived transport setups. For the energy transferred in a single jump there is in general no such restriction. Each jump can transfer the energy ΔE_{ij} as long as the corresponding transition from state $|i\rangle$ to state $|j\rangle$ is allowed.

Using these assumptions, we can deduce from Eq. (2.73) a master equation for the conditioned density matrix in Liouville space which reads as

$$\dot{\rho}^{(n,E)} = \mathcal{W}_0 \rho^{(n,E)} + \sum_{\Delta E} \left[\mathcal{W}_{\Delta E}^+ \rho^{(n-1, E-\Delta E)} + \mathcal{W}_{\Delta E}^- \rho^{(n+1, E+\Delta E)} \right]. \quad (2.74)$$

This master equation describes the evolution of the density matrix $\rho^{(n,E)}$ under the condition that n particles and the energy E have been transported through the system to the monitored reservoir. The operator \mathcal{W}_0 does not induce any particle or energy exchange between the considered reservoir and the system. Contrary, the operators $\mathcal{W}_{\Delta E}^+$ and $\mathcal{W}_{\Delta E}^-$ induce a transfer of a single particle and the amount of energy ΔE between system and reservoir. The summation in the above master equation runs over all possible energy transitions ΔE in the system.

Note that this energy- and particle-number conditioned master equation can also be obtained by introducing projection operators as virtual detectors [128].

Noticing that the rates contained in the operators \mathcal{W}_0 , $\mathcal{W}_{\Delta E}^\pm$ neither depend on the number n of transferred particles nor on the amount of transferred energy E , suggests to further simplify Eq. (2.74) by a suitable Fourier transformation. Therefore, assuming a continuous energy spectrum in the bath, we simultaneously perform a discrete and a continuous Fourier transformation of the form

$$\rho(\chi, \eta, t) = \sum_{n=-\infty}^{\infty} \int_{-\infty}^{\infty} dE \rho^{(n,E)}(t) e^{i(n\chi + E\eta)}. \quad (2.75)$$

The corresponding inverse Fourier transformation is given by

$$\rho^{(n,E)}(t) = \left(\frac{1}{2\pi} \right)^2 \int_{-\pi}^{+\pi} d\chi \int_{-\infty}^{+\infty} d\eta \rho(\chi, \eta, t) e^{-i(n\chi + E\eta)}. \quad (2.76)$$

The continuum assumption is justified for systems with various incommensurable transition frequencies where the spectrum of the exchanged energy becomes dense in the limit of a large number jump processes. It clearly breaks down in the so-called tight coupling limit where only a single transition in the system is possible. Therefore, depending on the transport setup one has to discard the continuous energy integration in Eq. (2.75) in favor of a discrete summation. However, this ambiguity does not affect our general argument.

The Fourier transformation (2.75) transforms the conditioned master equation (2.74) to an ordinary differential equation that reads as

$$\frac{\partial}{\partial t} \rho(\chi, \eta, t) = \underbrace{\left\{ \mathcal{W}_0 + \sum_{\Delta E} \left[\mathcal{W}_{\Delta E}^+ e^{+i(\chi + \Delta E \eta)} + \mathcal{W}_{\Delta E}^- e^{-i(\chi + \Delta E \eta)} \right] \right\}}_{\mathcal{W}(\chi, \eta)} \rho(\chi, \eta, t). \quad (2.77)$$

On the one hand, we see that the transformation in Eq. (2.75) strongly reduces the dimension of the system of equations as the reduced density matrix does not depend on E and n anymore. On the other hand, it introduces the two new parameters χ and η via some complex phases linked with the jump operators $\mathcal{W}_{\Delta E}^{\pm}$. Hence, every transfer of a particle or a quantum of energy is associated with a corresponding complex phase. These new parameters χ and η are also called particle- and energy-counting fields as introduced by L. S. Levitov [129] and L. Nicolin and D. Segal [130], respectively.

Finally, we note that multiple reservoirs enter in the above rate equation (2.73) additively according to Eq. (2.69) such that we can write

$$\dot{p}_i^{(n,E)} = \sum_{\nu} \sum_j \mathcal{W}_{ij}^{(\nu)} p_j^{(n+\Delta n_{ij}, E+\Delta E_{ij})}. \quad (2.78)$$

When deriving the corresponding counting field resolved master equation, we can proceed as described before. However, we need to introduce particle- and energy-counting fields for each reservoir, respectively. This yields the multi-terminal differential equation

$$\dot{\rho}(\chi, \eta, t) = \mathcal{W}(\chi, \eta) \rho(\chi, \eta, t), \quad (2.79)$$

where $\chi = (\chi_1, \dots, \chi_M)$ and $\eta = (\eta_1, \dots, \eta_M)$ are the counting field vectors containing the particle and energy counting fields for all reservoirs. This equation is formally solved by

$$\rho(\chi, \eta, t) = e^{\mathcal{W}(\chi, \eta)t} \rho(\chi, \eta, 0) = e^{\mathcal{W}(\chi, \eta)t} \rho_0, \quad (2.80)$$

where in the second equality we assume that initially no particles and energy is exchanged between system and environment, i.e., $\rho^{(n,E)}(0) = \rho_0 \delta_{n,0} \delta_{E,0}$.

The explicit role and use of these counting fields introduced within this paragraph is discussed in more detail within the following section.

2.11 Full counting statistics

In the previous section, we derived a rate equation for probabilities conditioned on the number of transferred particles and energy quanta. This derivation is of course closely related to measurable transport properties. In fact, information about the particle- and energy currents flowing in nonequilibrium between the system and the attached reservoirs can be obtained by monitoring the exchanged quanta [131]. We therefore disregard now the internal state of the system and ask for the probability $p^{(n,E)}(t)$ that at time t the reservoirs $(1, \dots, M)$ and the system have exchanged $\mathbf{n} = (n_1, \dots, n_M)$ particles and $\mathbf{E} = (E_1, \dots, E_M)$ quanta of energy. This probability is given by

$$p^{(n,E)}(t) = \sum_i p_i^{(n,E)}(t) = \text{Tr} \{ \rho^{(n,E)}(t) \}. \quad (2.81)$$

We can use the inverse Fourier transformation from Eq. (2.76) for the multi-terminal setup to relate the above probability distribution to the particle and energy counting fields. We obtain the expression

$$p^{(n,E)}(t) = \left(\frac{1}{2\pi}\right)^{2M} \int_{-\pi}^{+\pi} d\chi_1 \dots d\chi_M \int_{-\infty}^{+\infty} d\eta_1 \dots d\eta_M \text{Tr} \{e^{\mathcal{W}(\chi,\eta)t} \rho_0\} e^{-i(n\chi + E\eta)}. \quad (2.82)$$

From the above expression, we can easily calculate the corresponding moments of the probability distribution using derivatives with respect to the counting fields. The moments of the particle and energy distribution are given by

$$\langle n^k \rangle = \sum_n n^k p^{(n,E)}(t) = (-i \partial_\chi)^k \mathcal{M}(\chi, \eta, t) \Big|_{\chi=\eta=0}, \quad (2.83)$$

$$\langle E^k \rangle = \int dE E^k p^{(n,E)}(t) = (-i \partial_\eta)^k \mathcal{M}(\chi, \eta, t) \Big|_{\chi=\eta=0}, \quad (2.84)$$

respectively. Here, we introduced the moment-generating function as

$$\mathcal{M}(\chi, \eta, t) = \text{Tr} \{\rho(\chi, \eta, t)\} = \text{Tr} \{e^{\mathcal{W}(\chi,\eta)t} \rho_0\}. \quad (2.85)$$

From this moment-generating function the full distribution can be established by calculating the full Fourier transform. For a single reservoir ν these transformations read

$$p_n^{(\nu)}(t) = \frac{1}{2\pi} \int_{-\pi}^{+\pi} d\chi_\nu \mathcal{M}(\chi, \eta, t) e^{-in\chi_\nu} \Big|_{\chi=\eta=0}, \quad (2.86)$$

$$p_E^{(\nu)}(t) = \frac{1}{2\pi} \int_{-\infty}^{+\infty} d\eta_\nu \mathcal{M}(\chi, \eta, t) e^{-iE\eta_\nu} \Big|_{\chi=\eta=0}. \quad (2.87)$$

We will be mostly interested in the first moment which corresponds to the respective current. These currents measured at the bath ν can be calculated according to

$$I_N^{(\nu)}(t) = \langle \dot{n} \rangle_\nu = -i \text{Tr} \left\{ \frac{\partial}{\partial \chi_\nu} \dot{\rho}(\chi, \eta, t) \right\} \Big|_{\chi=\eta=0}, \quad (2.88)$$

$$I_E^{(\nu)}(t) = \langle \dot{E} \rangle_\nu = -i \text{Tr} \left\{ \frac{\partial}{\partial \eta_\nu} \dot{\rho}(\chi, \eta, t) \right\} \Big|_{\chi=\eta=0}. \quad (2.89)$$

Nevertheless, the calculation of higher moments, which for example reveal information about the variance and skewness of the distribution, is straightforward. However, they are usually harder to measure experimentally.

2.12 Steady-state currents

The presence of more than two reservoirs which are connected to the same system may lead to the emergence of nonvanishing steady-state currents. These currents

result from the fact that such setups can assume nonequilibrium steady-states for long times. In particular, the nonequilibrium steady-state properties of a transport system can be used for example to extract information about the system or perform some kind of work. These properties motivate our studies within the following chapters.

Starting from the evolution of the reduced system density matrix in Liouville-space representation as introduced in Eq. (2.79), the steady-state of the system of interest $\bar{\rho}$ is defined as the solution of the equation

$$\frac{\partial}{\partial t} \bar{\rho} = 0 = \mathcal{W}(\mathbf{0}, \mathbf{0}) \bar{\rho}. \quad (2.90)$$

In order to obtain a valid density matrix, we additionally require that the steady-state is normalized such that $\text{Tr} \{\bar{\rho}\} = 1$. Together, these relations define the steady-state of the system. If we additionally disregard bistable systems, the steady-state is uniquely determined by the above conditions.

Considering the analysis of transport setups using the full-counting-statistics approach, we are mostly interested in the first moment corresponding to the steady-state currents through the system. These steady-state currents can be obtained from the moment generating function in Eq. (2.85) which for long times reads as

$$\lim_{t \rightarrow \infty} \mathcal{M}(\chi, \eta, t) = \text{Tr} \{ e^{\mathcal{W}(\chi, \eta)t} \bar{\rho} \}. \quad (2.91)$$

Subsequently, we can calculate the steady-state particle current $J_N^{(\nu)} \equiv \bar{I}_N^{(\nu)}$, according to the Eq. (2.88) and Eq. (2.89) and obtain

$$\begin{aligned} J_N^{(\nu)} &= -i \frac{\partial}{\partial \chi_\nu} \text{Tr} \left\{ \frac{d}{dt} e^{\mathcal{W}(\chi, \eta)t} \bar{\rho} \right\} \Big|_{\chi=\eta=0} = -i \frac{\partial}{\partial \chi_\nu} \text{Tr} \{ \mathcal{W}(\chi, \eta) e^{\mathcal{W}(\chi, \eta)t} \bar{\rho} \} \Big|_{\chi=\eta=0} \\ &= -i \text{Tr} \left\{ \left[\frac{\partial}{\partial \chi_\nu} \mathcal{W}(\chi, \eta) \Big|_{\chi=\eta=0} \right] e^{\mathcal{W}(\mathbf{0}, \mathbf{0})t} \bar{\rho} \right\} - i \text{Tr} \left\{ \mathcal{W}(\mathbf{0}, \mathbf{0}) \left[\frac{\partial}{\partial \chi_\nu} e^{\mathcal{W}(\chi, \eta)t} \bar{\rho} \Big|_{\chi=\eta=0} \right] \right\} \\ &= -i \text{Tr} \left\{ \left[\frac{\partial}{\partial \chi_\nu} \mathcal{W}(\chi, \eta) \Big|_{\chi=\eta=0} \right] \bar{\rho} \right\}. \end{aligned} \quad (2.92)$$

Here, we used the property $\text{Tr} \{ \mathcal{W}(\mathbf{0}, \mathbf{0}) \} = 0$ and the relation $\text{Exp}[\mathcal{W}(\mathbf{0}, \mathbf{0})t] \bar{\rho} = \bar{\rho}$ in the last step. Therefore, we find

$$J_N^{(\nu)} = -i \text{Tr} \left\{ \frac{\partial}{\partial \chi_\nu} \mathcal{W}(\chi, \eta) \bar{\rho} \right\} \Big|_{\chi=\eta=0}, \quad (2.93)$$

and analogously for the steady-state energy current we obtain

$$J_E^{(\nu)} = -i \text{Tr} \left\{ \frac{\partial}{\partial \eta_\nu} \mathcal{W}(\chi, \eta) \bar{\rho} \right\} \Big|_{\chi=\eta=0}. \quad (2.94)$$

Since the above steady-state currents have to respect the conservation of the total particle number and the total energy, we find that this implies the relations

$$\sum_{\nu} J_N^{(\nu)} = \sum_{\nu} J_E^{(\nu)} = 0. \quad (2.95)$$

Especially for the case of a two-terminal transport setup with a left (L) and a right (R) reservoir, this yields the correspondences $J_N^{(L)} = -J_N^{(R)}$ and $J_E^{(L)} = -J_E^{(R)}$. Therefore, we define the currents flowing from left to right through the few-level system as

$$J_N \equiv J_N^{(L)} \quad \text{and} \quad J_E \equiv J_E^{(L)}, \quad (2.96)$$

such that we can mostly neglect the bath index within the discussions in Ch. 4. Note that the currents $J_N^{(L)}$ and $J_E^{(L)}$ are counted positive for particles that tunnel from the left reservoir into the system. Hence, in a two-terminal setup, a positive current J_N corresponds to particle transport from the left reservoir through the system into the right reservoir.

2.13 Entropy production

The existence of nonvanishing steady-state particle and energy currents through a thermodynamic device usually gives rise to a heat flow J_Q from which one can extract a work. This work is in general defined as

$$W = -Fx, \quad (2.97)$$

where F is a conservative force and x the conjugate variable. Such open systems which are also called thermo-elements are very useful as sensors or as power generators. They are well known and have been studied in the framework of classical thermodynamics for almost two centuries. Nowadays, these studies have been extended to open nanoscale quantum systems, e.g., [132–137], and most recently have been also addressed in transport experiments with ultracold atoms [105].

In order to analyze the properties and efficiency of such quantum thermo-elements, one needs to identify the heat flow and power generated in the transport system. These flows can be identified using their classical relation to the entropy S according to

$$TdS = dU - \delta W, \quad (2.98)$$

that allows to relate the entropy production \dot{S} to the energy flow \dot{U} and the power \dot{W} via the equation

$$\dot{S} = \frac{1}{T} (\dot{U} - \dot{W}). \quad (2.99)$$

Therefore, in order to identify the steady-state energy flow and power, we need to investigate the steady-state entropy production.

Note, that we use the entropy as a starting point for this discussion since it directly connects to the BMS master equation [138]. This can be seen by considering the Shannon entropy of the system which is defined as

$$S(t) = - \sum_n p_n \ln(p_n), \quad (2.100)$$

where p_n is the probability to find the system in its eigenstate $|n\rangle$. Assuming that the probabilities obey a rate equation of the form presented in Eq. (2.70), we find that the time derivative of the Shannon entropy is given by

$$\dot{S}(t) = - \sum_n \dot{p}_n \ln(p_n) = - \sum_{\nu, n, m} \mathcal{W}_{n,m}^{(\nu)} p_m \ln(p_n). \quad (2.101)$$

Furthermore, we can use the trace-preserving property (2.62) of the rate matrix to rewrite the above equation in the form

$$\dot{S}(t) = \frac{1}{2} \sum_{\nu, n, m} [\mathcal{W}_{n,m}^{(\nu)} p_m - \mathcal{W}_{m,n}^{(\nu)} p_n] \left[\ln \left(\frac{p_m \mathcal{W}_{n,m}^{(\nu)}}{p_n \mathcal{W}_{m,n}^{(\nu)}} \right) + \ln \left(\frac{\mathcal{W}_{m,n}^{(\nu)}}{\mathcal{W}_{n,m}^{(\nu)}} \right) \right]. \quad (2.102)$$

The reason for the transformation to this form becomes clearer when we introduce the fluxes $J_{n,m}^{(\nu)}(t)$ and their corresponding driving forces $X_{n,m}^{(\nu)}(t)$ according to

$$J_{n,m}^{(\nu)}(t) = \mathcal{W}_{n,m}^{(\nu)} p_m(t) - \mathcal{W}_{m,n}^{(\nu)} p_n(t), \quad (2.103)$$

$$X_{n,m}^{(\nu)}(t) = \ln \left(\frac{p_m(t) \mathcal{W}_{n,m}^{(\nu)}}{p_n(t) \mathcal{W}_{m,n}^{(\nu)}} \right). \quad (2.104)$$

These definitions allow to rewrite the system entropy flow in Eq. (2.101) as a sum over an internal entropy production \dot{S}_i and an entropy flow \dot{S}_e to the environment into the system, i.e.,

$$\dot{S}(t) = \dot{S}_e(t) + \dot{S}_i(t). \quad (2.105)$$

Here, we defined the entropy flow to the environment according to

$$\dot{S}_e(t) = \frac{1}{2} \sum_{\nu, n, m} J_{n,m}^{(\nu)}(t) \ln \left(\frac{\mathcal{W}_{m,n}^{(\nu)}}{\mathcal{W}_{n,m}^{(\nu)}} \right), \quad (2.106)$$

and the internal entropy production as

$$\dot{S}_i(t) = \frac{1}{2} \sum_{\nu, n, m} J_{n,m}^{(\nu)}(t) X_{n,m}^{(\nu)}(t). \quad (2.107)$$

From the definition in Eq. (2.102), we observe that in systems where the relation

$$\mathcal{W}_{n,m}^{(\nu)} \bar{p}_m = \mathcal{W}_{m,n}^{(\nu)} \bar{p}_n, \quad (2.108)$$

is fulfilled, the total change of the entropy flow \dot{S} vanishes. Therefore, in such systems the internal entropy production becomes the negative entropy flow to the environment, i.e.,

$$\dot{S}_i(t) = -\dot{S}_e(t). \quad (2.109)$$

Within the following sections, we show that this relation is fulfilled for the considered systems. In fact, we find that the transition rates fulfill the local detailed balance relation

$$\frac{\mathcal{W}_{m,n}^{(\nu)}}{\mathcal{W}_{n,m}^{(\nu)}} = e^{\beta_\nu(\omega_{m,n} - \mu_\nu)}, \quad (2.110)$$

where $\omega_{m,n} = E_m - E_n$ is the involved transition energy. Therefore, we conclude that the steady-state entropy production of these system is given by the entropy flow from the environment to the system, which can be written as

$$\begin{aligned} \dot{S}_i = -\dot{S}_e &= -\sum_\nu \beta_\nu \left(\underbrace{\sum_{n,m} \omega_{m,n} \frac{\bar{J}_{n,m}^{(\nu)}}{2}}_{J_E^{(\nu)}} - \mu_\nu \underbrace{\sum_{n,m} \frac{\bar{J}_{n,m}^{(\nu)}}{2}}_{J_N^{(\nu)}} \right) \\ &= -\sum_\nu \beta_\nu \left(J_E^{(\nu)} - \mu_\nu J_N^{(\nu)} \right), \end{aligned} \quad (2.111)$$

where we identified the steady-state particle and energy currents $J_N^{(\nu)}$ and $J_E^{(\nu)}$, respectively. Furthermore, using the conservation of the total number of particles and the total energy in the steady-state from Eq. (2.96), we find

$$\dot{S}_i = -\Delta_\beta J_E + \Delta_{\beta\mu} J_N, \quad (2.112)$$

where we define the differences as

$$\begin{aligned} \Delta_\beta &= \beta_L - \beta_R, \\ \Delta_{\beta\mu} &= \beta_L \mu_L - \beta_R \mu_R. \end{aligned} \quad (2.113)$$

Subsequently, introducing the potential bias $\Delta_\mu = \mu_L - \mu_R$, and, without loss of generality, assuming a symmetric detuning, we rewrite the bath temperature and chemical potential as

$$\begin{aligned} \beta_L &= \beta + \frac{\Delta_\beta}{2}, \quad \beta_R = \beta - \frac{\Delta_\beta}{2}, \\ \mu_L &= \mu + \frac{\Delta_\mu}{2}, \quad \mu_R = \mu - \frac{\Delta_\mu}{2}. \end{aligned} \quad (2.114)$$

Inserting these results into Eq. (2.112), we find that the steady-state entropy production can be decomposed into

$$\bar{S}_i(T, \mu) = -(J_E - \mu J_N) \Delta_\beta + J_N \beta \Delta_\mu, \quad (2.115)$$

We note that the above equation assumes the usual flux and affinity form of the entropy flow [139]. In particular, we can identify the heat flow

$$\dot{Q} = -J_Q T \Delta_\beta, \quad (2.116)$$

with the usual heat flux given by

$$J_Q = J_E - \mu J_N, \quad (2.117)$$

and the additional power

$$\dot{W} = J_N \Delta_\mu. \quad (2.118)$$

The Eq. (2.115) allows to calculate the linear response transport coefficients of the thermocouple by applying the Onsager theorem, which we discuss in more detail within the next section.

2.14 Onsager theorem

From classical electronic transport it is well known that the Onsager theorem [140, 141] is very useful for describing linear, purely resistive systems. This theorem has been analyzed and proven to be also valid for open quantum systems [133, 142]. In particular, the Onsager theorem holds for open quantum systems which can be described by Markovian master equations [143–145], i.e., for the systems we discuss within this thesis. Such systems are the quantum mechanical analog to purely resistive classical systems, i.e., systems without memory. Within this section, we demonstrate how to apply this theorem in order to extract the linear response transport coefficients for Markovian quantum systems. In particular, we compare the Onsager theorem for a constant chemical potential and a chemical potential that depends on temperature and particle density as obtained from a full grand-canonical derivation (compare with Sec. 4.1.1)

2.14.1 Constant chemical potential

In order to appropriately describe an irreversible transport process, one rewrites the steady-state entropy production as a sum

$$\bar{S}_i = \sum_{j=1}^2 \mathcal{J}_j \cdot \mathcal{F}_j, \quad (2.119)$$

over generalized fluxes \mathcal{J}_j and their corresponding affinities \mathcal{F}_j [139]. In classical electronic transport theory the chemical potential is assumed to be constant and thus independent of the reservoir temperature and particle number. Comparing with Eq. (2.115) and using the definitions from Eqs. (2.116)-(2.118), we conclude that the generalized fluxes are given by

$$\mathcal{J}_1 = -J_Q, \quad \mathcal{J}_2 = J_N, \quad (2.120)$$

with the corresponding affinities

$$\mathcal{F}_1 = \Delta_\beta, \quad \mathcal{F}_2 = \beta \Delta_\mu. \quad (2.121)$$

In the following, we focus on the linear response equations only, i.e., we assume that the bias Δ_β and Δ_μ are small. By linearizing the currents in Eq. (2.120) with respect to the affinities from Eq. (2.121) around the equilibrium ($\Delta_\beta = 0$, $\Delta_\mu = 0$), we can describe the linear response of generalized fluxes to small variations of the affinities. This procedure yields the so-called linear Onsager system of equations in the form

$$\begin{pmatrix} -J_Q \\ J_N \end{pmatrix} = \begin{pmatrix} L_{11} & L_{12} \\ L_{21} & L_{22} \end{pmatrix} \begin{pmatrix} \Delta_\beta \\ \beta \Delta_\mu \end{pmatrix} \equiv \mathbf{M} \begin{pmatrix} \Delta_\beta \\ \beta \Delta_\mu \end{pmatrix}, \quad (2.122)$$

where the entries of the Onsager matrix \mathbf{M} with constant chemical potential μ are defined as partial derivatives evaluated at the equilibrium values,

$$L_{ij} = \left. \frac{\partial \mathcal{J}_i}{\partial \mathcal{F}_j} \right|_0. \quad (2.123)$$

These so-called kinetic coefficients fulfill the Onsager reciprocal relation

$$L_{12} = L_{21}, \quad (2.124)$$

which is related to the time reversal symmetry of physical laws [139]. Furthermore, the Onsager matrix is positive-definite, which in the linear response regime guarantees the positivity of the entropy production in accordance with the second law of thermodynamics.

From the Onsager system in Eq. (2.122), one can subsequently extract the linear transport relations for different setups. Considering the particle current if no thermal bias, i.e., $\Delta_T = T_L - T_R$, is present, one finds Ohm's law

$$J_N = \sigma \Delta_\mu, \text{ for } \Delta_T = 0, \quad (2.125)$$

with the linear conductance determined by

$$\sigma = \frac{L_{22}}{T}. \quad (2.126)$$

Similarly one finds Fourier's law in the form

$$J_Q = -\kappa\Delta_T, \text{ for } J_N = 0, \quad (2.127)$$

for a thermocouple under the constraint of vanishing particle current. This defines the linear heat conductance

$$\kappa = \frac{D}{T^2 L_{22}}, \quad (2.128)$$

where $D = \det(\mathbf{M})$ is the determinant of the Onsager matrix in Eq. (2.122). Here, we emphasize the fact that for systems in the tight-coupling limit, where $J_N = \omega J_E$, the determinant and, thus, linear heat conductance vanishes. This behavior correctly reflects the fact, that in systems with a single transition frequency there can not be an energy transport without an accompanied particle transport.

Additionally, systems with more than one single transition frequency can produce a potential bias

$$\Delta_\mu = \Sigma\Delta_T, \text{ for } J_N = 0, \quad (2.129)$$

as a linear response to a thermal bias at vanishing particle current. This so-called Seebeck effect is characterized by the coefficient Σ , also known as thermopower, which is defined by

$$\Sigma = \frac{L_{21}}{T L_{22}}. \quad (2.130)$$

The reverse process, where a thermal bias is created by applying a bias in the chemical potentials, is known as Peltier effect which is characterized by the Peltier coefficient

$$\Pi = T\Sigma. \quad (2.131)$$

The efficiency of these processes can be characterized by the dimensionless figure-of-merit [146]

$$ZT = \frac{\Sigma^2}{L} = \frac{L_{12}^2}{D}, \quad (2.132)$$

with the Lorenz number $L = \kappa/(T\sigma)$ defined by the Wiedemann-Franz law [147]. Although this quantity is widely used in theoretical and experimental studies, it is mainly a qualitative measure since it has no upper bound in contrast to the efficiency η , which can only assume values in the range $[0, 1]$. Therefore, we also consider the proper efficiency which is defined as the ratio between extracted power and applied heat energy, i.e.,

$$\eta = \frac{\dot{W}}{J_Q}. \quad (2.133)$$

Using the affinity-flux form from Eq. (2.119), and the linearized Onsager system from Eq. (2.122), we find the linear response relation

$$\frac{\eta}{\eta_C} = \frac{\mathcal{J}_2 \mathcal{F}_2}{\mathcal{J}_1 \mathcal{F}_1} = \frac{L_{21} \mathcal{F}_1 \mathcal{F}_2 + L_{22} \mathcal{F}_2^2}{L_{11} \mathcal{F}_1^2 + L_{12} \mathcal{F}_1 \mathcal{F}_2} = K \frac{L_{21} + K L_{22}}{L_{11} + K L_{12}}, \quad (2.134)$$

with the Carnot efficiency

$$\eta_C = \frac{\Delta_T}{T}. \quad (2.135)$$

and the abbreviation $K = \mathcal{F}_2/\mathcal{F}_1$. Most interesting is the efficiency for the configuration of thermodynamic forces that yield the maximum power. From the equation

$$\dot{W} = \mathcal{J}_2 \mathcal{F}_2 T = (L_{21} \mathcal{F}_1 \mathcal{F}_2 + L_{22} \mathcal{F}_2^2) T, \quad (2.136)$$

we see that the power assumes a maximum at $\mathcal{F}_2^{\max} = \mathcal{F}_2^{\text{stop}}/2$, half the stopping force $\mathcal{F}_2^{\text{stop}} = -L_{21} \mathcal{F}_1 / L_{22}$, for which the particle current vanishes, i.e., $J_N = 0$. With this result, we calculate the efficiency at maximum power [148] which reads as

$$\eta = \frac{1}{2} \eta_C \frac{q^2}{2 - q^2} \geq 0. \quad (2.137)$$

Here, we define the dimensionless coupling

$$q = \frac{L_{12}}{\sqrt{L_{11} L_{22}}} = \sqrt{\frac{ZT}{1 + ZT}}, \quad (2.138)$$

which is restricted to the values $-1 \leq q \leq 1$. This result relates to the fact that the Onsager matrix is positive-definite and, hence, the relation $|L_{12}| \leq \sqrt{L_{11} L_{22}}$ is fulfilled. We note, that the efficiency at maximum power can at most be equal to half the Carnot efficiency. This maximum is reached for the ideal coupling $|q| = 1$, i.e., in the limit $ZT \rightarrow \infty$. It corresponds to the maximum possible value in the framework of linear response theory, the Curzon-Ahlborn [149] upper bound

$$\eta_{\max} = 1 - \sqrt{\frac{T_2}{T_1}} \sim \frac{\Delta_T}{2T} \quad \text{for } T_1 > T_2. \quad (2.139)$$

2.14.2 Temperature and density dependent chemical potential

In the previous section, we derived the linear transport coefficients assuming that the only present forces which drive the system are given by the inverse temperature bias Δ_β and the chemical potential bias Δ_μ . However, there are transport setups where such a treatment is not entirely correct. For example, in setups that require a grand-canonical description, one usually obtains a chemical potential $\mu(T, n)$ that

depends on the reservoir temperature T and the particle density n . Respective transport setups are discussed in Ch. 4. Here, the forces that drive the generalized currents through the system depend on the difference in temperature and/or a difference in the particle densities of the attached reservoirs. Therefore, one has to rewrite the potential bias Δ_μ in the entropy production from Eq. (2.115) in terms of this new basis. In general, the chemical potential does not depend linearly on the temperature and density bias, which results in a nonlinear dependence of the entropy production on these driving forces.

Nevertheless, since we are only interested in the linear response transport regime where the applied potential bias is assumed to be very small, we can safely assume that it depends linearly on temperature and density differences. Hence, we can expand the potential bias around the equilibrium to lowest order, i.e.,

$$\Delta_\mu \cong \left. \frac{\partial \mu}{\partial \beta} \right|_0 \Delta_\beta + \left. \frac{\partial \mu}{\partial n} \right|_0 \Delta_n + \mathcal{O}(\Delta_\beta \Delta_n), \quad (2.140)$$

where we introduce the particle density bias $\Delta_n = n_L - n_R$ between the two reservoirs. Inserting this expansion into Eq. (2.115) yields

$$\tilde{S}_i(T, n) = - \left(J_E - \mu J_N - \beta \frac{\partial \mu}{\partial \beta} J_N \right) \Delta_\beta + \beta J_N \frac{\partial \mu}{\partial n} \Delta_n. \quad (2.141)$$

Comparing this result with the decomposition from Eq. (2.119), we find that for the case of a temperature- and particle density dependent chemical potential the generalized fluxes are given by

$$\mathcal{J}_1 = -\tilde{J}_Q, \quad \mathcal{J}_2 = J_N, \quad (2.142)$$

with the corresponding affinities

$$\mathcal{F}_1 = \Delta_\beta, \quad \mathcal{F}_2 = \beta \frac{\partial \mu}{\partial n} \Delta_n. \quad (2.143)$$

In analogy to Eq. (2.117), we define the generalized heat flux as

$$\tilde{J}_Q = J_E - \left(\mu + \beta \frac{\partial \mu}{\partial \beta} \right) J_N, \quad (2.144)$$

which formally corresponds to the conventional heat flux with a modified chemical potential. Now, we can also identify the power generated by the thermocouple. Comparing Eq. (2.141) with Eq. (2.99), we obtain the power

$$\dot{W} = J_N \frac{\partial \mu}{\partial n} \Delta_n, \quad (2.145)$$

which is generated under the influence of the heat flow

$$\dot{Q} = -\tilde{J}_Q T \Delta_\beta. \quad (2.146)$$

Note that the choice of the affinities in Eq. (2.143) is not unique. Because the derivative $\partial\mu/\partial n$ is evaluated at the equilibrium it can be also absorbed in the definition of the current. In fact, this specific derivative can be related to the inverse compressibility at constant volume c_V [150] of the gas

$$c_V = \frac{1}{n^2} \left. \frac{\partial n}{\partial \mu} \right|_0. \quad (2.147)$$

Due to dimensional reasons, we choose the affinities as defined in Eq. (2.143). As a result, all transport coefficients we derive below, have the same physical dimension as for the case of a constant chemical potential. Additionally, we can immediately identify the physical meaning of the generalized fluxes as particle and heat currents, which are measurable in an experiment. Finally, we note that the affinity \mathcal{F}_2 can be interpreted as an effective chemical potential bias which is induced by a density imbalance between the reservoirs. Hence, the generated powers in Eq. (2.118) and Eq. (2.145) have also the same physical meaning.

In order to extract the transport coefficients, we again linearize the generalized fluxes from Eq. (2.142) with respect to the affinities from Eq. (2.143) and obtain a Onsager system of equations in analogy to Eq. (2.122) which reads as

$$\begin{pmatrix} -\tilde{J}_Q \\ J_N \end{pmatrix} = \begin{pmatrix} \tilde{L}_{11} & \tilde{L}_{12} \\ \tilde{L}_{21} & \tilde{L}_{22} \end{pmatrix} \begin{pmatrix} \Delta_\beta \\ \beta \frac{\partial \mu}{\partial n} \Delta_n \end{pmatrix} \equiv \tilde{\mathbf{M}} \begin{pmatrix} \Delta_\beta \\ \beta \frac{\partial \mu}{\partial n} \Delta_n \end{pmatrix}, \quad (2.148)$$

where the kinetic coefficients $\tilde{L}_{ij} = \partial \mathcal{J}_i / \partial \mathcal{F}_j$ are now functionals of the chemical potential $\mu(T, n)$. Due to the linearity of the system of equations in Eq. (2.122) and Eq. (2.148), and the respective generalized currents and their affinities, we can find a linear mapping which transforms the Onsager matrices \mathbf{M} and $\tilde{\mathbf{M}}$ into each other. Hence, we can rewrite the matrix $\tilde{\mathbf{M}}$ using the kinetic coefficients defined in Eq. (2.122), which now become functionals of the temperature- and density-dependent chemical potential, i.e., $L_{ij}(\mu) \rightarrow L_{ij}[\mu(T, n)]$. This yields

$$\tilde{\mathbf{M}} = \begin{pmatrix} L_{11} + \beta \frac{\partial \mu}{\partial \beta} \left(2L_{12} + \frac{\partial \mu}{\partial \beta} L_{22} \right) & L_{12} + \beta \frac{\partial \mu}{\partial \beta} L_{22} \\ L_{21} + \beta \frac{\partial \mu}{\partial \beta} L_{22} & L_{22} \end{pmatrix}. \quad (2.149)$$

We observe that the Onsager reciprocal relation is preserved, i.e.,

$$L_{12} = L_{21} \implies \tilde{L}_{12} = \tilde{L}_{21}. \quad (2.150)$$

Note that for another choice of the affinity \mathcal{F}_2 and the corresponding current, the kinetic coefficients in Eq. (2.148) become modified, such that the Onsager reciprocal relation might be violated. Furthermore, it becomes more complicated to relate the currents, and subsequently the transport coefficients, to physical observables.

The linear response transport coefficients are obtained in analogy to the previous section. Hence, the particle current in the absence of a thermal bias is described in

analogy to Ohm's law by the relation

$$\tilde{\sigma} \equiv \frac{J_N}{\frac{\partial \mu}{\partial n} \Delta_n} = \frac{\tilde{L}_{22}}{T} = \sigma[\mu(T, n)], \text{ for } \Delta_T = 0, \quad (2.151)$$

for the matter conductance $\tilde{\sigma}(T, n)$. In a similar way to the matter conductance, we can extract the analog of the thermal conductance $\tilde{\kappa}$ from the modified Fourier's law $\tilde{J}_Q = -\tilde{\kappa} \Delta_T$ under the constraint of a vanishing particle current, which yields

$$\tilde{\kappa} \equiv -\frac{\tilde{J}_Q}{\Delta_T} = \frac{\tilde{D}}{T^2 \tilde{L}_{22}} = \kappa[\mu(T, n)], \text{ for } J_N = 0. \quad (2.152)$$

Here, $\tilde{D} = \det(\tilde{M})$ is the determinant of the Onsager Matrix \tilde{M} from Eq. (2.149). In analogy to the Wiedemann-Franz law, we define the modified Lorenz number as

$$\tilde{L} = \frac{\tilde{\kappa}}{T \tilde{\sigma}} = \frac{\tilde{D}}{(T \tilde{L}_{22})^2}. \quad (2.153)$$

Furthermore, we find that a vanishing particle current for finite thermal and density bias implies

$$\beta \frac{\partial \mu}{\partial n} \Delta_n = \frac{\tilde{L}_{21}}{T^2 \tilde{L}_{22}} \Delta_T, \text{ for } J_N = 0. \quad (2.154)$$

Therefore, such a thermodynamic device produces a density induced chemical potential bias as a response to a thermal bias. This allows us to define $\tilde{\Sigma}$ analogous to the thermopower by

$$\tilde{\Sigma} \equiv \frac{\frac{\partial \mu}{\partial n} \Delta_n}{\Delta_T} = \frac{\tilde{L}_{21}}{T \tilde{L}_{22}} = \Sigma[\mu(T, n)] + \beta^2 \frac{\partial \mu}{\partial \beta}. \quad (2.155)$$

This coefficient characterizes the linear density response to a temperature difference at vanishing particle current. It is related to the analog of the modified Peltier coefficient $\tilde{\Pi}$ by the Thomson relation

$$\tilde{\Pi} = T \tilde{\Sigma}. \quad (2.156)$$

Using the transport coefficients defined in Eq. (2.153) and Eq. (2.155), we can calculate the dimensionless figure-of-merit $\tilde{Z}T$ which characterizes the efficiency of the thermodynamic device. It is given by

$$\tilde{Z}T \equiv \frac{\tilde{\Sigma}^2}{\tilde{L}} = ZT[\mu(T, n)] + \frac{\beta^2 \frac{\partial \mu}{\partial \beta} \left(\beta^2 \frac{\partial \mu}{\partial \beta} + 2\Sigma[\mu(T, n)] \right)}{L[\mu(T, n)]}. \quad (2.157)$$

Finally, we can calculate the efficiency at maximum power for this setup which reads as

$$\tilde{\eta} = \frac{1}{2}\eta_C \frac{\tilde{q}^2}{2 - \tilde{q}^2} \geq 0, \quad \text{with} \quad \tilde{q} = \frac{\tilde{L}_{12}}{\sqrt{\tilde{L}_{11}\tilde{L}_{22}}}. \quad (2.158)$$

From the definitions in the Eqs. (2.151)-(2.158), we see that for an independent chemical potential, where the derivative with respect to temperature $\partial\mu/\partial\beta$ vanishes, we recover the usual linear response transport coefficients from Sec. 2.14.1.

Chapter 3

Interacting transport qubits

Within this chapter we extend the research that cumulated in the publication in Ref. [151].

The weak-coupling master equation approach derived in the previous chapter is well suited to describe quantum transport through mesoscopic structures. This category of physical systems is basically defined by their physical dimensions which normally are in the range of a few nanometers to hundreds of microns. Hence, such systems are usually much larger than microscopic structures like atoms or molecules but not large enough to be described as classical ohmic conductors.

Nowadays, such mesoscopic systems can be routinely fabricated using a variety of different materials and geometries. The fact that these systems cover a wide field of interesting applications, for example as detectors [26, 27, 152], single quanta-, particle- and spin sources [24, 25, 127], constituents of quantum computers [35, 37, 39, 46, 49, 50] or quantum simulators [30, 153–157], to name but a few, has lead to intensive studies over the last decades. Consequently, the quantum master equation theory has been very successfully applied to several of these systems.

Motivated by the ever increasing interest and ongoing advances in this field of physics, we now study the steady-state transport properties of a mesoscopic setup consisting of two capacitively coupled double quantum dots (DQDs) which are additionally exposed to an impurity. We decided to investigate this DQD system due to its possible utilization as building block of a future quantum computer. In such devices the classical bit is replaced by a quantum mechanical qubit (QB) as the basic unit of computation and these qubits can for example be experimentally implemented by DQDs [40, 43, 44, 48]. They are interesting candidates, since their solid-state implementation is in principle scalable. However, industrial production of such quantum dots (QDs) on a large scale will inevitable face the problem of unwanted impurities [55]. Therefore, we additionally include an impurity between the two coupled DQDs, which we model as charge-qubit (CQB).

In the first part of this chapter, we study the effect of the impurity on the transport properties of the double quantum dot system and in the second part, we focus on the question if the impurity can also have desirable effects for example in the context of the creation of entanglement.

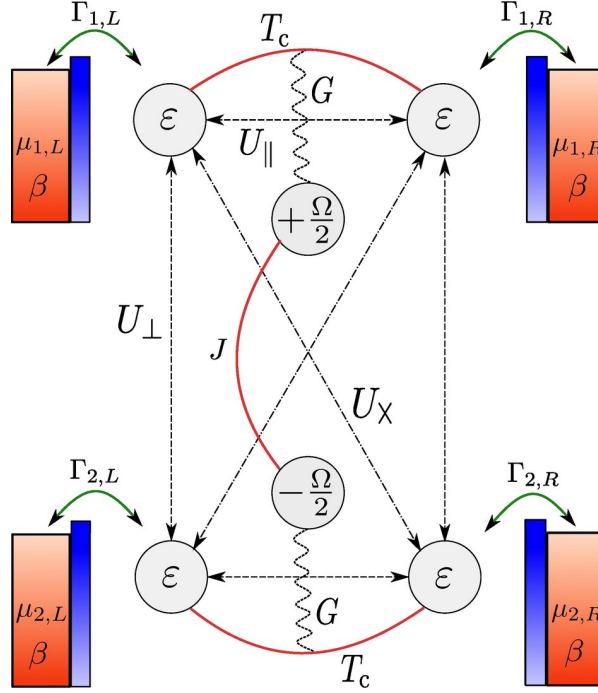


Figure 3.1: Two double quantum dots 1 and 2 with electronic dot energies ε , coherent tunneling amplitude (solid lines) T_c , and on-site Coulomb interaction (dashed lines) U_{\parallel} interact capacitively via perpendicular and diagonal Coulomb interactions U_{\perp} and U_{χ} , respectively. Transport is enabled by tunnel coupling the quantum dots (i, α) to adjacent fermionic reservoirs of chemical potential $\mu_{i,\alpha}$ and inverse temperature β with the tunneling rate $\Gamma_{i,\alpha}$. A charge-qubit with detuning Ω and tunneling amplitude J modifies the tunnel amplitudes of both DQDs by G (wavy lines) depending on the position of the CQB electron.

3.1 System Hamiltonian

We consider an experimental setup as depicted in Fig. 3.1, which consists of two parallel double quantum dots that are coupled both capacitively and via a perpendicularly aligned charge qubit (CQB) impurity. These DQDs are coupled to leads that act as reservoirs for electrons and, thus, allow for electronic transport when their parameters, i.e., their chemical potentials are chosen differently. To simplify the calculations, we explicitly assume spin-polarized electronic leads and neglect the spin degree of freedom throughout this chapter. This implies that spin-selection effects as observed in Ref. [57] do not matter.

The Hamiltonian of the full system can be decomposed according to Eq. (2.1) into a sum over the system Hamiltonian $\hat{\mathcal{H}}_S$, the bath Hamiltonian $\hat{\mathcal{H}}_B$ and the Hamiltonian $\hat{\mathcal{H}}_I$ describing the coupling between system and bath. In the considered setup,

the system Hamiltonian consist of several contributions from the two DQDs, which we label by $i \in \{1, 2\}$, the CQB and their respective couplings. It can be written in the form

$$\hat{\mathcal{H}}_S = \hat{\mathcal{H}}_{\text{DQDs}} + \hat{\mathcal{H}}_{\text{CQB}} + \hat{\mathcal{H}}_{\text{int}}, \quad (3.1)$$

where the Hamiltonian that describes the DQDs reads as

$$\hat{\mathcal{H}}_{\text{DQDs}} = \sum_{i=1}^2 \hat{\mathcal{H}}_{\text{DQD}}^{(i)} + \hat{\mathcal{H}}_{\perp} + \hat{\mathcal{H}}_{\times}. \quad (3.2)$$

For convenience, we use here and in the following discussion the notation $i = 1$ for the upper and $i = 2$ for the lower transport channel in Fig. 3.1, whereas the labels L, R denote the left and right quantum dots and electronic baths, respectively. In consequence, each single DQD is described by the Hamiltonian

$$\hat{\mathcal{H}}_{\text{DQD}}^{(i)} = \varepsilon (\hat{d}_{i,L}^\dagger \hat{d}_{i,L} + \hat{d}_{i,R}^\dagger \hat{d}_{i,R}) + T_c (\hat{d}_{i,L}^\dagger \hat{d}_{i,R} + \hat{d}_{i,R}^\dagger \hat{d}_{i,L}) + U_{\parallel} \hat{d}_{i,L}^\dagger \hat{d}_{i,L} \hat{d}_{i,R}^\dagger \hat{d}_{i,R}, \quad (3.3)$$

where the operators $\hat{d}_{i,\alpha}$ and $\hat{d}_{i,\alpha}^\dagger$ annihilate and create electrons in the QD $\alpha \in \{R, L\}$ of the DQD $i \in \{1, 2\}$. They fulfill fermionic anti-commutation relations

$$\{\hat{d}_{i,\alpha}, \hat{d}_{j,\beta}^\dagger\} = \delta_{ij} \delta_{\alpha\beta}, \quad \text{and} \quad \{\hat{d}_{i,\alpha}^\dagger, \hat{d}_{j,\beta}^\dagger\} = \{\hat{d}_{i,\alpha}, \hat{d}_{j,\beta}\} = 0. \quad (3.4)$$

Furthermore, we assume that all quantum dots have the same dot energy ε and each DQD has the same coherent tunneling amplitude T_c and Coulomb interaction strength U_{\parallel} . Additionally, the two DQD can interact capacitively with each other which gives rise to the DQD cross coupling Hamiltonians

$$\hat{\mathcal{H}}_{\perp} = U_{\perp} (\hat{d}_{1,L}^\dagger \hat{d}_{1,L} \hat{d}_{2,L}^\dagger \hat{d}_{2,L} + \hat{d}_{1,R}^\dagger \hat{d}_{1,R} \hat{d}_{2,R}^\dagger \hat{d}_{2,R}), \quad (3.5)$$

that describes the capacitive interaction between charged parallel aligned quantum dots parametrized by the interaction strength U_{\perp} , and

$$\hat{\mathcal{H}}_{\times} = U_{\times} (\hat{d}_{1,L}^\dagger \hat{d}_{1,L} \hat{d}_{2,R}^\dagger \hat{d}_{2,R} + \hat{d}_{1,R}^\dagger \hat{d}_{1,R} \hat{d}_{2,L}^\dagger \hat{d}_{2,L}), \quad (3.6)$$

which describes the capacitive interaction between the charged transverse aligned quantum dots parametrized by the interaction strength U_{\times} .

The CQB is introduced in the setup as an effective DQD filled with exactly one electron which is perpendicularly aligned with respect to the two parallel transport DQDs. Thus, it can be described as an effective two-level Hamiltonian of the form

$$\hat{\mathcal{H}}_{\text{CQB}} = \frac{\Omega}{2} \hat{\sigma}_z + J \hat{\sigma}_x, \quad (3.7)$$

where we introduce the Pauli matrices $\hat{\sigma}_z$ and $\hat{\sigma}_x$ which are defined as

$$\hat{\sigma}_z = \hat{c}_1^\dagger \hat{c}_1 - \hat{c}_2^\dagger \hat{c}_2, \quad \text{and} \quad \hat{\sigma}_x = \hat{c}_1^\dagger \hat{c}_2 + \hat{c}_2^\dagger \hat{c}_1. \quad (3.8)$$

The operators \hat{c}_i and \hat{c}_i^\dagger annihilate and create an electron in the QD i of the CQB. They also obey fermionic anti-commutation relations of the form

$$\{\hat{c}_i, \hat{c}_j^\dagger\} = \delta_{ij}, \quad \text{and} \quad \{\hat{c}_i^\dagger, \hat{c}_j^\dagger\} = \{\hat{c}_i, \hat{c}_j\} = 0. \quad (3.9)$$

The CQB is characterized by the detuning Ω and coherent tunneling amplitude J .

In the considered setup, the electronic transport through each DQD is altered by the state of the nearby CQB impurity. In particular, the current through the DQD closest to the charge of the CQB is suppressed due to Coulomb repulsion. We account for this interaction by phenomenologically introducing the additional coupling Hamiltonian $\hat{\mathcal{H}}_{\text{int}}$ between the DQDs and the CQB which reads as

$$\hat{\mathcal{H}}_{\text{int}} = \frac{G}{2} \left[(\mathbb{1} + \hat{\sigma}_z) (\hat{d}_{1,L}^\dagger \hat{d}_{1,R} + \hat{d}_{1,R}^\dagger \hat{d}_{1,L}) + (\mathbb{1} - \hat{\sigma}_z) (\hat{d}_{2,L}^\dagger \hat{d}_{2,R} + \hat{d}_{2,R}^\dagger \hat{d}_{2,L}) \right]. \quad (3.10)$$

According to this Hamiltonian, the influence of the CQB on the transport DQDs is as follows: The intrinsic tunneling processes of the DQDs are modified by the parameter G in the presence of an electron in the respective dot of the CQB. Due to Coulomb repulsion, it is reasonable to assume that the presence of an electron in the CQB leads to a suppression of the tunneling amplitude T_c in the respective DQD. Thus, we phenomenologically restrict the parameter G to negative values, i.e.,

$$0 > G \geq -T_c. \quad (3.11)$$

Furthermore, we assume that each QD of the setup can at most be filled with one electron. Thus, the minimum amount of electrons in the whole system is 1, corresponding to the electron contained within the CQB, and the maximum amount is 4+1, with four electrons in the two DQDs and one electron in the CQB. This assumption fixes the dimension of the system Hamiltonian to $d = 2^5 = 32$. Since the electron in the CQB is always present, we focus in the following only on the electrons in the DQDs. We introduce the local basis of the system in the form

$$|a, b, c\rangle = \underbrace{|a\rangle_1}_{\text{DQD}_1} \otimes \underbrace{|b\rangle_2}_{\text{DQD}_2} \otimes \underbrace{|c\rangle}_{\text{CQB}}, \text{ with } a, b \in \{ \underbrace{0}_{0e^-}, \underbrace{L}_{1e^-}, \underbrace{R}_{2e^-}, \underbrace{LR}_{2e^-} \}, \quad c \in \{\uparrow, \downarrow\}. \quad (3.12)$$

Thus, the basis states are given by a tensor product of the local states of the two DQDs and the CQB where the labels L, R denote a filled left or right QD, respectively. Using this definition, we can extract the explicit representation of the full system Hamiltonian from Eq. (3.1) in the local basis. We find that in this representation the system Hamiltonian assumes a block diagonal form. Along the diagonal of the Hamiltonian there are 9 blocks each representing a subspace with fixed electron number in the DQDs. There are four (2×2) blocks corresponding to the situation that both DQD are completely filled, completely empty or one of the DQDs is completely filled whereas the other one is completely empty. Then there are four

(4×4) blocks corresponding to the situation that one DQD is completely filled or completely empty whereas the other DQD is filled with exactly one electron. Finally, there is one (8×8) block which corresponds to the situation that both DQDs are filled with exactly one electron. Obviously, this specific block structure emerges because we do not allow for electrons to tunnel between the DQDs and the CQB. Therefore, transitions between the different electronic subspaces can only be induced by the environment due to the tunneling of electrons from the reservoirs into the system and vice versa. Accordingly, we lastly take a look at the environment which is connected to the system.

Each quantum dot of the DQD system is weakly coupled to an electronic bath, which we model as a free electron gas of spin-polarized electrons. Hence, the full bath Hamiltonian is given as a sum

$$\hat{\mathcal{H}}_B = \sum_{i=1}^2 \sum_{\alpha \in \{L, R\}} \hat{\mathcal{H}}_B^{(i, \alpha)}, \quad (3.13)$$

over all connected reservoirs (i, α) that are described by the Hamiltonians

$$\hat{\mathcal{H}}_B^{(i, \alpha)} = \sum_{k=0}^{\infty} \nu_{i, \alpha, k} \hat{q}_{i, \alpha, k}^\dagger \hat{q}_{i, \alpha, k}, \quad (3.14)$$

respectively. Here, we introduce the operators $\hat{q}_{i, \alpha, k}^\dagger$ and $\hat{q}_{i, \alpha, k}$ that create and annihilate an electron with momentum k and energy $\nu_{i, \alpha, k}$ in the reservoir (i, α) . Each of the reservoirs is in a thermal equilibrium state described by the density matrix

$$\bar{\rho}_{i, \alpha} = \frac{e^{\beta(\hat{\mathcal{H}}_B^{(i, \alpha)} - \mu_{i, \alpha} \hat{N}^{(i, \alpha)})}}{\text{Tr} \left\{ e^{\beta(\hat{\mathcal{H}}_B^{(i, \alpha)} - \mu_{i, \alpha} \hat{N}^{(i, \alpha)})} \right\}}, \quad (3.15)$$

with the global inverse temperature $\beta = 1/T$ and the local chemical potentials $\mu_{i, \alpha}$ which fixes the mean electron number $\bar{N}^{(i, \alpha)} = \langle \hat{N}^{(i, \alpha)} \rangle$ in each lead. Furthermore, the reservoirs obey the commutator $[\hat{\mathcal{H}}_B^{(i, \alpha)}, \hat{N}^{(i, \alpha)}] = 0$, such that the steady-state fulfills

$$[\hat{\mathcal{H}}_B^{(i, \alpha)}, \bar{\rho}_{i, \alpha}] = 0. \quad (3.16)$$

The quantum dots couple weakly to their respective reservoirs via quantum mechanical tunneling processes, such that we can define the full system-bath interaction Hamiltonian as

$$\hat{\mathcal{H}}_I = \sum_{i, \alpha, k} (t_{i, \alpha, k} \hat{d}_{i, \alpha} \hat{q}_{i, \alpha, k}^\dagger + \text{h. c.}), \quad (3.17)$$

where the tunneling amplitude of an electron hopping from the lead (i, α) into the system or vice versa is proportional to $t_{i, \alpha, k}^*$ and $t_{i, \alpha, k}$, respectively.

3.2 Liouvillian

In order to derive the BMS master equation for the considered fermionic setup according to the results within Sec. 2, we start by rewriting the interaction Hamiltonian from Eq. (3.17) in the form presented in Eq. (2.9). Here, the complete interaction Hamiltonian reads as

$$\hat{\mathcal{H}}_I = \sum_{i,\alpha} \hat{d}_{i,\alpha} \sum_k t_{i,\alpha,k} \hat{q}_{i,\alpha,k}^\dagger - \sum_{i,\alpha} \hat{d}_{i,\alpha}^\dagger \sum_k t_{i,\alpha,k} \hat{q}_{i,\alpha,k}, \quad (3.18)$$

where the $(-)$ sign arises due to the anti-commutation relation $\{\hat{d}_{i,\alpha}, \hat{q}_{i,\alpha,k}^\dagger\} = 0$. We note that the fermionic interaction Hamiltonian contradicts the form postulated in Eq. (2.9). However, we can use, e.g., a Jordan-Wigner transformation [158, 159] that decomposes the fermionic operators $\hat{d}_{i,\alpha}$ and $\hat{q}_{i,\alpha,k}$ into tensor products of Pauli matrices. This allows to define new fermionic operators in the form

$$\begin{aligned} \tilde{d}_{1,L} &= \sigma_- \otimes \mathbb{1} \otimes \mathbb{1} \otimes \mathbb{1} \otimes \mathbb{1}, & \tilde{d}_{1,R} &= \sigma_z \otimes \sigma_- \otimes \mathbb{1} \otimes \mathbb{1} \otimes \mathbb{1}, \\ \tilde{d}_{2,L} &= \sigma_z \otimes \sigma_z \otimes \sigma_- \otimes \mathbb{1} \otimes \mathbb{1}, & \tilde{d}_{2,R} &= \sigma_z \otimes \sigma_z \otimes \sigma_z \otimes \sigma_- \otimes \mathbb{1}, \end{aligned} \quad (3.19)$$

and

$$\tilde{q}_{i,\alpha,k} = \underbrace{\sigma_z \otimes \dots \otimes \sigma_z}_{k-1} \otimes \sigma_- \otimes \mathbb{1} \otimes \dots \otimes \mathbb{1} \quad (3.20)$$

Here, we introduced the composite Pauli matrices $\sigma_\pm = \frac{1}{2}(\sigma_x \pm i\sigma_y)$ which have the property $(\sigma_-)^\dagger = \sigma_+$, and the unity matrix in two dimensions $\mathbb{1}$. Now, using the fact that the Pauli matrix σ_z is self adjoint and that the products with the composite Pauli matrices is given by $\sigma_- \sigma_z = \sigma_-$ and $\sigma_+ \sigma_z = -\sigma_+$, we find that the interaction Hamiltonian assumes the desired form

$$\hat{\mathcal{H}}_I = \sum_{i,\alpha,k} \left(\tilde{d}_{i,\alpha} \otimes \sum_k t_{i,\alpha,k} \tilde{q}_{i,\alpha,k}^\dagger + \tilde{d}_{i,\alpha}^\dagger \otimes \sum_k t_{i,\alpha,k} \tilde{q}_{i,\alpha,k} \right). \quad (3.21)$$

In the following, we implicitly assume that the fermionic operators are given in their Jordan-Wigner representation shown in Eq. (3.19) and Eq. (3.20), Therefore, we now drop the tilde above the new fermionic operators again.

By comparing the transformed interaction Hamiltonian from Eq. (3.21) with the decomposition in Eq. (2.9), we can identify the system operators

$$\hat{A}_1 = \hat{d}_{1,L}, \hat{A}_2 = \hat{d}_{1,L}^\dagger, \hat{A}_3 = \hat{d}_{1,R}, \hat{A}_4 = \hat{d}_{1,R}^\dagger, \hat{A}_5 = \hat{d}_{2,L}, \hat{A}_6 = \hat{d}_{2,L}^\dagger, \hat{A}_7 = \hat{d}_{2,R}, \hat{A}_8 = \hat{d}_{2,R}^\dagger, \quad (3.22)$$

and their corresponding bath operators

$$\begin{aligned} \hat{B}_1 &= \sum_k t_{1,L,k} \hat{q}_{1,L,k}^\dagger, \hat{B}_2 = \sum_k t_{1,L,k}^* \hat{q}_{1,L,k}, \hat{B}_3 = \sum_k t_{1,R,k} \hat{q}_{1,R,k}^\dagger, \hat{B}_4 = \sum_k t_{1,R,k}^* \hat{q}_{1,R,k}, \\ \hat{B}_5 &= \sum_k t_{2,L,k} \hat{q}_{2,L,k}^\dagger, \hat{B}_6 = \sum_k t_{2,L,k}^* \hat{q}_{2,L,k}, \hat{B}_7 = \sum_k t_{2,R,k} \hat{q}_{2,R,k}^\dagger, \hat{B}_8 = \sum_k t_{2,R,k}^* \hat{q}_{2,R,k}. \end{aligned} \quad (3.23)$$

These bath operators can subsequently be used to determine the Fourier transform equilibrium bath correlation functions according to Eq. (2.42) as

$$\gamma_{\alpha\beta}(\omega) = \int_{-\infty}^{+\infty} \text{Tr} \left\{ e^{i\hat{\mathcal{H}}_B\tau} \hat{B}_\alpha e^{-i\hat{\mathcal{H}}_B\tau} \hat{B}_\beta \bar{\rho}_B \right\} e^{i\omega\tau} d\tau, \quad (3.24)$$

where $\bar{\rho}_B = \sum_{i,\alpha} \bar{\rho}_{i,\alpha}$. We find that the nonvanishing contributions assume the form of Fermi's Golden rule and read

$$\begin{aligned} \gamma_{12}(\omega) &= \Gamma_{1,L}(-\omega) f_{1,L}(-\omega), \quad \gamma_{21}(\omega) = \Gamma_{1,L}(\omega) [1 - f_{1,L}(\omega)], \\ \gamma_{34}(\omega) &= \Gamma_{1,R}(-\omega) f_{1,R}(-\omega), \quad \gamma_{43}(\omega) = \Gamma_{1,R}(\omega) [1 - f_{1,R}(\omega)], \\ \gamma_{56}(\omega) &= \Gamma_{2,L}(-\omega) f_{2,L}(-\omega), \quad \gamma_{65}(\omega) = \Gamma_{2,L}(\omega) [1 - f_{2,L}(\omega)], \\ \gamma_{78}(\omega) &= \Gamma_{2,R}(-\omega) f_{2,R}(-\omega), \quad \gamma_{87}(\omega) = \Gamma_{2,R}(\omega) [1 - f_{2,R}(\omega)]. \end{aligned} \quad (3.25)$$

Here, the abbreviation $f_{i,\alpha}(\omega)$ defined as

$$f_{i,\alpha}(\omega) = \frac{1}{e^{\beta(\omega - \mu_{i,\alpha})} + 1}, \quad (3.26)$$

is the Fermi function of each reservoir evaluated at the transition frequency ω , and

$$\Gamma_{i,\alpha}(\omega) = 2\pi \sum_k |t_{i,\alpha,k}|^2 \delta(\nu_{i,\alpha,k} - \omega), \quad (3.27)$$

are the energy dependent tunneling rates between the reservoir (i, α) and the QD (i, α) . With this results, we can now proceed to calculate the rate matrix elements from Eq. (2.48). However, to do this, we need to find the eigensystem of the system Hamiltonian which is in general difficult to obtain analytically, except for some special limits. Therefore, in order to diagonalize the full system Hamiltonian from Eq. (3.1) and calculate the expectation values over the system operators, we resort to numerical methods.

3.3 Transport characteristics

Within the following sections, we will apply the master equation formalism derived in Ch. 2 to the system Hamiltonian in Eq. (3.1) and analyze its steady-state properties both analytically and numerically. Motivated by the well known transport properties through DQD structures [41, 160–164], we especially focus on the steady-state particle currents. Here, we expect to find a so called Coulomb diamond (CD) pattern in dependence of externally applied gate- and bias potentials.

3.3.1 Full transport characteristics

In order to analyze the steady-state transport spectrum of the full Hamiltonian from Eq. (3.1), we need to evaluate Eq. (2.93). Therefore, we numerically determine the eigenspectrum of the full system Hamiltonian. This allows to calculate the rates defined in Eq. (2.48). Subsequently, we establish the corresponding Liouvillian for the populations of the reduced system density matrix. Thus, we obtain a Liouvillian of dimension 32×32 , which we insert in Eq. (2.93). Using this result, we numerically calculate the steady-state particle current through the system. Since a particle exchange between the DQDs is not possible, we find that the conservation of the total particle number yields the steady-state current relation

$$I_i^{(L)} = -I_i^{(R)} \equiv I_i, \quad (3.28)$$

for each transport DQD, respectively.

We obtain the transport spectrum by calculating the steady-state particle current for varying gate voltage $V_{\text{Gate}} = \varepsilon$, which shifts the energy levels of all transport DQDs according to Eq. (3.1), and varying external bias voltage V_{Bias} . The bias voltage enters the Liouville super operator through the Fermi functions via the chemical potentials. For convenience, we henceforth assume symmetric chemical potentials

$$\mu_{i,L} = \frac{V_{\text{Bias}}}{2} \quad \text{and} \quad \mu_{i,R} = -\frac{V_{\text{Bias}}}{2}, \quad (3.29)$$

for both transport channels in all further calculation.

To understand the idea behind transport spectroscopy, we point out that in the limit of vanishing temperatures the Fermi-Dirac distribution from Eq. (3.26) can be approximated by the Heaviside step function $\Theta(x)$ according to

$$\lim_{T \rightarrow 0} f_{i,\alpha}(\omega) = \Theta(\mu_{i,\alpha} - \omega). \quad (3.30)$$

From this observation, we see that for configurations where the two leads connected to a single DQD i have the chemical potentials $\mu_{i,R}$ and $\mu_{i,L}$, only such electrons which lie in the transport window $V_{\text{Bias}} = (\mu_{i,L} - \mu_{i,R})$ can participate in the transport. Only in this energy range there are occupied energy levels in one reservoir and empty energy levels in the other reservoir. For transition energies where the corresponding energy levels in both reservoirs are filled, no electron transport is possible due to the Pauli exclusion principle. This argument also holds for finite temperatures. However, for $T > 0$ the transport window is smeared out due to the thermal melting of the Fermi edge. Therefore, the conclusive identification of the width of the transport window with the bias voltage V_{Bias} is only approximately valid for small finite temperatures.

Additionally to a finite transport window, the transport theory described by the BMS master equation from Eq. (2.51) requires that at least a single transition frequency of the system lies within this transport window in order to observe transport through this setup. By carefully adjusting the gate- and bias voltages one can

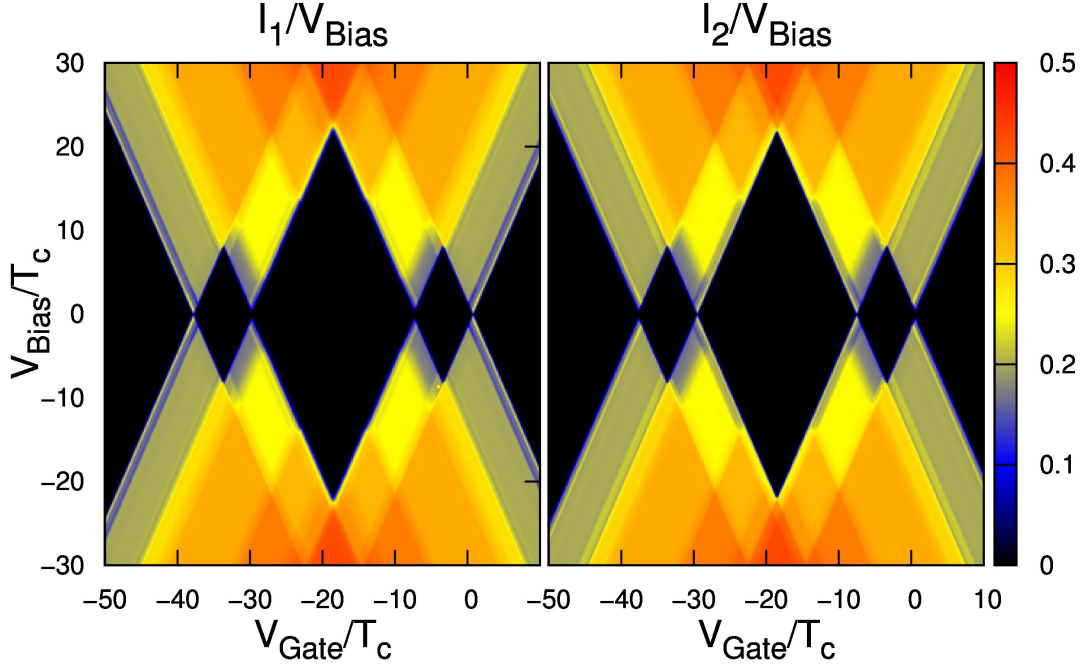


Figure 3.2: Unitless steady-state currents through channel 1 (left) and channel 2 (right). We observe Coulomb Diamond (CD) structures where the currents vanish (black). Outside of the CDs the currents increase nearly stepwise for low temperatures. The system parameters are fixed to: $\beta = 100/T_c$, $U_{\parallel} = 20 T_c$, $U_{\perp} = U_X = 10 T_c$, $J = \Omega = \Gamma_{i,\alpha} = T_c$ and $G = -T_c$.

select the transition energies of the system through which transport is possible, i.e., which lie in the transport window. Thus, plotting the steady-state currents for different values of V_{Bias} and V_{Gate} reveals information about the energy-level structure of the system. This method represents the foundation of transport spectroscopy [165–167].

For this reason, we plot the numerically calculated steady-state particle current versus the gate- and bias potential in Fig. 3.2. We observe diamond shaped regions where the particle current vanishes. This vanishing current is caused by the Coulomb repulsion between electrons in the system that prevent the entering of an additional electron [153]. Hence, one can also associate a fixed number of electrons to each of these regions which are known in the literature as Coulomb diamonds [168–170]. In order to overcome this repulsive barrier one has to increase the bias- and/or gate potentials. Thus, starting in such a Coulomb diamond and subsequently increasing or diminishing the gate- and/or the bias potential beyond a certain threshold yields a finite current. The value of these threshold and, hence, the size of the Coulomb diamonds mostly depends on the strength of the Coulomb repulsions. Further increasing the potential bias allows for even more system transition energies to enter the transport window. For the case of, e.g., a single DQD,

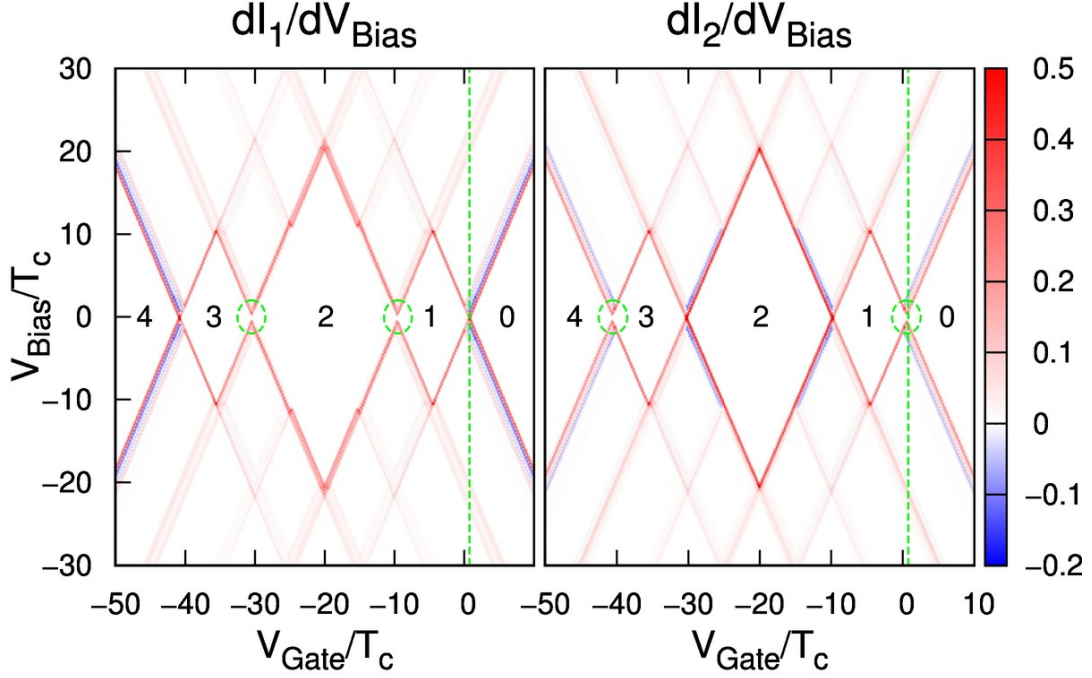


Figure 3.3: Unitless, differential steady-state currents through channel 1 (left) and channel 2 (right). Most prominent are the CD structures with a different number of electrons (inset: numbers) loaded into the system. The dashed circles indicate the presence of gaps between the CDs and the dashed vertical lines correspond to Fig. 3.4. The other parameters are fixed to: $\beta = 100/T_c$, $U_{\parallel} = 20 T_c$, $U_{\perp} = U_X = 10 T_c$, $J = \Omega = \Gamma_{i,\alpha} = T_c$ and $G = -T_c$.

this usually leads to an increased particle current through the system. For sufficiently low temperatures the increase in the current is approximately stepwise in accordance with the statement from Eq. (3.30).

In transport spectroscopy the physical quantity of interest is the energy spectrum of the system. Therefore, one prefers to investigate the differential change of the steady-state current with respect to the potentials, rather than its absolute amount. For the considered setup we show the differential transport spectra for both transport channels in Fig. 3.3. Both panels in this figure show a structure composed of two sets of parallel lines which cross each other to form a pattern of tetragons. Each line represents a system transition energy in the transport window.

In each of the two panels we see three partially closed CDs labeled 1, 2, 3 and two open CDs labeled by the numbers 0 and 4. As explained before, within these regions the respective steady-state currents vanish due to Coulomb blockade effects [171–173] that prevent electronic transport through the system. For a suitable choice of gate- and bias voltages, this blockade can be overcome leading to finite steady-state currents. Since we assume a relatively small temperature, the current changes ap-

proximately step-wise indicated by the lines outside of the CDs. The Coulomb diamonds can be associated with specific electronic subspaces reaching from the vacuum state with zero electrons in the DQDs up to the maximal number of four electrons in the DQDs. These electron subspaces are indicated by the number insets in Fig. 3.3. Note that distinct CDs can only be observed for low temperatures. As the temperature is raised the CDs become smeared out making it hard to distinguish them.

Additionally to the CD structure, we observe a multitude of additional lines corresponding to higher transitions in the system. Depending on the chosen system parameters they can be relatively close to each other which makes it difficult to resolve them. The largest differential currents dI/dV_{Bias} are observed at the edges of the Coulomb diamonds where the current changes from zero to some finite value. Moreover, we also observe that there are transitions that yield a negative differential current (blue lines), meaning the current is diminished despite the fact that the external potentials are raised. Finally, we notice that the CDs are just partially closed and that there is a certain symmetry between the two transport channels shown in the left and right panels of Fig. 3.3, respectively.

In order to gain a better physical insight and understanding of these observations, we focus on some analytically solvable limits of the system Hamiltonian in the following sections.

3.3.2 Ultra-strong Coulomb blockade regime

Since the full system Hamiltonian from Eq. (3.1) is complicated to analyze analytically, we first consider the case of a high Coulomb repulsion in the whole system, i.e., $U_{\parallel}, U_{\perp}, U_X \gg \{\varepsilon, T_c, G, \Omega\}$. Here, only the system transition energies from the zero-to-one electron subspace lie within the transport window. Hence, using this limit, we can describe the section in the vicinity of the Coulomb diamonds 0 and 1 in Fig. 3.3. We refer to this limit as the ultra-strong Coulomb blockade limit (USCB). In this limit, we can model the system by an effective Hamiltonian which reads as

$$\hat{\mathcal{H}}_{\text{USCB}} = \sum_{i=1}^2 \left(\sum_{\alpha} \varepsilon \hat{d}_{i,\alpha}^{\dagger} \hat{d}_{i,\alpha} + \left[T_c + \frac{G}{2} \{ \mathbb{1} - (-1)^i \hat{\sigma}_z \} \right] [\hat{d}_{i,L}^{\dagger} \hat{d}_{i,R} + \hat{d}_{i,R}^{\dagger} \hat{d}_{i,L}] \right) + \hat{\mathcal{H}}_{\text{CQB}}. \quad (3.31)$$

This Hamiltonian is block diagonal and consist of three blocks corresponding to the electronic subspaces. Due to this block structure it is sufficient to find the eigenspectrum of each block separately in order to construct the full eigenspectrum of the Hamiltonian from Eq. (3.31). Concerning these blocks, we see that the block with 0 electrons in the two DQDs in the CQB basis $\{|\downarrow\rangle, |\uparrow\rangle\}$ reads as

$$\hat{H}^{(0)} = \begin{pmatrix} -\frac{\Omega}{2} & J \\ J & \frac{\Omega}{2} \end{pmatrix}. \quad (3.32)$$

Additionally, the two blocks with 1 electron in the DQD i respectively, assume in the basis $\{|L\rangle_i \otimes |\downarrow\rangle, |L\rangle_i \otimes |\uparrow\rangle, |R\rangle_i \otimes |\downarrow\rangle, |R\rangle_i \otimes |\uparrow\rangle\}$ the form

$$\hat{H}_i^{(1)} = \begin{pmatrix} \varepsilon - \frac{\Omega}{2} & J & (i-1)G + T_c & 0 \\ J & \varepsilon + \frac{\Omega}{2} & 0 & (2-i)G + T_c \\ (i-1)G + T_c & 0 & \varepsilon - \frac{\Omega}{2} & J \\ 0 & (2-i)G + T_c & J & \varepsilon + \frac{\Omega}{2} \end{pmatrix}. \quad (3.33)$$

All of these blocks can be diagonalized analytically such that the eigenvalue problems

$$\hat{H}^{(0)} |\pm\rangle^{(0)} = E_{\pm}^{(0)} |\pm\rangle^{(0)}, \quad \text{and} \quad \hat{H}_i^{(1)} |\alpha, \beta\rangle_i^{(1)} = E_{i,\alpha,\beta}^{(1)} |\alpha, \beta\rangle_i^{(1)}, \quad (3.34)$$

result in the eigenvalues

$$E_{\pm}^{(0)} = \pm J \sqrt{1 + \left(\frac{\Omega}{2J}\right)^2},$$

$$E_{i,\alpha,\beta}^{(1)} = \varepsilon - \alpha(-1)^i \left(T_c + \frac{G}{2}\right) + J\beta \sqrt{1 + \left(\frac{G + \alpha\Omega}{2J}\right)^2}, \quad \alpha, \beta \in \{-1, +1\}, \quad (3.35)$$

and the corresponding non-normalized eigenvectors

$$|\pm\rangle^{(0)} = |0\rangle_1 \otimes |0\rangle_2 \otimes \left\{ \left[-\frac{\Omega}{2J} \pm \sqrt{1 + \left(\frac{\Omega}{2J}\right)^2} \right] |\downarrow\rangle + |\uparrow\rangle \right\},$$

$$|\alpha, \beta\rangle_1^{(1)} = (|R\rangle_1 + \alpha |L\rangle_1) \otimes |0\rangle_2 \otimes \left\{ \left[\beta \sqrt{1 + \left(\frac{G + \alpha\Omega}{2J}\right)^2} - \alpha \left(\frac{G + \alpha\Omega}{2J}\right) \right] |\downarrow\rangle + |\uparrow\rangle \right\},$$

$$|\alpha, \beta\rangle_2^{(1)} = |0\rangle_1 \otimes (|R\rangle_2 - \alpha |L\rangle_2) \otimes \left\{ \left[\beta \sqrt{1 + \left(\frac{G + \alpha\Omega}{2J}\right)^2} - \alpha \left(\frac{G + \alpha\Omega}{2J}\right) \right] |\downarrow\rangle + |\uparrow\rangle \right\}. \quad (3.36)$$

Here, the states $|R\rangle_i$ and $|L\rangle_i$ are the local, single electron states of the DQD i and $|\uparrow\rangle, |\downarrow\rangle$ are the eigenstates of the CQB. From the tensor product form of the above eigenstates, we see that for the considered set of parameters there is no entanglement between the transport DQDs and the impurity in the USCB regime. Furthermore, due to the ultra-strong Coulomb blockade limit, there is also no entanglement between the two DQDs themselves. Additionally, we see that in the absence of the CQB, i.e., in the limit $\{G, \Omega\} \rightarrow 0$, we obtain the corresponding results for non-interacting parallel DQDs.

With these results, we can subsequently calculate the rates in Eq. (2.48) and construct the corresponding Liouvillian. Unfortunately, without a specific choice for the system parameters, we can not write down the Liouvillian in a compact form. Therefore, we proceed by considering additional limits and restrictions within the following subsection.

3.3.2.1 High-bias currents

The matrix elements of the Liouvillian that we can construct from the eigenvectors defined in Eq. (3.36), obviously depend on the impurity parameters G, Ω and J . Furthermore, from Eq. (3.25), we see that these entries also depend on the Fermi functions of the leads. Now, for the purpose of simplifying the structure of the Liouvillian, one often applies a high-bias limit where $V_{\text{Bias}} \gg 1$ such that all system transitions lie within the transport window. For sufficiently low temperatures, this limit implies that we can approximate the Fermi functions of the leads as

$$f_{i,L}(\omega) \xrightarrow{V_{\text{Bias}} \gg 1} 1, \quad f_{i,R}(\omega) \xrightarrow{V_{\text{Bias}} \gg 1} 0. \quad (3.37)$$

Additionally, assuming the wide-band limit $\Gamma_{i,\alpha}(\omega) = \Gamma_{i,\alpha}$, we obtain a Liouvillian which is independent of the transition frequencies in the system and the occupations of the leads. Fixing the basis of the density vector according to

$$\rho = \left(\rho_+^{(0)}, \rho_-^{(0)}, \rho_{1--}^{(1)}, \rho_{1-+}^{(1)}, \rho_{1+-}^{(1)}, \rho_{1++}^{(1)}, \rho_{2--}^{(1)}, \rho_{2-+}^{(1)}, \rho_{2+-}^{(1)}, \rho_{2++}^{(1)} \right)^T, \quad (3.38)$$

where the density matrix elements $\rho_{i\alpha\beta}^{(n)}$ are labeled in correspondence with the energy eigenstates in Eq. (3.36), this Liouvillian for the USCB regime in the high-bias limit reads as

$$\mathcal{W}(0) = \begin{pmatrix} -\Gamma_{1,L} - \Gamma_{2,L} & 0 & \frac{1+\Lambda_+}{4}\Gamma_{1,R} & \frac{1+\Lambda_+}{4}\Gamma_{2,R} & \frac{1-\Lambda_+}{4}\Gamma_{1,R} & \frac{1-\Lambda_+}{4}\Gamma_{2,R} & \frac{1+\Lambda_-}{4}\Gamma_{2,R} & \frac{1+\Lambda_-}{4}\Gamma_{1,R} & \frac{1-\Lambda_-}{4}\Gamma_{2,R} & \frac{1-\Lambda_-}{4}\Gamma_{1,R} \\ 0 & -\Gamma_{1,L} - \Gamma_{2,L} & \frac{1-\Lambda_+}{4}\Gamma_{1,R} & \frac{1-\Lambda_+}{4}\Gamma_{2,R} & \frac{1+\Lambda_+}{4}\Gamma_{1,R} & \frac{1+\Lambda_+}{4}\Gamma_{2,R} & \frac{1-\Lambda_-}{4}\Gamma_{2,R} & \frac{1-\Lambda_-}{4}\Gamma_{1,R} & \frac{1+\Lambda_-}{4}\Gamma_{2,R} & \frac{1+\Lambda_-}{4}\Gamma_{1,R} \\ \frac{1+\Lambda_+}{4}\Gamma_{1,L} & \frac{1-\Lambda_+}{4}\Gamma_{1,L} & -\frac{\Gamma_{1,R}}{2} & 0 & 0 & 0 & 0 & 0 & 0 & 0 \\ \frac{1+\Lambda_+}{4}\Gamma_{2,L} & \frac{1-\Lambda_+}{4}\Gamma_{2,L} & 0 & -\frac{\Gamma_{2,R}}{2} & 0 & 0 & 0 & 0 & 0 & 0 \\ \frac{1-\Lambda_+}{4}\Gamma_{1,L} & \frac{1+\Lambda_+}{4}\Gamma_{1,L} & 0 & 0 & -\frac{\Gamma_{1,R}}{2} & 0 & 0 & 0 & 0 & 0 \\ \frac{1-\Lambda_+}{4}\Gamma_{2,L} & \frac{1+\Lambda_+}{4}\Gamma_{2,L} & 0 & 0 & 0 & -\frac{\Gamma_{2,R}}{2} & 0 & 0 & 0 & 0 \\ \frac{1+\Lambda_-}{4}\Gamma_{2,L} & \frac{1-\Lambda_-}{4}\Gamma_{2,L} & 0 & 0 & 0 & 0 & -\frac{\Gamma_{2,R}}{2} & 0 & 0 & 0 \\ \frac{1+\Lambda_-}{4}\Gamma_{1,L} & \frac{1-\Lambda_-}{4}\Gamma_{1,L} & 0 & 0 & 0 & 0 & 0 & -\frac{\Gamma_{1,R}}{2} & 0 & 0 \\ \frac{1-\Lambda_-}{4}\Gamma_{2,L} & \frac{1+\Lambda_-}{4}\Gamma_{2,L} & 0 & 0 & 0 & 0 & 0 & 0 & -\frac{\Gamma_{2,R}}{2} & 0 \\ \frac{1-\Lambda_-}{4}\Gamma_{1,L} & \frac{1+\Lambda_-}{4}\Gamma_{1,L} & 0 & 0 & 0 & 0 & 0 & 0 & 0 & -\frac{\Gamma_{1,R}}{2} \end{pmatrix}. \quad (3.39)$$

To keep our notation as compact as possible, we introduced the abbreviations

$$\Lambda_+ = \frac{1 + \frac{\Omega}{2J} \left(\frac{G+\Omega}{2J} \right)}{\sqrt{\left[1 + \left(\frac{\Omega}{2J} \right)^2 \right] \left[1 + \left(\frac{G+\Omega}{2J} \right)^2 \right]}}, \quad \Lambda_- = \frac{1 - \frac{\Omega}{2J} \left(\frac{G-\Omega}{2J} \right)}{\sqrt{\left[1 + \left(\frac{\Omega}{2J} \right)^2 \right] \left[1 + \left(\frac{G-\Omega}{2J} \right)^2 \right]}}. \quad (3.40)$$

This limit allows one to calculate the steady-state density matrix and particle current analytically. As an example we show the steady-state density matrix populations in the wide-band limit which are given by

$$\bar{\rho}_\alpha^{(0)} = \frac{1}{2\theta} \Gamma_{1,R} \Gamma_{2,R}, \quad \bar{\rho}_{1\alpha\beta}^{(1)} = \frac{1}{2\theta} \Gamma_{1,L} \Gamma_{2,R}, \quad \bar{\rho}_{2\alpha\beta}^{(1)} = \frac{1}{2\theta} \Gamma_{1,R} \Gamma_{2,L}, \quad (3.41)$$

with the normalization constant

$$\theta = 2 (\Gamma_{1,L}\Gamma_{2,R} + \Gamma_{1,R}\Gamma_{2,L}) + \Gamma_{1,R}\Gamma_{2,R}. \quad (3.42)$$

From the rates appearing in the steady-state populations, we see that the particles enter the system from the left leads and leave it through the right leads in accordance with the high-bias limit from Eq. (3.37).

In this ultra-strong Coulomb blockade regime, we make use of Eq. (2.93) and find that the high-bias steady-state current through the transport channel i becomes

$$I_{\text{USCB}}^{(i,R)} = \frac{\Gamma_{i,L}\Gamma_{i,R}\Gamma_{\bar{i},R}}{2(\Gamma_{i,R}\Gamma_{\bar{i},L} + \Gamma_{i,L}\Gamma_{\bar{i},R}) + \Gamma_{i,R}\Gamma_{\bar{i},R}}, \quad \bar{i} \in \{1, 2\} \mid i \neq \bar{i}. \quad (3.43)$$

Here \bar{i} labels the opposite transport channel.

From Eq. (3.43), we see that the current $I_{\text{USCB}}^{(i,R)}$ explicitly depends on the tunneling rates of the opposite channel. This is to be expected for a configuration with dynamical channel blockade [152, 174]. This intermediate coupling is lifted, for example, if the DQD i is almost immediately reloaded from the left lead, i.e., $\Gamma_{i,L} \gg \Gamma_{i,R}$. Then, the system tends to be always occupied by an electron: The steady-state current in channel i becomes proportional to the coupling to the right lead, i.e.,

$$I_{\text{USCB}}^{(i,R)} \xrightarrow{\Gamma_{i,L} \gg \Gamma_{i,R}} \frac{\Gamma_{i,R}}{2}, \quad (3.44)$$

whereas the current through the other transport channel vanishes. In the opposite case, when the DQD i is not refilled from the left lead, i.e., $\Gamma_{i,L} \rightarrow 0$, while the other tunneling rates remain nonvanishing, the steady-state current through channel i vanishes and the other current takes on the form of Eq. (3.56). Considering a similar configuration where the electrons almost instantly leave the transport channel i via the right lead, i.e., $\Gamma_{i,R} \gg \Gamma_{i,L}$, we find that the channel coupling is only partially lifted. In fact, in this limit, the opposite channel decouples and the respective steady-state current takes on the form of Eq. (3.56). However, the steady-state current i becomes

$$I_{\text{USCB}}^{(i,R)} \xrightarrow{\Gamma_{i,R} \gg \Gamma_{i,L}} \frac{\Gamma_{i,L}\Gamma_{\bar{i},R}}{2\Gamma_{\bar{i},L} + \Gamma_{\bar{i},R}}, \quad (3.45)$$

and, hence, is still proportional to tunnel couplings of both transport channels. Finally, if the couplings to the left leads and the couplings to the right leads are the same for both channels, i.e., $\Gamma_{i,\alpha} \rightarrow \Gamma_{\alpha}$, the steady-state currents are the same for each channel reading

$$I_{\text{USCB}}^{(R)} = \frac{\Gamma_L\Gamma_R}{4\Gamma_L + \Gamma_R}. \quad (3.46)$$

Finally, we note that due to electron-hole symmetry, one finds analogous results to Eq. (3.43) if the system transition energies from the three-to-four electron subspace lie within the transport window.

3.3.3 Strong Coulomb blockade regime

In addition to the USCB limit, we now consider a less restrictive limit where we assume that each transport DQD can at most be filled with one electron. Thus, we are considering the situation that $U_{\parallel} \gg \{\varepsilon, T_c, G, \Omega, U\}$, where we, for the sake of simplicity, assume $U = U_{\perp} = U_{\chi}$. Consequently, in this approximation the 0- and 1-electron states as well as some of the 2-electron states lie within the transport window. Hence, this limit is capable to describe the section from the CD 0 up to the beginning of the CD 2 in Fig. 3.3. In this limit, to which we refer as the strong Coulomb blockade limit (SCB), the system can be described by the effective Hamiltonian

$$\hat{\mathcal{H}}_{\text{SCB}} = \hat{\mathcal{H}}_{\text{USCB}} + U \sum_{\alpha, \beta \in \{L, R\}} \hat{d}_{1, \alpha}^{\dagger} \hat{d}_{1, \alpha} \hat{d}_{2, \beta}^{\dagger} \hat{d}_{2, \beta}. \quad (3.47)$$

This Hamiltonian is also block-diagonal, consisting of the same three blocks found in the USCB limit according to Eq. (3.32) and Eq. (3.33). Moreover, since we now also allow for a total of 2 electrons in the two DQDs, we find an additional block corresponding to the 2-electron states of the system. In the two-electron basis

$$\{|L, L, \downarrow\rangle, |L, L, \uparrow\rangle, |L, R, \downarrow\rangle, |L, R, \uparrow\rangle, |R, L, \downarrow\rangle, |R, L, \uparrow\rangle, |R, R, \downarrow\rangle, |R, R, \uparrow\rangle\}, \quad (3.48)$$

this block explicitly reads as

$$\hat{H}^{(2)} = \begin{pmatrix} \bar{U} - \frac{\Omega}{2} & J & G + T_c & 0 & T_c & 0 & 0 & 0 \\ J & \bar{U} + \frac{\Omega}{2} & 0 & T_c & 0 & G + T_c & 0 & 0 \\ G + T_c & 0 & \bar{U} - \frac{\Omega}{2} & J & 0 & 0 & T_c & 0 \\ 0 & T_c & J & \bar{U} + \frac{\Omega}{2} & 0 & 0 & 0 & G + T_c \\ T_c & 0 & 0 & 0 & \bar{U} - \frac{\Omega}{2} & J & G + T_c & 0 \\ 0 & G + T_c & 0 & 0 & J & \bar{U} + \frac{\Omega}{2} & 0 & T_c \\ 0 & 0 & T_c & 0 & G + T_c & 0 & \bar{U} - \frac{\Omega}{2} & J \\ 0 & 0 & 0 & G + T_c & 0 & T_c & J & \bar{U} + \frac{\Omega}{2} \end{pmatrix}, \quad (3.49)$$

where we used the abbreviation $\bar{U} = (U + 2\varepsilon)$. Solving the corresponding eigenvalue equation

$$\hat{H}^{(2)} |i, \alpha, \beta\rangle^{(2)} = E_{i, \alpha, \beta}^{(2)} |i, \alpha, \beta\rangle^{(2)}, \quad (3.50)$$

results in the eigenvalues

$$E_{i, \alpha, \beta}^{(2)} = \begin{cases} i = 1, & 2\varepsilon + \alpha J \sqrt{1 + \left(\frac{2G + \beta\Omega}{2J}\right)^2} \\ i = 2, & 2\varepsilon + \alpha (G + 2T_c) + \beta J \sqrt{1 + \left(\frac{\Omega}{2J}\right)^2} \end{cases}, \quad \alpha, \beta \in \{-1, +1\}, \quad (3.51)$$

with the respective non-normalized eigenstates

$$\begin{aligned} |1, \alpha, \beta\rangle^{(2)} &= (|R\rangle_1 + \beta |L\rangle_1) \otimes (|R\rangle_2 - \beta |L\rangle_2) \otimes (B_{\alpha, \beta} |\downarrow\rangle + |\uparrow\rangle), \\ |2, \alpha, \beta\rangle^{(2)} &= (|R\rangle_1 + \alpha |L\rangle_1) \otimes (|R\rangle_2 + \alpha |L\rangle_2) \otimes (\bar{B}_{\beta} |\downarrow\rangle + |\uparrow\rangle). \end{aligned} \quad (3.52)$$

The emerging coefficients are defined as

$$B_{\alpha,\beta} = \beta \left(\frac{2G - \beta\Omega}{2J} \right) - \alpha \sqrt{1 + \left(\frac{2G - \beta\Omega}{2J} \right)^2}, \quad \bar{B}_\beta = -\frac{\Omega}{2J} + \beta \sqrt{1 + \left(\frac{\beta\Omega}{2J} \right)^2}. \quad (3.53)$$

We notice that the eigenstates assume again a tensor product form indicating that the subspaces of the DQDs and the CQB are not entangled. However, contrary to the USCB limit results, here this behavior is caused by our choice of the Coulomb interactions $U_\perp = U_\times$. Assuming even a small difference between these interactions would result in partially entangled eigenstates.

Following the same procedure as in the previous section, we can now calculate the rates according to Eq. (2.48) and construct the corresponding Liouvillian. However, again we can not write down the Liouvillian in a compact form and, thus, consider the high-bias limit for this Liouvillian within the following subsection.

3.3.3.1 High-bias currents

Applying the high-bias limit from Eq. (3.37) and assuming energy independent tunneling rates $\Gamma_{i,\alpha}$, we can analytically determine the steady-state system populations in the SCB limit, which read

$$\bar{\rho}_\alpha^{(0)} = \frac{1}{2\bar{\theta}} \Gamma_{1,R} \Gamma_{2,R}, \quad \bar{\rho}_{1\alpha\beta}^{(1)} = \frac{1}{2\bar{\theta}} \Gamma_{1,L} \Gamma_{2,R}, \quad \bar{\rho}_{2\alpha\beta}^{(1)} = \frac{1}{2\bar{\theta}} \Gamma_{1,R} \Gamma_{2,L}, \quad \bar{\rho}_{i\alpha\beta}^{(2)} = \frac{1}{2\bar{\theta}} \Gamma_{1,L} \Gamma_{2,L}, \quad (3.54)$$

where the normalization constant is defined as

$$\bar{\theta} = 4\Gamma_{1,L}\Gamma_{2,L} + 2(\Gamma_{1,L}\Gamma_{2,R} + \Gamma_{1,R}\Gamma_{2,L}) + \Gamma_{1,R}\Gamma_{2,R}. \quad (3.55)$$

Inserting these results into Eq. (2.93), we find that in the high-bias limit, where all transition energies from the zero-to-one and one-to-two electron subspace lie within the transport window, the SCB steady-state current through the transport channel i is of the form

$$I_{\text{SCB}}^{(i,R)} = \frac{\Gamma_{i,L}\Gamma_{i,R}}{2\Gamma_{i,L} + \Gamma_{i,R}}. \quad (3.56)$$

This result corresponds to the high-bias steady-state current one obtains for sequential electronic transport through a two-level system in the SCB regime [128].

Both results presented in Eq. (3.46) and Eq. (3.56) demonstrate that in the high-bias regime, the steady-state currents are not sensitive to the asymmetry induced by the CQB.

3.3.4 Current anti-correlation

In this section, we further analyze the transport properties of the system in the USCB regime for small bias voltages. Thus, we focus on the region in the vicinity of the

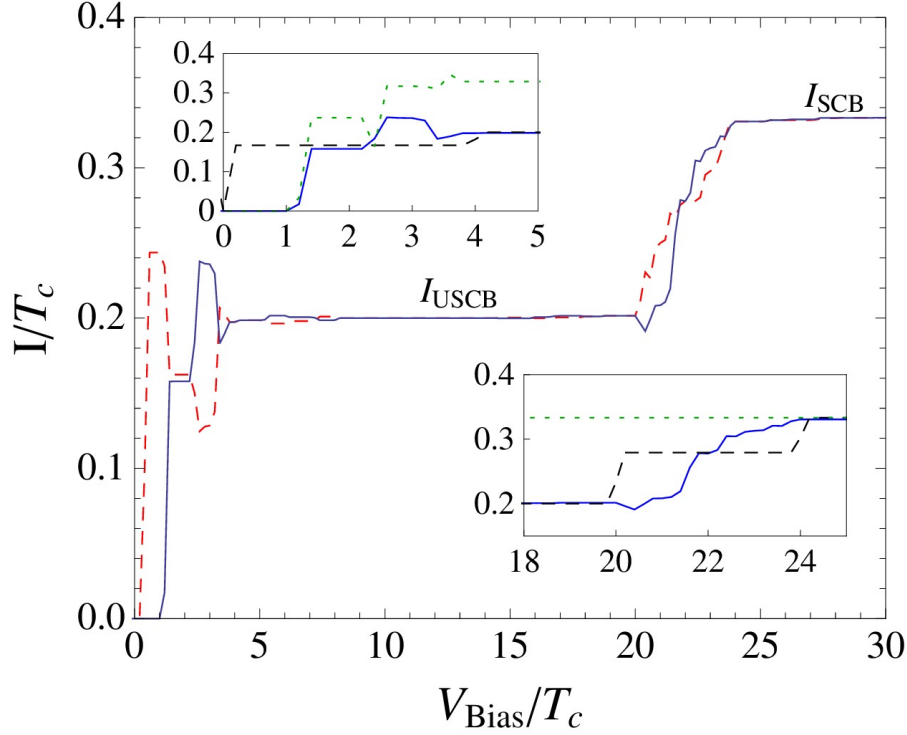


Figure 3.4: Plot of the steady-state currents for both transport channels 1 (red, dashed line) and 2 (solid line). The plot corresponds to the dashed vertical line in Fig. 3.3 at $V_{\text{Gate}} = 0.8 T_c$. We indicated the high-bias currents in the ultra-strong Coulomb blockade (I_{USCB}), and strong Coulomb blockade (I_{SCB}) regimes. The insets compare the steady-state current of channel 2 (solid line) with the results for parallel DQDs without impurity (black, dashed line) and a single DQD coupled to a CQB (dotted line). The system parameters are fixed to: $\beta = 100/T_c$, $U_{\parallel} = 20 T_c$, $U_{\perp} = U_{\times} = 10 T_c$, $J = \Omega = \Gamma_{i,\alpha} = T_c$ and $G = -T_c$.

edge of the 0-electron CD of the transport spectra in Fig. 3.3. A first interesting feature in this region is the occurrence of negative differential conductance, i.e., the blue lines in Fig. 3.3, which indicates blocking effects in the transport channels. To clearly show this effect, we plot in Fig. 3.4 the IV -curves which correspond to the green, dashed lines in Fig. 3.3. Due to the symmetry of the particle current with respect to the bias voltage, it suffices to investigate, e.g., the positive voltage regime $V_{\text{Bias}} \geq 0$ in Fig. 3.4. In this plot, we observe a negative differential conductance in both channels for certain bias voltages.

We demonstrate in the inset in Fig. 3.4 that this is an intrinsic feature resulting from the CQB impurity as negative differential conductance is not present in parallel DQDs without impurity. Consequently, we also observe a negative differential conductance for low bias voltages in a system where the second DQD is removed

(inset: dotted line). Effectively, the asymmetry induced by the impurity leads to the fact that the two possible transport channels become accessible at different gate voltages. Consequently, in which channel this negative differential current occurs depends on the sign of the CQB detuning Ω .

Furthermore, since the total number of electrons in the system is constrained by Coulomb interactions, as soon as the second transport channel becomes available, the current in the first channel decreases, leading to a negative differential conductance. Consistently, this property is most prominent in the Coulomb blockade regime. Therefore, by comparing the steady-state currents for the two transport channels, we find that this feature is accompanied by an anti-correlation between the steady-state currents in the different transport channels. This anti-correlation can be clearly observed in Fig. 3.4 for a small bias voltage in the range $0 < V_{\text{Bias}} < 5$.

3.3.5 Coulomb diamond gaps

The most striking feature of the plots in Fig. 3.3 is the fact that some of the observed Coulomb diamonds do not close, as indicated by the dashed circles. We expect this effect to occur for coupled DQDs with asymmetries in the quantum-dot energies or in their tunneling amplitudes [175–177]. Because we explicitly exclude this kind of asymmetry in the transport DQDs, this effect clearly suggests a blocking induced by a finite energy barrier at zero bias voltage that stems from the presence of the CQB. Consistently, we find that it depends on the sign of the detuning Ω in which channel the gap appears.

Since all changes in the steady-state currents are associated to transition energies between eigenstates of the system Hamiltonian, it is possible to calculate the position of the lines shown in Fig. 3.4 if the eigenvalues of the respective Hamiltonian $\hat{\mathcal{H}}_S$ are known. Hence, a diagonalization of Eq. (3.1) allows one to calculate the position and width of the gap. Since the system Hamiltonian is block-diagonal, as discussed in Sec. 3.1, one can diagonalize each block separately to obtain the full eigenspectrum of the system. As a consequence, we can use the results for the eigenvalues and eigenstates calculated in the USCB and SCB limits in Sec. 3.3.2 and Sec. 3.3.3. Therefore, by identifying the involved transition energies using the eigenvalues from Eq. (3.35), we can analyze the gap between the 0- and 1-electron Coulomb diamond in the second transport channel. By comparison we find that the transitions energies responsible for this gap are given by

$$\omega_{\pm}^{(1)} = \pm \left(E_{-}^{(0)} - E_{2,+,-}^{(1)} \right), \quad \omega_{\pm}^{(2)} = \pm \left(E_{-}^{(0)} - E_{2,-,-}^{(1)} \right). \quad (3.57)$$

These are the transitions from the energetically lowest vacuum state $|-\rangle^{(0)}$ to the 1-electron states $|-, -\rangle_2^{(1)}$ and $|+, -\rangle_2^{(1)}$. All properties of the CD gap can subsequently be determined from these transition energies. For example the gate voltage for which

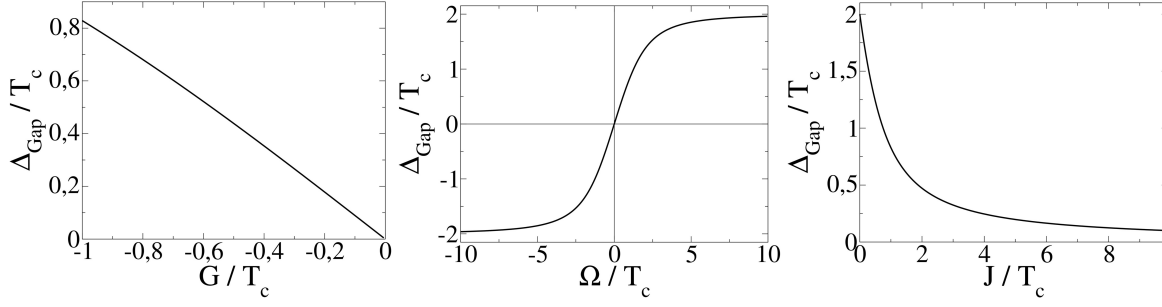


Figure 3.5: Plot of the width of the gap between the 0- and 1-electron Coulomb diamond in dependence of the parameters of the charge-qubit. All the remaining parameters are set equal to T_c except for G which is set to $-T_c$. Note that the negative gap width for a negative detuning indicates that the gap appears in the opposite channel.

the gap between the 0-electron and 1-electron CD is minimal, is given by

$$V_{\text{Gate}}^{\min} = J \left\{ \frac{G + 2T_c}{2J} + \frac{1}{2} \left[\sqrt{1 + \left(\frac{G - \Omega}{2J} \right)^2} + \sqrt{1 + \left(\frac{G + \Omega}{2J} \right)^2} \right] - \sqrt{1 + \left(\frac{\Omega}{2J} \right)^2} \right\}. \quad (3.58)$$

Subsequently, we derive the other parameters of the gap such as the upper bias voltage at this point, which reads as

$$V_{\text{Bias}}^{\text{upper}} = J \left[\sqrt{1 + \left(\frac{G - \Omega}{2J} \right)^2} - \sqrt{1 + \left(\frac{G + \Omega}{2J} \right)^2} \right]. \quad (3.59)$$

Due to the choice of our parameters, the gap is symmetric with respect to $V_{\text{Bias}} = 0$ and thus the lower bias voltage satisfies $V_{\text{Bias}}^{\text{lower}} = -V_{\text{Bias}}^{\text{upper}}$. Hence, the width of the gap is given by

$$\Delta_{\text{Gap}} = 2J \left[\sqrt{1 + \left(\frac{G - \Omega}{2J} \right)^2} - \sqrt{1 + \left(\frac{G + \Omega}{2J} \right)^2} \right] = 2V_{\text{Bias}}^{\text{upper}}. \quad (3.60)$$

In an analogous way, we can determine the point of contact of these Coulomb diamonds in the opposite channel. We find that this position is given by the relation

$$V_{\text{Gate}}^{\text{cross}} = J \left[\frac{G + 2T_c}{2J} + \sqrt{1 + \left(\frac{G - \Omega}{2J} \right)^2} - \sqrt{1 + \left(\frac{\Omega}{2J} \right)^2} \right] = V_{\text{Gate}}^{\min} + \frac{1}{2} V_{\text{Bias}}^{\text{upper}}. \quad (3.61)$$

From Eq. (3.60) and the results in Fig. 3.5, we see that for the considered experimental setup, the appearance of the gap results solely from the CQB since it depends on both, the detuning Ω and the modification G of the intrinsic tunnel amplitudes. If

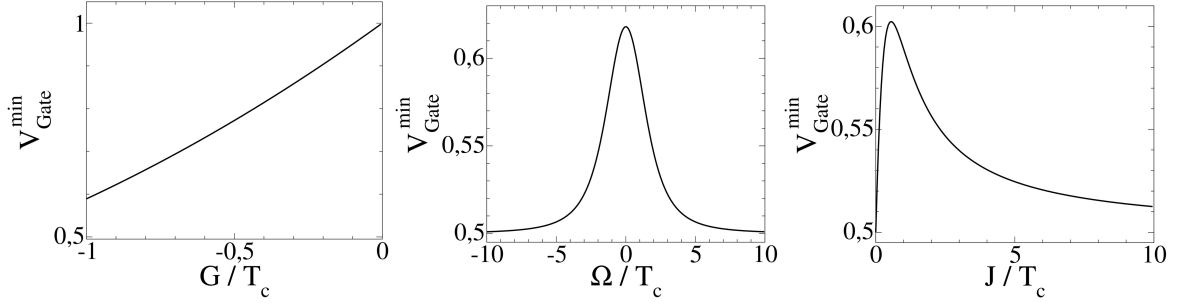


Figure 3.6: Plot of the position of the minimum gap between the 0- and 1-electron Coulomb diamond in dependence of the parameters of the charge-qubit. All the remaining constants are set equal to T_c except for G which is set to $-T_c$.

one of these quantities is zero, the gap vanishes. On the contrary, the width of the gap is completely independent of the intrinsic tunnel amplitudes T_c of the transport DQDs. Moreover, we find that the gap not only vanishes as G or Ω approaches zero, but also if J becomes very large. This behavior can be understood since the rapidly oscillating CQB on average affects both transport channels in the same way and the energy barrier vanishes.

Investigating the position of the gap according to Eq. (3.58) yields a more complicated behavior in dependence of the CQB parameters as shown in Fig. 3.6. For example, we find that, as the hopping amplitude J is increased from zero, the gap is shifted from an initial finite value to higher gate voltages up to a maximal value. A further increase of J results in a shift of the minimum gap to lower gate voltages, which in the limit $J \rightarrow \infty$ becomes a constant that equals the position for $J = 0$. Likewise the gap position is maximally shifted for a small detuning and approaches the value $1/2T_c$ for large detuning Ω . Therefore, we conclude that the system is most sensitive to the CQB for a small tunneling amplitude J and detuning Ω .

In general, we note that measuring the quantities described by Eqs. (3.58)–(3.61) in a real experiment enables one to calculate the tunneling amplitude J and the detuning Ω of the CQB as well as the modification G of the tunnel amplitudes T_c of the DQDs.

3.4 Preparation of pure states

After we analyzed the transport properties of the steady-state currents within the previous section, we now shift our focus and treat the CQB not as an unwanted impurity but as a crucial part of the system of interest.

Here, we first notice that the SCB limit includes configurations where the transport DQDs can also be treated as CQBs, giving rise to an effective system composed of three coupled CQBs. In the following, we refer to this specific subspace as the

strong Coulomb blockade qubit (SCB-QB) limit which corresponds to the SCB limit from Sec. 3.3.3, where additionally the vacuum- and 1-electron states are eliminated. These coupled qubits represent possible candidates for basic constituents of quantum information technologies that use entangled qubit states for calculations or communication. Since by measuring a system state its entanglement is usually destroyed, one can think of it as a kind of resource: By carefully preparing the system state one can generate entanglement, which is afterwards used for the desired operation, and finally gets exhausted by the measurement [178].

Encouraged by this specific application, we study the possibility to prepare the system in a pure state and use it as an entanglement resource within the following sections. In order to better understand the eigenstates of the considered system in the long-time limit, we start by analyzing the purity of its reduced steady-state system density matrix and investigate some of the system expectation values.

3.4.1 Purity of the full system

In order to decide whether a given system state ρ is a pure eigenstate of the system or rather a mixture of several such pure states one needs to calculate the trace

$$\mathcal{P} = \text{Tr} \{ \rho^2 \} \leq 1, \quad (3.62)$$

where the equality only holds if ρ is a pure state. Note that the purity of a state can be related to its linear entropy S_L , defined via $S_L = 1 - \mathcal{P}$, which is a lower approximation for the von-Neumann entropy [179].

In Fig. 3.7, we plot the purity \mathcal{P} of the reduced system density matrix for fixed system parameters versus the gate- and bias voltages. We find that in the interior of the Coulomb diamonds and for low temperatures, the system enters a pure energy eigenstate with the lowest possible energy. This behavior causes the vanishing steady-state currents in this region.

In general, these eigenstates, which are obtained from a diagonalization of the system Hamiltonian in Eq. (3.1), are entangled states. However, for the special choice of Coulomb interactions $U_\perp = U_X$, we find that the eigenstates become separable and, thus, are not entangled [180]. Therefore, the eigenstates S_i of the system in the CDs in Fig. 3.7 have a tensor product representation that reads as

$$\begin{aligned} S_0 &= |0\rangle_1 \otimes |0\rangle_2 \otimes (a_0 |\downarrow\rangle - b_0 |\uparrow\rangle), \\ S_1 &= (|L\rangle_1 - |R\rangle_2) \otimes |0\rangle_2 \otimes (a_1 |\downarrow\rangle - b_1 |\downarrow\rangle), \\ S_2 &= (|L\rangle_1 - |R\rangle_1) \otimes (|L\rangle_2 - |R\rangle_2) \otimes (a_2 |\uparrow\rangle - b_2 |\downarrow\rangle), \\ S_3 &= |LR\rangle_1 \otimes (|L\rangle_2 - |R\rangle_2) \otimes (a_3 |\downarrow\rangle - b_3 |\uparrow\rangle), \\ S_4 &= |LR\rangle_1 \otimes |LR\rangle_2 \otimes (a_4 |\downarrow\rangle - b_4 |\uparrow\rangle), \end{aligned} \quad (3.63)$$

where $\{a_i, b_i\} \in \mathbb{R}$ are the respective normalization coefficients. We note that the purity plotted in Fig. 3.7 looks qualitatively the same, if we consider the cases where

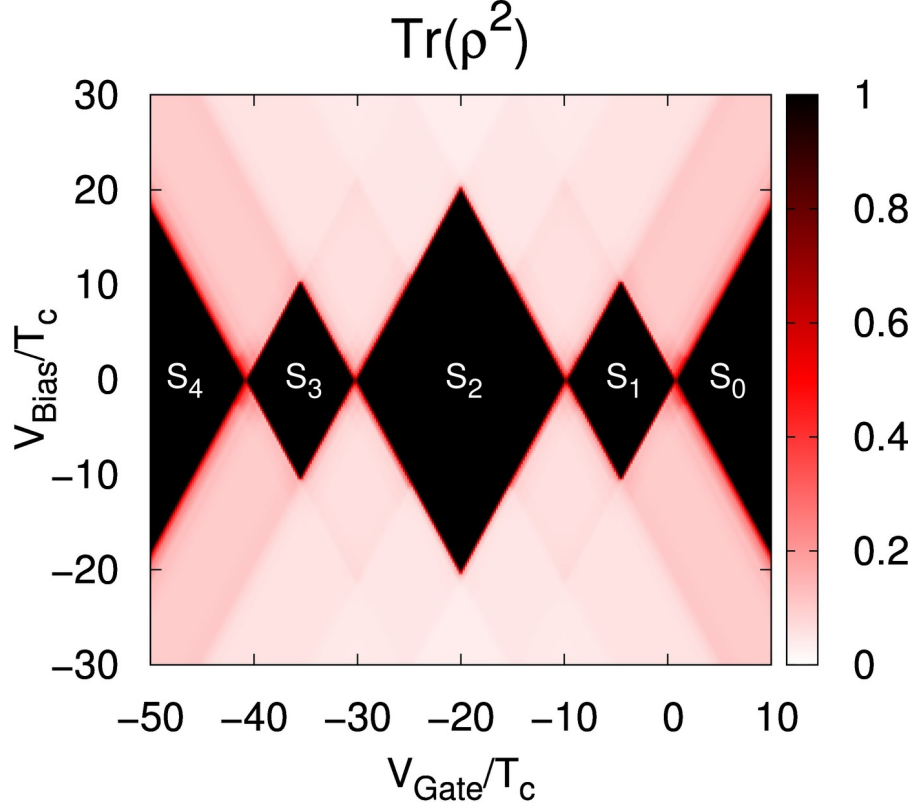


Figure 3.7: Density plot of the purity of the steady-state density matrix for low temperatures $\beta = 100/T_c$. Here, white indicates a total mixture of states, whereas black corresponds to a pure system state. The picture also shows the respective normalized eigenvectors of $\hat{\mathcal{H}}_S$ indicated in the CDs by the labels S_0, S_1, S_2, S_3 , and S_4 , which are given in Eq. (3.63). The system parameters are fixed to $U_{\parallel} = 20 T_c$, $U_{\perp} = U_X = 10 T_c$, $J = \Omega = \Gamma_{i,\alpha} = T_c$ and $G = -T_c$.

$U_{\perp} \neq U_X$. Therefore, in general the preparation of the system in an entangled pure state is possible.

If the temperature is raised, the region within a Coulomb diamond where purity is reached shrinks in favor of a mixture of states with the same number of electrons. Outside of the Coulomb diamonds, eigenstates belonging to different electron subspaces always mix together. This is not surprising since a mixture of several states is necessary to have electronic transport and a finite current. Thus, the Coulomb diamonds are in general the only regions where the preparation of a pure system state is possible.

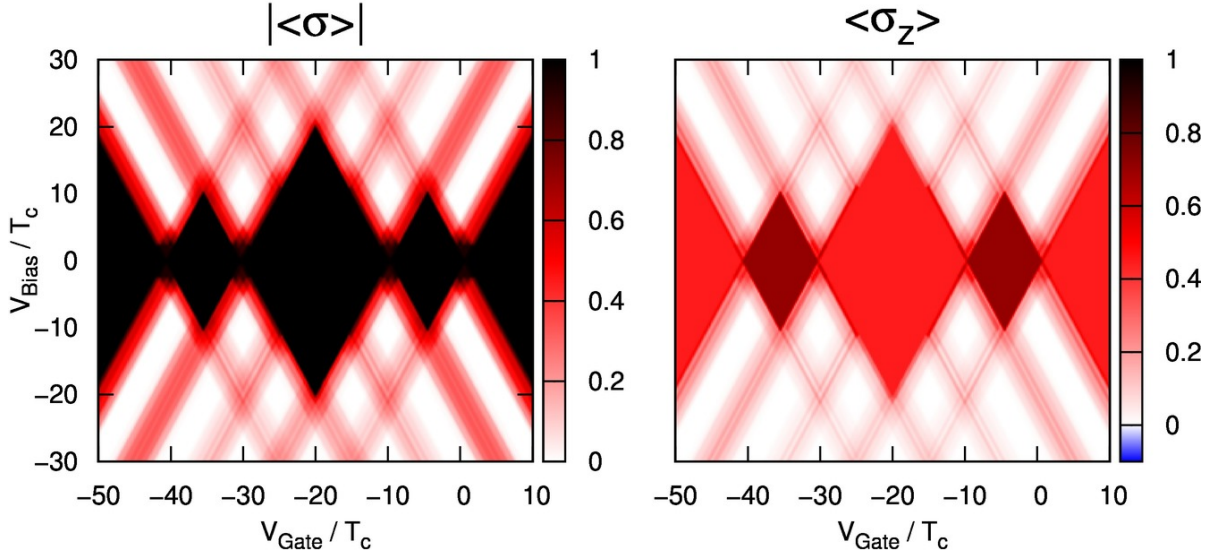


Figure 3.8: State analysis of the charge qubit for low temperatures $\beta = 100/T_c$. The left picture shows the modulus of the Bloch vector and the right picture shows the σ_z component of the CQB. The system parameters are fixed to $U_{\parallel} = 20 T_c$, $U_{\perp} = U_{\chi} = 10 T_c$, $\Gamma_{i,\alpha} = J = \Omega = T_c$ and $G = -T_c$.

3.4.2 Purity of the charge-qubit

The observation that one can prepare pure states of the whole system within the CDs, leads to the question if the same is true for the CQB. A pure density matrix of the whole system together with a mixed CQB density matrix would imply entanglement between the transport DQDs and the CQB. In order to answer this question, we calculate the stationary expectation values of the CQB occupation operators according to

$$\langle \hat{\sigma}_j \rangle = \text{Tr} \{ \hat{\sigma}_j \bar{\rho} \}. \quad (3.64)$$

Since the CQB represents a two-level system, these expectation values can be interpreted as the components of a Bloch vector. A pure CQB state corresponds to a Bloch vector with modulus one, i.e., the state lies on the surface of the Bloch sphere. Because in the steady-state the CQB component $\hat{\sigma}_y$ vanishes, the modulus of the Bloch vector is defined by

$$\| \langle \hat{\sigma} \rangle \| = \sqrt{\langle \hat{\sigma}_x \rangle^2 + \langle \hat{\sigma}_z \rangle^2}. \quad (3.65)$$

In the left panel of Fig. 3.8, we plot this quantity for fixed system parameters and the assumption that $U_{\chi} = U_{\perp}$, versus the gate- and bias voltages. We find that it is possible to tune the CQB to a pure qubit state for suitable combinations of gate- and bias voltage. The regions with large CQB purity coincide with the Coulomb diamonds, which indicates that the CQB is not entangled with the rest of the system.

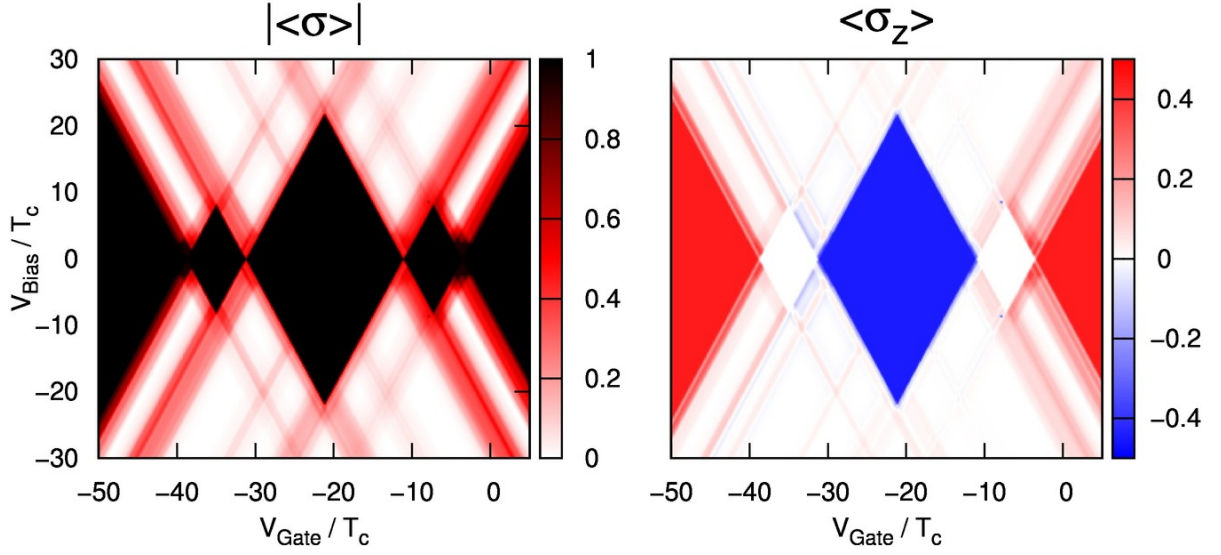


Figure 3.9: State analysis of the charge qubit for low temperatures $\beta = 100/T_c$. The left picture shows the modulus of the Bloch vector and the right picture shows its σ_z -component. The system parameters are fixed to $U_{\parallel} = 20 T_c$, $U_{\perp} = 10 T_c$, $U_{\chi} = 0.7 U_{\perp}$, $\Gamma_{i,\alpha} = J = \Omega = T_c$ and $G = -T_c$.

Furthermore, there are regions outside of the Coulomb diamonds where the electron is completely delocalized in the CQB, indicated by the vanishing modulus of the Bloch vector. However, as shown in the right panel of Fig. 3.8 the eigenstates that the CQB can take on within the Coulomb diamonds, do not correspond to localized electron states as the $\hat{\sigma}_z$ -component never takes on the value ± 1 in these regions. Nevertheless, we observe that there are regions where the $\hat{\sigma}_z$ -component of the CQB is strongly enhanced indicating a polarization. These regions coincide with the odd electron number Coulomb diamonds. This behavior indicates a back action of the electronic occupation in the DQDs on the CQB. Consistently, the $\hat{\sigma}_z$ -component of the CQB is completely undetermined in most of the regions outside of the CDs due to the electron transport through the DQDs. These properties remain qualitatively unchanged if other system parameters are considered. However, the purity and localization can be increased when lower temperatures are considered.

For comparison, we also consider a situation where the Coulomb interactions U_{χ} and U_{\perp} differ and, thus, the corresponding eigenstates are in general entangled. The results are shown in Fig. 3.9. Here, we observe that outside of the CDs the purity of the CQB is partially decreased. However, within the Coulomb diamond regions the purity of the CQB is still preserved. Therefore, we find that there is no entanglement between the CQB and the DQDs even for $U_{\perp} \neq U_{\chi}$. For the expectation value of the σ_z -component of the CQB, the difference we observe between the two cases in Fig. 3.8 and Fig. 3.9 is more striking. In fact, we see that for $U_{\chi} \neq U_{\perp}$ the σ_z -component

can assume negative values, which we do not observe for equal interactions. This effect is most obvious in the 2-electron CD where now the CQB-electron is mainly trapped in the opposite channel compared to Fig. 3.8. Additionally, the increased expectation value of the σ_z -component in the odd CDs of Fig. 3.8 is completely reduced in Fig. 3.9. This comparison shows that there is indeed a strong back action of the DQDs on the CQB

Finally, we note that in general the purity properties of the CQB as well as of the DQDs, are sensitive to thermal fluctuations and thus the stability of the corresponding regions will decrease as the temperature increases. This effect is strongest for the 2-electron CD and weakest for the 4-electron and 0-electron CDs.

3.5 Entanglement

In contrast to the separable eigenstates in Eq. (3.63), we can also change the Hamiltonian parameters to stabilize entangled states in the 2-electron CD. Thus, motivated by investigations of the entanglement of a system of parallel DQDs without the CQB impurity [51, 181], we explore the effect of the presence of the CQB on the entanglement of the transport channels within the following section.

In order to qualitatively and quantitatively determine the entanglement between the two transport DQDs, we project the steady-state density matrix onto the two-qubit subspace where exactly one electron is present in each transport DQD. Subsequently, tracing out the CQB degrees of freedom yields an effective 4×4 matrix

$$\rho_2 = \text{Tr}_{\text{rest}} \{ \rho \} \quad (3.66)$$

for the two coupled qubits represented by the transport DQDs. Here, the trace over “rest” includes the 0-, 1-, 3-, and 4-electron subspaces as well as the 2-electron states corresponding to a doubly occupied transport DQD. For this effective system of two coupled qubits, there exist a few well-defined entanglement measures [179]. One of these measures, which is known as the *concurrence* [182], is defined as

$$C = \max \left[0, \sqrt{\lambda_1} - \sqrt{\lambda_2} - \sqrt{\lambda_3} - \sqrt{\lambda_4} \right] \quad (3.67)$$

where λ_i are the eigenvalues of the matrix

$$\tilde{\rho} = \rho_2 (\sigma_y \otimes \sigma_y) \rho_2^T (\sigma_y \otimes \sigma_y) \quad (3.68)$$

arranged in decreasing order, i. e. , $\lambda_{i+1} < \lambda_i$. Testing the above definition on the Bell states [183]

$$|\Psi_{\pm}\rangle = \frac{1}{\sqrt{2}} (|\downarrow\uparrow\rangle \pm |\uparrow\downarrow\rangle), \quad |\Phi_{\pm}\rangle = \frac{1}{\sqrt{2}} (|\downarrow\downarrow\rangle \pm |\uparrow\uparrow\rangle), \quad (3.69)$$

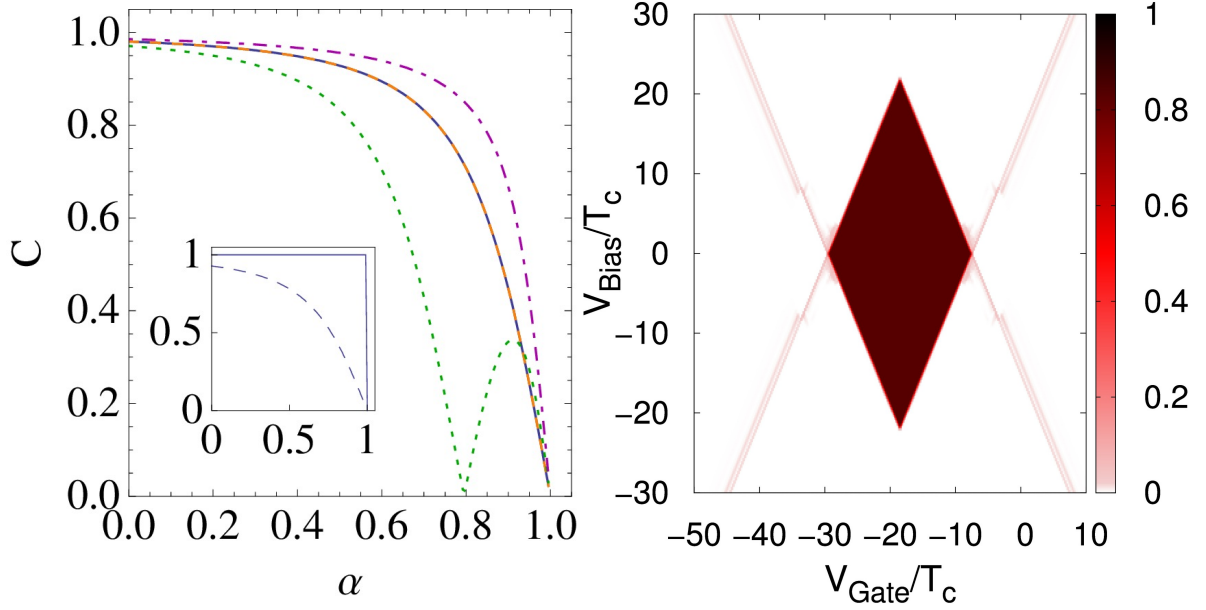


Figure 3.10: The left picture shows the concurrence of the four energy eigenstates in the qubit sector of Hamiltonian (3.1) as a function of the ratio α of the Coulomb interaction strengths. For comparison the inset shows the concurrence for the system without CQB impurity. The right plot shows the generalized transport concurrence with $\alpha = 0.7$ for the full transport spectrum. All other parameters are set to $\beta = 100/T_c$, $U_{\parallel} = 20T_c$, $U_{\perp} = 10T_c$, $\Gamma_{i,\alpha} = J = \Omega = T_c$ and $G = -T_c$.

which are maximally entangled, we notice that the spin flip facilitated by σ_y does not change the considered Bell state except for an overall sign. Therefore, the corresponding matrix $\tilde{\rho}$ has only a single nonvanishing eigenvalue $\lambda = 1$ and the concurrence assumes its maximum value $C = 1$. Contrary, applying the spin flip to a state of the local basis $\{|\downarrow\uparrow\rangle, |\uparrow\downarrow\rangle, |\downarrow\downarrow\rangle, |\uparrow\uparrow\rangle\}$ yields a different local basis state and hence the matrix $\tilde{\rho}$ has no finite eigenvalue. Hence, we see that the concurrence equals 1 for maximally entangled states and 0 for completely unentangled states.

In the following, we use the concurrence defined in Eq. (3.67) to characterize the amount of entanglement stored in the system.

3.5.1 Eigenstate concurrence

For the system of two coupled transport DQDs it is known that the strength of entanglement depends on the strength of the on-site Coulomb interaction [51]. Additionally, the entanglement of two parallel DQDs can also be influenced by asymmetric interactions or external driving [184]. Hence, this property depends on the choice of Coulomb interactions between the quantum dots. In our numerical evaluation

in Fig. 3.3, we explicitly assume that the Coulomb interaction between parallel dots has the same strength as the diagonal interactions, i. e. , $U_X = U_\perp$. However, with this choice entanglement can hardly be achieved.

In order to investigate the dependence of the entanglement of the pure states on the interaction strength, we introduce the ratio

$$\alpha \equiv \frac{U_X}{U_\perp}, \quad (3.70)$$

between parallel and diagonal Coulomb interaction in the system Hamiltonian from Eq. (3.1). First, we investigate the concurrence of the pure qubit eigenstates in the SCB-QB limit in dependence of this ratio α . In this limit, we obtain an effective system composed of three coupled CQBs. Tracing out the CQB impurity in the middle results in an effective 4×4 matrix for the remaining two coupled DQDs. The corresponding 4 eigenstates and their entanglement now depend on the ratio α and on the CQB parameters. The results for their respective concurrence are presented in the left panel in Fig. 3.10.

In general, we find that for the highly asymmetric case of $\alpha = 0$ the concurrence for parallel DQDs with CQB impurity is maximal and reaches almost 1. With increasing ratio α the concurrence decreases until it completely vanishes at $\alpha = 1$, the point of maximum symmetry. Furthermore, we see that two eigenstates show exactly the same concurrence (dashed line) in dependence on the ratio α . Contrary, one of the remaining two eigenstates possesses an increased concurrence (dot-dashed line) and the concurrence of the other one is mostly lowest (dotted line). Additionally, the concurrence of this last eigenstate vanishes at $\alpha \approx 0.8$ in contrast to all other eigenstates.

In order to clearly elaborate the effect of the CQB impurity on the concurrence, we added an analysis for two coupled qubits without CQB impurity in the inset. Here, always two of the four eigenstates show the same entanglement in dependence of α due to the symmetry of the setup. We specially observe that the two Bell states $|\Psi_-\rangle$ and $|\Phi_-\rangle$ from Eq. (3.69) corresponding to the solid line in the inset in Fig. 3.10, have a constant concurrence of 1 over almost the full range of α . Hence, these eigenstates are maximally entangled states except near the point $\alpha = 1$ where the concurrence vanishes discontinuously.

Comparing with the concurrence for the different qubit eigenstates, we find that the Bell states are destroyed due to the influence of the tunneling amplitude J and the detuning Ω of the CQB. This result is in agreement with recent theoretical work using a configuration interaction method to analyze impurity effects on quantum bits [55]. In addition, we observe that in general the concurrence of non-Bell states is raised for all values of α . This effect mainly results from the modification parameter G . The concurrence is maximally enhanced for $G = -T_c$ and approaches the value of the unperturbed system as G approaches zero.

3.5.2 Generalized transport concurrence

Lastly, we investigate the concurrence for the whole transport spectrum, which includes mixed states as well. This fact contradicts the definition of the concurrence which is basically only valid in the SCB-QB limit where the two DQDs can be treated as CQBs. In order to study entanglement in the whole transport spectrum, we therefore need to define a generalized transport entanglement measure first.

From the definition of the concurrence, it is obvious that this quantity is linear in the norm of the reduced density matrix ρ_2 . Hence, if the reduced density matrix is not renormalized after tracing out the CQB, the concurrence is only exact if evaluated in the transport qubit sector where a single electron is in each transport DQD. Otherwise, the calculation yields a product of the exact concurrence multiplied by the probability for being in a transport qubit state. Due to this special property, we will in the following use the non-renormalized concurrence C as a generalized transport concurrence to characterize the entanglement of the DQDs in the full gate and bias regimes.

In the right picture of Fig. 3.10, we plot the resulting concurrence versus gate and bias voltage. Since both cases with $\alpha = 0$ and 1 are experimentally hard to achieve and also represent rather special configurations, we choose $\alpha = 0.7$ for numerical investigations. We observe that the presence of the CQB diminishes the concurrence within the 2-electron Coulomb diamond and slightly decreases the concurrence of the mixed states outside of this Coulomb diamond. Moreover, we see that in the exterior of the 2-electron Coulomb diamond, the concurrence vanishes almost everywhere except for the regions associated with transitions from the 1- or 3-electron to the 2-electron subspace. Here, the transport qubit eigenstates enter the steady-state reduced density matrix contributing their high concurrence to the mixture of states. However, since we do not re-normalize the effective two-qubit density matrix, this high concurrence gets multiplied by the 2-electron fraction of the mixed state which corresponds to the probability to be in such a 2-particle state. Going deeper into the 2-electron subspace allows for more 2-electron eigenstates to mix in the steady state reduced density matrix and hence rapidly reduces the respective entanglement. In an experiment the DQD entanglement could be measured for example via construction of a Bell inequality as suggested in Ref. [51] or by qubit spectroscopy and quantum state tomography [185].

Chapter 4

Transport with ultracold atoms

Within this chapter we extend the research outlined in Ref. [186].

After studying electronic transport through nano-structures during the first half of this thesis, we now aspired to combine the methods presented in Chap. 2 with the field of ultra cold gases. This field of physics has attracted an ever increasing interest of both theorists and experimentalist over the recent years. In particular, the fact that these systems can nowadays be produced routinely in the lab and allow for a very high degree of control over the experimental parameters, makes them an interesting subject to study. Furthermore, some of these systems show a critical behavior, as for example the phase transition to a Bose-Einstein condensate or a quantum phase transition in lattice systems like the Bose-Hubbard model [73] and the Jaynes-Cummings-Hubbard model[31, 187]. Usually, such systems and their critical behavior are studied in equilibrium. Hence, there is not much known about their properties in nonequilibrium situations.

Therefore, we posed ourself the question if one can use transport experiments to observe signatures of the critical behavior in the transport properties such as the currents and its matter and heat conductances. Since the critical phenomena such as quantum phase transitions are only possible in very large systems it is commendable to treat the critical system-of-interest as a reservoir which is coupled to a much smaller quantum system. Finally, motivated by some recent experiments conducted in the group of Tilman Esslinger in Zürich which can be regarded as the first transport experiments with ultracold gases [104, 105], we focused on modeling the transport with ultracold quantum gases. Here, the bosonic gas is especially interesting since it shows a transition to a Bose-Einstein condensate for sufficiently low temperatures or high particle densities.

However, in order to correctly consider the experimental implementation of such transport setups and also to correctly describe the critical behavior of the quantum gas, one has to assume a constant mean particle density. In the framework of the grand-canonical ensemble theory, this assumption leads to a chemical potential that depends on the temperature and the particle density of the gas. This is in contrast to the usual scheme of a constant chemical potential used to describe electronic transport through nano-structures as for example discussed in the previous chapter.

Therefore, we start by calculating the density and temperature dependent grand-canonical chemical potential in Sec. 4.1. Subsequently, we apply this result first to a transport setup with fermionic reservoirs in Sec. 4.2, in order to analyze the modifications in comparison to the conventional approach with constant chemical potential. Afterwards, we apply it to a bosonic setup and explore the transport properties for signatures of Bose-Einstein condensation in Sec. 4.3.

4.1 Ideal quantum gases at constant density

We model the reservoirs, which are connected to the system-of-interest, as ideal quantum gases. To correctly describe the properties of these reservoirs, we review the thermodynamics of ideal quantum gases within this section.

The bath Hamiltonian that describes the ideal quantum gas assumes the form

$$\hat{\mathcal{H}}_B = \sum_k \varepsilon_k \hat{b}_k^\dagger \hat{b}_k, \quad (4.1)$$

where the operators \hat{b}_k^\dagger and \hat{b}_k create and annihilate particles with momentum k in the reservoir. The energy spectrum of an ideal quantum gas consisting of particles with mass m is given by

$$\varepsilon_k = \frac{\mathbf{k}^2}{2m}, \quad k = |\mathbf{k}|. \quad (4.2)$$

The thermal mean occupation of these energy levels obeys the distribution

$$\bar{n}(\varepsilon_k) = \frac{1}{e^{\beta(\varepsilon_k - \mu)} + \xi}, \quad (4.3)$$

with inverse temperature $\beta = 1/T$ and chemical potential μ . The parameter ξ assumes the value +1 for an ideal Fermi gas, resulting in the Fermi-Dirac statistics. For an ideal Bose gas the parameter ξ assumes the value -1 resulting in the Bose-Einstein statistics. In Fig. 4.1, we plot both statistics versus the frequency $\beta\omega$ for different chemical potentials. We note that the mean occupations fulfill the relation

$$\frac{\bar{n}(\omega + \mu)}{\bar{n}(-\omega + \mu)} = \begin{cases} e^{-\beta\omega} & , \text{ for fermions} \\ -e^{-\beta\omega} & , \text{ for bosons} \end{cases} \quad (4.4)$$

implying a thermal detailed balance. The additional minus sign for bosons enters this relation to ensure the positivity of the mean occupations because the Bose-Einstein statistics is formally negative for negative frequencies whereas the Fermi-Dirac statistics remains always positive. From the condition that the mean occupation can only take on positive values, we immediately conclude that for bosonic particles the chemical potential is restricted to values below the lowest eigenenergy.

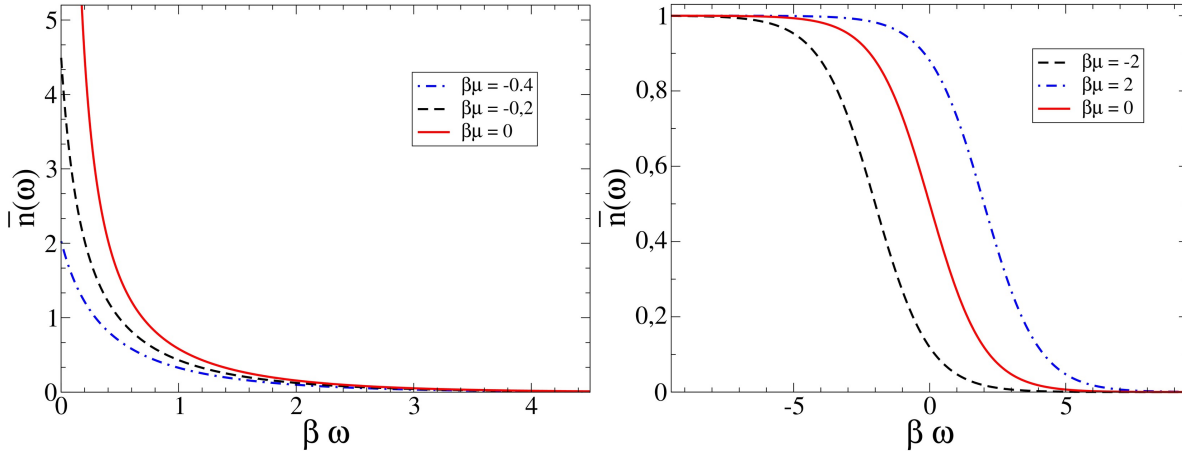


Figure 4.1: Plot of the Bose-Einstein (left) and Fermi-Dirac statistics (right) for different chemical potentials versus energy.

Since the ground-state energy of an ideal quantum gas is given by $\varepsilon_0 = 0$ the bosonic chemical potential is limited to negative values, i.e.,

$$-\infty < \mu < 0, \quad \text{for bosons.} \quad (4.5)$$

This observation for bosons is in contrast to the Fermi distribution where the chemical potential can in principle take on arbitrary values, i.e.,

$$-\infty < \mu < +\infty, \quad \text{for fermions.} \quad (4.6)$$

The chemical potential explicitly enters the mean occupation in Eq. (4.3), since we allow for matter exchange processes between the system and its environment. Due to these exchange processes a grand-canonical thermodynamic description of the whole system is required. Within the framework of the grand-canonical ensemble theory the chemical potential is introduced as a Lagrange multiplier fixing the mean total amount of particles \bar{N} in the reservoir. Therefore, the correct values for the chemical potential have to be determined self-consistently for a given mean number of particles and a fixed temperature in the reservoirs.

4.1.1 Grand-canonical chemical potential

Let us consider the situation of an ideal quantum gas confined in a 3D box of volume V . Then the mean total number of particles can be calculated according to

$$\bar{N} = g_S \sum_{k=0}^{\infty} \bar{n}(\varepsilon_k), \quad (4.7)$$

where we introduced the factor $g_S = 2S + 1$ which accounts for the spin-degeneracy of a particle with spin S . Using the thermodynamic limit where $\bar{N} \rightarrow \infty$ and $V \rightarrow \infty$

such that the mean particle density $n = \bar{N}/V$ remains constant, we can transform the summation over the k -modes in Eq. (4.7) into a continuous energy integral

$$\frac{g_S}{(2\pi)^3} \sum_{\mathbf{k}} \rightarrow \int_0^\infty g(E) dE. \quad (4.8)$$

The function $g(E)$ is the density-of-states which can be obtained from the phase space volume Ω . For a given energy E this phase space volume can be calculated by integrating over the whole available volume V and summing over all momenta \mathbf{k} which lie within the corresponding energy surface S_E . This results in the expression

$$\Omega(E) = \int_V d^3\mathbf{x} \int_{S_E} \frac{d^3\mathbf{k}}{(2\pi)^3}, \quad (4.9)$$

from which we can determine the density-of-states as a derivative with respect to the energy, i.e.,

$$g(E) = g_S \frac{d\Omega(E)}{dE}. \quad (4.10)$$

The \mathbf{k} integral in Eq. (4.9) can be solved using the energy dispersion relation from Eq. (4.2). It follows that

$$\int_{S_E} \frac{d^3\mathbf{k}}{(2\pi)^3} = \frac{4\pi}{(2\pi)^3} \int_0^{k_E} k^2 dk = \frac{1}{(2\pi)^2} (2m)^{3/2} \int_0^E \sqrt{\varepsilon_k} d\varepsilon_k, \quad (4.11)$$

which yields for the phase-space volume Ω the expression

$$\Omega(E) = \frac{1}{(2\pi)^2} (2m)^{3/2} V \int_0^E \sqrt{\varepsilon_k} d\varepsilon_k. \quad (4.12)$$

Consequently, the density-of-states of an ideal quantum gas in 3D reads as

$$g(E) = \frac{g_S V}{(2\pi)^2} (2m)^{3/2} \sqrt{E}, \quad (4.13)$$

with the usual dependence on the square root of the energy. With this result, we can now calculate the mean density of particles $n = \bar{N}/V$ in the reservoir according to

$$n = \frac{g_S}{(2\pi)^2} (2m)^{3/2} \int_0^\infty \frac{\sqrt{E}}{e^{\beta(E-\mu)} + \xi} dE = -g_S \frac{\xi}{\lambda_T^3} \text{Li}_{3/2}(-\xi z). \quad (4.14)$$

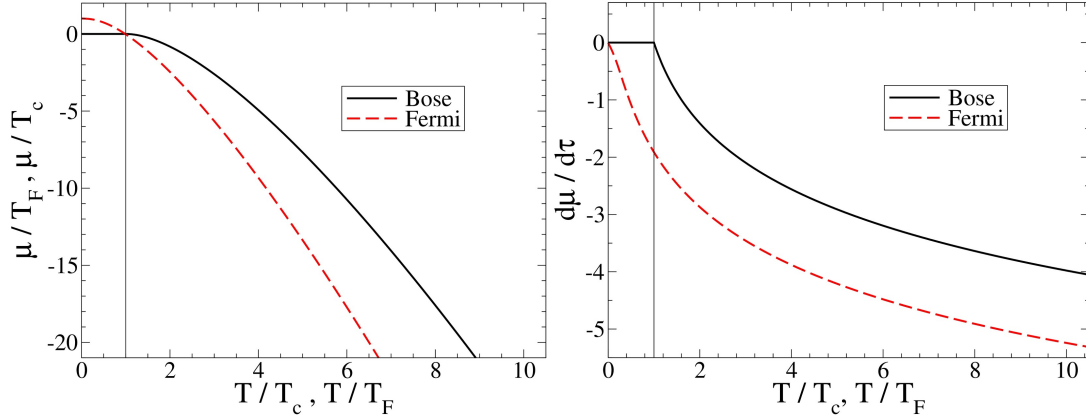


Figure 4.2: Plot of the temperature dependence of the chemical potential (left) and its derivative, with respect to the normalized reservoir temperature (right), for fermions (dashed line) and bosons (solid line) for a fixed particle density.

Here, we introduced the thermal de-Broglie wave length $\lambda_T = \sqrt{2\pi\beta/m}$, the fugacity $z = e^{\beta\mu}$, and the polylogarithm (see, e.g., Ref. [188])

$$\text{Li}_\alpha(z) = \frac{1}{\Gamma(\alpha)} \int_0^\infty \frac{x^\alpha - 1}{e^x/z - 1} dx = \sum_{k=1}^\infty \frac{z^k}{k^\alpha}, \quad (4.15)$$

where

$$\Gamma(\alpha) = \int_0^\infty dx x^{\alpha-1} e^{-x}, \quad (4.16)$$

is the Gamma function.

The above equation (4.14) implicitly defines a temperature and density dependent chemical potential $\mu(n, T)$. However, due to the highly nonlinear behavior of the polylogarithm the chemical potential can not be obtained analytically and we have to resort to numerical methods [189–194]. The resulting chemical potential as a function of the gas temperature is plotted in Fig. 4.2.

Moreover, using the properties of the polylogarithm

$$\frac{d}{dz} \text{Li}_\alpha(z) = \frac{1}{z} \text{Li}_{\alpha-1}(z), \quad (4.17)$$

we are able to calculate the derivatives of the chemical potential with respect to temperature and density from Eq. (4.14). Performing a derivative with respect to temperature on both sides of Eq. (4.14) and rearranging the resulting terms, we find the relation

$$\frac{\partial \mu(T, n)}{\partial T} = \frac{\mu}{T} - \frac{3\text{Li}_{3/2}(-\xi z)}{2\text{Li}_{1/2}(-\xi z)}. \quad (4.18)$$

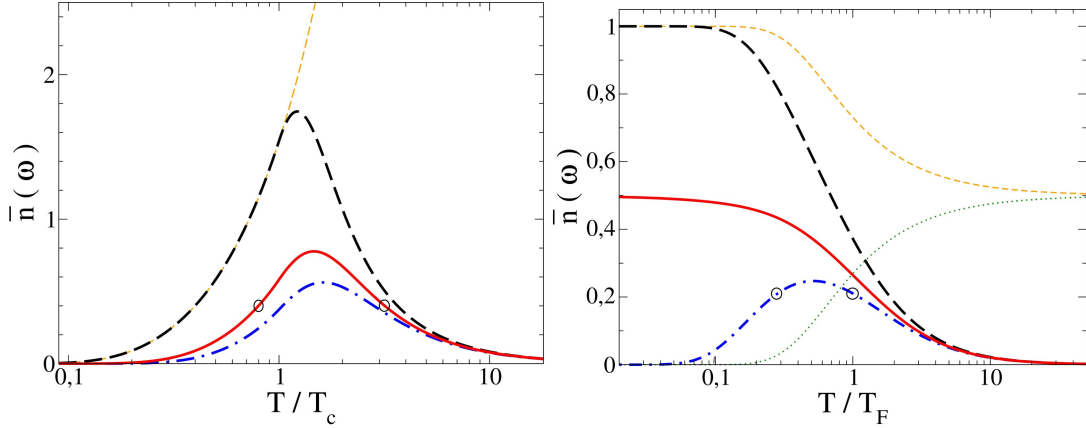


Figure 4.3: Mean occupation for ideal quantum gases with temperature- and density-dependent chemical potential. Left: For an ideal Bose gas at $\omega = 0.5T_c$ (dashed line), $\omega = T_c$ (solid line) and $\omega = 1.3T_c$ (dot-dashed line). Using a constant chemical potential, e.g., $\omega - \mu = 0.5T_c$ (thin, dashed line) the occupation increases exponentially with the temperature. Right: For an ideal Fermi gas at $\omega = 0.5T_F$ (dashed line), $\omega = T_F$ (solid line) and $\omega = 1.3T_F$ (dot-dashed line). The fermionic occupation for a constant chemical potential approaches 1/2 for large temperature. This value is approached, either from above if $\omega - \mu < 0$, e.g., $\omega - \mu = -T_F$ (thin, dashed line), or from below if $\omega - \mu > 0$, e.g., $\omega - \mu = T_F$ (thin, dotted line). The circles indicate a set of temperatures with the same occupation for a given transition frequency (see Fig. 4.6 and `figrefC3:F:BoseSteadyStateCurrent`).

In the same way we can calculate the derivative with respect to the density and obtain

$$\frac{\partial \mu(T, n)}{\partial n} = \frac{T \operatorname{Li}_{3/2}(-\xi z)}{n \operatorname{Li}_{1/2}(-\xi z)}. \quad (4.19)$$

Hence, we see that the derivatives of the chemical potential with respect to the reservoir temperature and particle density can be obtained as analytic functions of the chemical potential, leaving its determination to be the only numerical problem we have to solve.

Within the following analysis, we will often observe dependencies on the mean occupations of the reservoirs. It is therefore instructive to investigate the influence of the temperature and density dependent chemical potential on these mean occupations. Hence, we insert the numerical result for the chemical potential as depicted in Fig. 4.2 into the definition of the mean occupations in Eq. (4.3). In Fig. 4.3, we plotted the resulting occupations of different energy levels in fermionic and bosonic reservoirs.

In the bosonic case, we observe that the mean occupation of a given energy level is peaked around a specific characteristic temperature. For temperatures lower than this characteristic temperature the mean occupation of the considered energy level is decreased. This effect is related to the fact that for lower temperatures the particles occupy lower energy levels. Since the density is fixed, this increase of the occupations of lower levels is accompanied by a decrease of the occupation of the higher energy levels. Analogously, for high temperatures the particles are excited to higher energy levels and the mean occupation of the lower energy levels decreases. Thus, the occupation of a given energy level approaches zero for large temperature. This high temperature behavior is in strong contrast to the conventional mean occupation with fixed chemical potential. Here, one would expect an exponential growth (thin, dashed line) with temperature which appears linear in the logarithmic plot for high temperatures.

In case of ideal Fermi gases, we find a similar behavior if the considered energy level lies above the Fermi energy (dot-dashed line). The reasons for this behavior are the same as discussed for bosons. However, the situation changes if one considers the occupation of an energy level which lies below the Fermi energy (dashed line). Here, the occupation becomes constant as the temperature is decreased. This is caused by the Pauli principle which forbids that the fermions can occupy an energy level which is already filled. Thus, further decreasing the temperature does not result in a decrease of the occupation of the monitored energy level as we observed for the bosonic case, since the lower energy levels are already filled. Contrary, for a constant chemical potential, we find a different high temperature behavior. Here, the mean occupation assumes the value $1/2$ with increasing temperature independent of the monitored energy level. This constant value is either approached from above if $\omega - \mu < 0$, or approached from below for $\omega - \mu > 0$.

We therefore find that the temperature dependent chemical potential strongly affects the high temperature behavior of the mean occupations for both, bosons and fermions.

4.1.2 Bose-Einstein condensation

The derivation for the mean total particle number in Eq. (4.14) presented in the previous paragraph is actually only valid for fermions. If we consider bosonic particle reservoirs, it is not completely correct, since it does not correctly account for the bosonic ground-state.

Taking a look at the bosonic mean occupation as plotted in Fig. 4.1, we observe that as the chemical potential approaches zero, i.e., $\beta\mu \rightarrow 0$, the mean occupation of the ground-state, where $\omega = 0$, becomes macroscopic. This macroscopic occupation of the bosonic ground-state is known in literature as Bose-Einstein condensation. Despite the fact that the ground-state becomes macroscopically occupied, the corresponding spectral weight \sqrt{E} in the energy integral in Eq. (4.14) becomes zero.

Therefore, one has to take special care of the bosonic ground-state when replacing the summation over the k -modes with an integral in order to correctly describe the phenomenon of Bose-Einstein condensation. Adding the ground-state occupation $n_0 = g_S z / (1 - z)$ to the mean total particle number in Eq. (4.14) yields the correct expression for the mean particle density $n = \bar{N}/V$ which reads as

$$n = \underbrace{-g_S \frac{\xi}{\lambda_T^3} \text{Li}_{3/2}(-\xi z)}_{n_{\text{ex}}} + \underbrace{g_S \frac{z}{1-z} \delta_{\xi+1,0}}_{n_0}, \quad (4.20)$$

where the first part n_{ex} represents the fraction of particles that are in excited energy levels whereas the second part n_0 is the fraction of particles in the ground-state. As indicated by the Kronecker delta function this additional ground-state contribution is only present for bosonic particles. Furthermore, we note that the fraction of particles in the ground-state diverges as z approaches one, i.e., when $\beta\mu \rightarrow 0$.

In the left panel of Fig. 4.2, we plot the chemical potential for a fixed mean particle density as a function of the reservoir temperature for both, bosonic and fermionic reservoirs. We observe that for bosons there exists a critical temperature T_c below which the chemical potential vanishes. Consequently, at this critical temperature the bosonic ground-state starts to be macroscopically occupied and Bose-Einstein condensation sets in. This density-dependent critical temperature can be obtained from Eq. (4.20) with $n_0 = 0$ and $z = 1$. This yields

$$T_c = T_c(n) = \frac{2\pi}{m} \left(\frac{n}{g_S \zeta(3/2)} \right)^{2/3}, \quad (4.21)$$

where $\text{Li}_{3/2}(1) = \zeta(3/2)$ and $\zeta(x)$ is the Riemann zeta function. For the case of a fixed temperature, we can rewrite this expression to obtain a corresponding critical particle density n_c which is defined as

$$n_c = n_c(T) = \frac{g_S}{\lambda_T^3} \zeta(3/2). \quad (4.22)$$

Here, it is convenient to introduce the dimensionless temperature $\tau = T/T_c$ and the dimensionless density $\nu = n/n_c$ for the bosonic reservoirs. We note that the dimensionless temperature and density fulfill the relation

$$\tau = \nu^{-2/3}. \quad (4.23)$$

Subsequently, reformulating Eq. (4.20) with the help of these dimensionless variables results in the fact that the chemical potential can be treated as a function of a single dimensionless variable only. Additionally, we can deduce the ground-state occupation as a function of the dimensionless temperature which results in the famous relation

$$n_0 = n (1 - \tau^{3/2}), \quad \text{for } T < T_c, \quad (4.24)$$

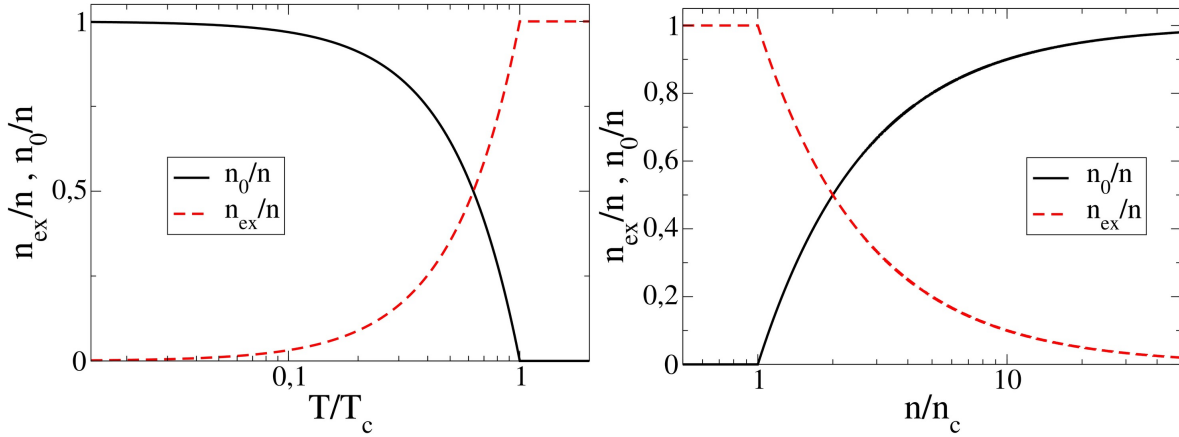


Figure 4.4: Plot of the occupation of the bosonic ground-state (solid line) and the excited states (dashed line) versus the dimensionless temperature (left) and the dimensionless density (right). Below the critical temperature T_c and above the critical density n_c , Bose-Einstein condensation sets in. At $T = 0$ the ideal Bose gas forms a pure Bose-Einstein condensate.

which we plot in Fig. 4.4. We observe that Bose-Einstein condensation sets in at the critical values for the temperature and the particle density. As the ground-state becomes occupied the number of thermally excited particles decreases. Since the particles in the ground-state do not possess enough energy they can not participate in the transport process. Thus, transport is only facilitated by the particles in the excited states. Only at $T = 0$ or for $n \rightarrow \infty$ all particles are in the ground-state and the reservoir forms a pure Bose-Einstein condensate.

Correspondingly, we can find a density-dependent characteristic temperature T_F in the case of fermionic particle reservoirs as well. This Fermi temperature is defined as

$$T_F = T_F(n) = \frac{1}{2m} \left(\frac{6\pi^2 n}{g_S} \right)^{2/3}. \quad (4.25)$$

It relates to the Fermi energy which is the value of the chemical potential at absolute zero, i.e., $\mu(T = 0) = E_F$, according to $E_F = T_F$. Again, we can reformulate Eq. (4.25) to obtain a temperature dependent characteristic Fermi density that is defined as

$$n_F = n_F(T) = \frac{4g_S}{3\sqrt{\pi}\lambda_T^3}. \quad (4.26)$$

Introducing these characteristic temperature and energy for the fermionic system allows to introduce dimensionless variables $\tau = T/T_F$ and $\nu = n/n_F$ in correspondence to the bosonic ones. Keeping either the temperature or the particle density constant and inserting the dimensionless variables τ or ν into Eq. (4.20) leads to the chemical potential as a function of a single dimensionless variable only, for both, the ideal Fermi and the ideal Bose gas.

4.2 Transport with ultracold fermions

After we reviewed the properties of ideal quantum gas reservoirs in 3D within the previous section, we now apply these results to a fermionic transport setup. Hence, in the following, we consider a few-level fermionic quantum system connected to two fermionic terminals. In particular, we investigate the effect of the temperature and density dependent chemical potential on the steady-state transport properties through this system.

4.2.1 Transport system

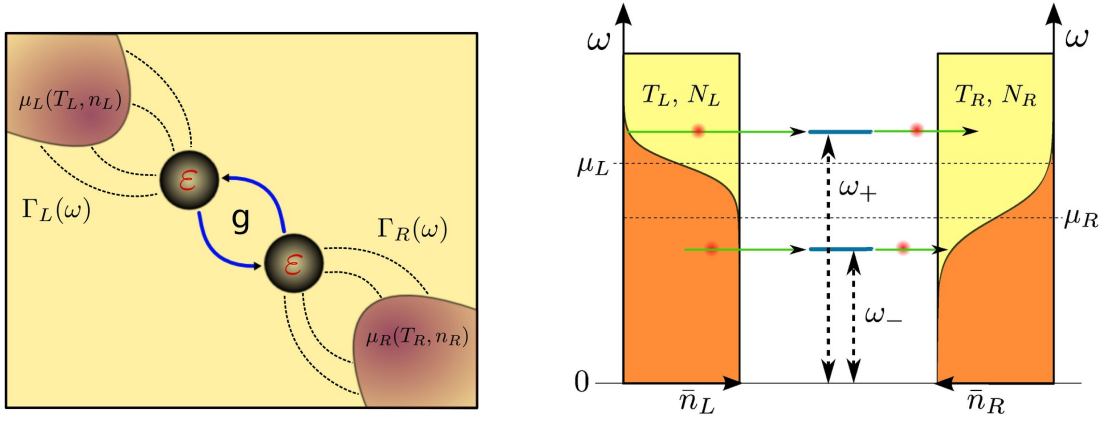


Figure 4.5: Fermionic transport setup (left) and the corresponding energy representation in the system eigenbasis (right). The atomic reservoirs $\alpha \in \{L, R\}$ are in thermal equilibrium characterized by temperature T_α and chemical potential $\mu_\alpha = \mu(T_\alpha, N_\alpha)$ for fixed particle number N_α . The mean occupation \bar{n}_α of energy ω is given by the Fermi-Dirac distribution. The system is composed of two identical quantum dot-like structures with on-site energy ε , that are coherently coupled with an amplitude g . The coupling to the reservoirs is facilitated via the rates $\Gamma_\alpha(\omega)$. In the Coulomb blockade regime this double quantum-dot structure has two internal transitions with the energies $\omega_- = \varepsilon - g$ and $\omega_+ = \varepsilon + g$.

We consider a fermionic system as shown in the left panel of Fig. 4.5. This system is composed of a double quantum dot which is held in the Coulomb blockade regime and coupled to two fermionic terminals. The corresponding energy representation of this setup is sketched in the right panel of Fig. 4.5.

The transport double-dot system is described by the Hamiltonian

$$\hat{\mathcal{H}}_S^{\text{fermi}} = \varepsilon (\hat{c}_L^\dagger \hat{c}_L + \hat{c}_R^\dagger \hat{c}_R) + g (\hat{c}_L^\dagger \hat{c}_R + \hat{c}_R^\dagger \hat{c}_L) + U \hat{c}_L^\dagger \hat{c}_L \hat{c}_R^\dagger \hat{c}_R. \quad (4.27)$$

Here, the operators \hat{c}_α and \hat{c}_α^\dagger which obey the fermionic anti-commutation relation

$$\{\hat{c}_\alpha, \hat{c}_\beta^\dagger\} = \delta_{\alpha,\beta}, \quad \text{and} \quad \{\hat{c}_\alpha, \hat{c}_\beta\} = \{\hat{c}_\alpha^\dagger, \hat{c}_\beta^\dagger\} = 0, \quad (4.28)$$

annihilate and create a fermionic particle in quantum dot α , respectively. The two quantum dots are denoted by the labels L and R and they are coupled via a coherent tunneling process with amplitude g . Each dot can be empty or occupied by a single particle. A filled quantum dot increases the system energy by the amount ε . In order to have a brief notation, we explicitly consider the case that both quantum dots have the same energy ε when filled. The corresponding eigenstates for each dot $\alpha \in \{L, R\}$ are the Fock-states

$$|\alpha\rangle = \begin{cases} |1\rangle, & \text{if dot } \alpha \text{ is filled} \\ |0\rangle, & \text{if dot } \alpha \text{ is empty} \end{cases}. \quad (4.29)$$

Subsequently, the Fock-states of the double-dot are obtained as a direct product of the single-dot Fock-states, which yields the definition

$$|\alpha\alpha'\rangle = |\alpha\rangle \otimes |\alpha'\rangle. \quad (4.30)$$

In the Coulomb blockade limit the Coulomb repulsion $U \gg \varepsilon, g$ is the dominating energy scale. Hence, the state $|11\rangle$ corresponding to a doubly occupied double quantum dot does not take part in the long-time dynamics and can be safely neglected. The remaining energy eigenstates of the system are the vacuum state

$$|0\rangle = |00\rangle, \quad (4.31)$$

and the superposition states

$$|- \rangle = \frac{1}{\sqrt{2}} (|01\rangle - |10\rangle), \quad |+\rangle = \frac{1}{\sqrt{2}} (|01\rangle + |10\rangle), \quad (4.32)$$

with the eigenvalues

$$\omega_0 = 0, \quad \omega_- = \varepsilon - g, \quad \omega_+ = \varepsilon + g. \quad (4.33)$$

As shown in Fig. 4.5, each quantum dot is coupled to a respective reservoir. Hence, the total system-bath interaction Hamiltonian for the fermionic setup is given by

$$\hat{\mathcal{H}}_1 = \sum_{\alpha,k} (t_{\alpha,k} \hat{b}_{\alpha,k}^\dagger \hat{c}_\alpha + \text{h.c.}), \quad (4.34)$$

where the tunneling amplitude of a particle hopping from mode k of reservoir α into the respective quantum dot or vice versa is proportional to $t_{\alpha,k}^*$ and $t_{\alpha,k}$, respectively. We can split this interaction Hamiltonian into a sum over direct products of system- and bath operators only, according to Eq. (2.9). We find the decomposition

$$\hat{\mathcal{H}}_1 = \sum_{i \in \{1,2\}} \sum_{\alpha \in \{L,R\}} \hat{A}_i^{(\alpha)} \otimes \hat{B}_i^{(\alpha)}, \quad (4.35)$$

where, in correspondence with Sec. 3.2, we introduce the system- and bath operators in their Jordan-Wigner representation as

$$\begin{aligned}\hat{A}_1^{(\alpha)} &= \hat{c}_\alpha, & \hat{B}_1^{(\alpha)} &= \sum_{k=0}^{\infty} t_{\alpha,k} \hat{b}_{\alpha,k}^\dagger, \\ \hat{A}_2^{(\alpha)} &= \hat{c}_\alpha^\dagger, & \hat{B}_2^{(\alpha)} &= \sum_{k=0}^{\infty} t_{\alpha,k}^* \hat{b}_{\alpha,k}.\end{aligned}\quad (4.36)$$

Each reservoir is assumed to be in its respective thermal equilibrium state defined as

$$\bar{\rho}_B^{(\alpha)} = \frac{1}{\mathcal{Z}_\alpha} e^{-\beta_\alpha (\hat{\mathcal{H}}_B^{(\alpha)} - \mu_\alpha \hat{N}_B^{(\alpha)})}. \quad (4.37)$$

Here, \mathcal{Z}_α is the partition function of an ideal Fermi gas which can be calculated to

$$\mathcal{Z}_\alpha = \text{Tr} \left\{ e^{-\beta_\alpha (\hat{\mathcal{H}}_B^{(\alpha)} - \mu_\alpha \hat{N}_B^{(\alpha)})} \right\} = \prod_k \sum_{n_k=0}^1 e^{-\beta_\alpha (\varepsilon_k^{(\alpha)} - \mu_\alpha) n_k} = \prod_k [1 + e^{-\beta_\alpha (\varepsilon_k - \mu_\alpha)}]. \quad (4.38)$$

Note, that in the last equality we assumed $\varepsilon_k^{(\alpha)} = \varepsilon_k$, i.e., that both reservoirs consist of the same type of particles with the same mass $m_\alpha = m$. This choice is not essential for the further calculations, however it corresponds to the actual experimental realization [104]. Now, we can use these bath properties to calculate the bath correlation functions according to Eq. (2.68). We find that the only non vanishing correlations are given by

$$C_{12}^{(\alpha)}(\tau) = \sum_k \bar{n}_\alpha(\varepsilon_k) |t_{\alpha,k}|^2 e^{i\varepsilon_k \tau} = \int_{-\infty}^{\infty} d\omega \rho^{(\alpha)}(\omega) \bar{n}_\alpha(\omega) e^{i\omega \tau}, \quad (4.39)$$

$$C_{21}^{(\alpha)}(\tau) = \sum_k [1 - \bar{n}_\alpha(\varepsilon_k)] |t_{\alpha,k}|^2 e^{-i\varepsilon_k \tau} = \int_{-\infty}^{\infty} d\omega \rho^{(\alpha)}(\omega) [1 - \bar{n}_\alpha(\omega)] e^{-i\omega \tau}, \quad (4.40)$$

where the mean occupation $\bar{n}_\alpha(\omega)$ for each bath is given by the Fermi-Dirac statistics defined as

$$\bar{n}_\alpha(\omega) = \frac{1}{e^{\beta_\alpha(\omega - \mu_\alpha)} + 1}, \quad (4.41)$$

in correspondence with Eq. (4.3). Additionally, in the above equations we introduced the density-of-states

$$\rho^{(\alpha)}(\omega) = \sum_k |t_{\alpha,k}|^2 \delta(\varepsilon_k - \omega), \quad (4.42)$$

for each reservoir, respectively. Using these results, we can calculate the even Fourier transform bath correlation functions in the intuitive Fermi golden rule form [195]

$$\begin{aligned}\gamma_{12}^{(\alpha)}(-\omega) &= \Gamma_\alpha(\omega) \bar{n}_\alpha(\omega), \\ \gamma_{21}^{(\alpha)}(\omega) &= \Gamma_\alpha(\omega) [1 - \bar{n}_\alpha(\omega)],\end{aligned}\quad (4.43)$$

with the energy dependent bare tunneling rates

$$\Gamma_\alpha(\omega) = 2\pi\rho^{(\alpha)}(\omega). \quad (4.44)$$

We observe that each bath separately fulfills a detailed balance condition, i.e.,

$$\frac{\gamma_{12}^{(\alpha)}(-\omega)}{\gamma_{21}^{(\alpha)}(\omega)} = \frac{\bar{n}_\alpha(\omega)}{1 - \bar{n}_\alpha(\omega)} = e^{-\beta_\alpha(\omega - \mu_\alpha)}. \quad (4.45)$$

Note, in order to shorten our notation, we henceforth work in the so called wide-band limit. This limit assumes that the rates $\Gamma_\alpha(\omega) = \Gamma_\alpha$ are independent of the energy, i.e., that the density-of-states is approximately flat.

4.2.2 Liouvillian

In Sec. 2.7, we showed that in the energy eigenbasis of the system the BMS-master equation for the populations becomes an effective rate equation of the form presented in Eq. (2.54). In Liouville space the rate matrix is defined by the rates in Eq. (2.48) via Eq. (2.61). For the fermionic setup shown in Fig. 4.5, we already introduced the eigensystem in the previous section 4.2.1. Together with the system-bath interaction Hamiltonian from Eq. (4.34) and the rates from Eq. (4.43), we find

$$\gamma_{ab,ba} = \sum_\alpha \left[\gamma_{12}^{(\alpha)}(\omega_{a,b}) \left| \langle a | \hat{A}_1^{(\alpha)} | b \rangle \right|^2 + \gamma_{21}^{(\alpha)}(\omega_{a,b}) \left| \langle b | \hat{A}_1^{(\alpha)} | a \rangle \right|^2 \right]. \quad (4.46)$$

Here, the states $|a\rangle$ and $|b\rangle$ have to be chosen from the set of system eigenstates $\{|0\rangle, |-\rangle, |+\rangle\}$. Obviously, the only nonvanishing transition rates are

$$\gamma_{0+,+0} = \frac{1}{2} \sum_\alpha \Gamma_\alpha(\omega_+) \bar{n}_\alpha(\omega_+), \quad \gamma_{0-, -0} = \frac{1}{2} \sum_\alpha \Gamma_\alpha(\omega_-) \bar{n}_\alpha(\omega_-), \quad (4.47)$$

$$\gamma_{+0,0+} = \frac{1}{2} \sum_\alpha \Gamma_\alpha(\omega_+) [1 - \bar{n}_\alpha(\omega_+)], \quad \gamma_{-0,0-} = \frac{1}{2} \sum_\alpha \Gamma_\alpha(\omega_-) [1 - \bar{n}_\alpha(\omega_-)]. \quad (4.48)$$

Inserting these results into the rate equation for the populations in Eq. (2.54) and subsequently performing the Fourier transform from Eq. (2.75) leads to the evolution of the reduced system density matrix in the Liouville-space representation which reads as

$$\frac{\partial}{\partial t} \begin{pmatrix} \rho_0 \\ \rho_- \\ \rho_+ \end{pmatrix} = \mathcal{W}(\chi, \eta) \cdot \begin{pmatrix} \rho_0 \\ \rho_- \\ \rho_+ \end{pmatrix}. \quad (4.49)$$

Here, the particle- and energy-counting field dependent Liouvillian can be decomposed into

$$\mathcal{W}(\chi, \eta) = -\mathcal{W}_0 + \mathcal{W}_+(\chi, \eta) + \mathcal{W}_-(\chi, \eta). \quad (4.50)$$

Thus, we can uniquely identify the coherent evolution and the jump terms which in the wide-band limit are given by

$$\begin{aligned}
 \mathcal{W}_0 &= \sum_{\alpha} \frac{\Gamma_{\alpha}}{2} \begin{pmatrix} \bar{n}_{\alpha}(\omega_-) + \bar{n}_{\alpha}(\omega_+) & 0 & 0 \\ 0 & 1 - \bar{n}_{\alpha}(\omega_-) & 0 \\ 0 & 0 & 1 - \bar{n}_{\alpha}(\omega_+) \end{pmatrix}, \\
 \mathcal{W}_+(\chi, \eta) &= \sum_{\alpha} \frac{\Gamma_{\alpha}}{2} \begin{pmatrix} 0 & e^{i(\chi_{\alpha} - \eta_{\alpha} \omega_-)} [1 - \bar{n}_{\alpha}(\omega_-)] & e^{i(\chi_{\alpha} - \eta_{\alpha} \omega_+)} [1 - \bar{n}_{\alpha}(\omega_+)] \\ 0 & 0 & 0 \\ 0 & 0 & 0 \end{pmatrix}, \\
 \mathcal{W}_-(\chi, \eta) &= \sum_{\alpha} \frac{\Gamma_{\alpha}}{2} \begin{pmatrix} 0 & 0 & 0 \\ e^{-i(\chi_{\alpha} - \eta_{\alpha} \omega_-)} \bar{n}_{\alpha}(\omega_-) & 0 & 0 \\ e^{-i(\chi_{\alpha} - \eta_{\alpha} \omega_+)} \bar{n}_{\alpha}(\omega_+) & 0 & 0 \end{pmatrix}. \tag{4.51}
 \end{aligned}$$

Using the above equations, we find that the steady-state of the system according to Eq. (2.90) is given by

$$\bar{\rho} = \begin{pmatrix} \bar{\rho}_0 \\ \bar{\rho}_- \\ \bar{\rho}_+ \end{pmatrix} = \frac{1}{\theta} \begin{pmatrix} \gamma_{-0,0-} \gamma_{+0,0+} \\ \gamma_{0-, -0} \gamma_{+0,0+} \\ \gamma_{-0,0-} \gamma_{0+, +0} \end{pmatrix} = \frac{1}{\theta} \sum_{\alpha, \beta} \Gamma_{\alpha} \Gamma_{\beta} \begin{pmatrix} [1 - \bar{n}_{\alpha}(\omega_-)] [1 - \bar{n}_{\beta}(\omega_+)] \\ \bar{n}_{\alpha}(\omega_-) [1 - \bar{n}_{\beta}(\omega_+)] \\ [1 - \bar{n}_{\alpha}(\omega_-)] \bar{n}_{\beta}(\omega_+) \end{pmatrix}, \tag{4.52}$$

where we defined the normalization constant θ as

$$\theta = \gamma_{0+, +0} \gamma_{-0,0-} + \frac{1}{2} (\Gamma_L + \Gamma_R) \gamma_{+0,0+} = \frac{1}{4} \sum_{\alpha, \beta} \Gamma_{\alpha} \Gamma_{\beta} [1 - \bar{n}_{\alpha}(\omega_+) \bar{n}_{\beta}(\omega_-)]. \tag{4.53}$$

These steady-state populations have the property

$$\frac{\bar{\rho}_-}{\bar{\rho}_0} = \frac{\gamma_{0-, -0}}{\gamma_{-0,0-}} = \frac{\sum_{\alpha} \Gamma_{\alpha} \bar{n}_{\alpha}(\omega_-)}{\sum_{\alpha} \Gamma_{\alpha} [1 - \bar{n}_{\alpha}(\omega_-)]}, \quad \frac{\bar{\rho}_+}{\bar{\rho}_0} = \frac{\gamma_{0+, +0}}{\gamma_{+0,0+}} = \frac{\sum_{\alpha} \Gamma_{\alpha} \bar{n}_{\alpha}(\omega_+)}{\sum_{\alpha} \Gamma_{\alpha} [1 - \bar{n}_{\alpha}(\omega_+)]}, \tag{4.54}$$

which results in a global detailed balance relation if only a single reservoir would be present, in full accordance with our finding in Eq. (4.45).

4.2.3 Steady-state currents

We start our investigation of the effect of a temperature and density dependent chemical potential by calculating the steady-state particle and energy currents according to Eq. (2.93) and Eq. (2.94). This yields for the steady-state currents measured at reservoir α the relations

$$J_N^{(\alpha)} = \mathcal{I}_-^{(\alpha)} + \mathcal{I}_+^{(\alpha)}, \quad J_E^{(\alpha)} = \omega_- \mathcal{I}_-^{(\alpha)} + \omega_+ \mathcal{I}_+^{(\alpha)}, \tag{4.55}$$

where we defined the abbreviation

$$\mathcal{I}_n^{(\alpha)} = -\frac{\Gamma_{\alpha}}{2} \{ \bar{n}_{\alpha}(\omega_n) \bar{\rho}_0 - [1 - \bar{n}_{\alpha}(\omega_n)] \bar{\rho}_n \}, \tag{4.56}$$

and used the wide-band limit, i.e., $\Gamma_\alpha(\omega) = \Gamma_\alpha$, again.

With the steady-state density vector given in Eq. (4.52) the full expressions for these currents can be obtained resulting in

$$\begin{aligned}
 J_N^{(\alpha)} &= -\frac{\Gamma_\alpha}{2} \left\{ [\bar{n}_\alpha(\omega_-) + \bar{n}_\alpha(\omega_+)] - [1 - \bar{n}_\alpha(\omega_-)] \frac{\bar{\rho}_-}{\bar{\rho}_0} - [1 - \bar{n}_\alpha(\omega_+)] \frac{\bar{\rho}_+}{\bar{\rho}_0} \right\} \bar{\rho}_0 \\
 &= -2\Gamma_\alpha \left\{ [\bar{n}_\alpha(\omega_-) + \bar{n}_\alpha(\omega_+)] - \frac{[1 - \bar{n}_\alpha(\omega_-)] \sum_\beta \Gamma_\beta \bar{n}_\beta(\omega_-)}{\sum_\beta \Gamma_\beta [1 - \bar{n}_\beta(\omega_-)]} \right. \\
 &\quad \left. - \frac{[1 - \bar{n}_\alpha(\omega_+)] \sum_\beta \Gamma_\beta \bar{n}_\beta(\omega_+)}{\sum_\beta \Gamma_\beta [1 - \bar{n}_\beta(\omega_+)]} \right\} \frac{\sum_{\delta,\gamma} \Gamma_\delta \Gamma_\gamma [1 - \bar{n}_\delta(\omega_-)] [1 - \bar{n}_\gamma(\omega_+)]}{\sum_{\delta,\gamma} \Gamma_\delta \Gamma_\gamma [1 - \bar{n}_\delta(\omega_+)] \bar{n}_\gamma(\omega_-)}, \quad (4.57)
 \end{aligned}$$

and

$$\begin{aligned}
 J_E^{(\alpha)} &= -2\Gamma_\alpha \left\{ [\omega_- \bar{n}_\alpha(\omega_-) + \omega_+ \bar{n}_\alpha(\omega_+)] - \omega_- \frac{[1 - \bar{n}_\alpha(\omega_-)] \sum_\beta \Gamma_\beta \bar{n}_\beta(\omega_-)}{\sum_\beta \Gamma_\beta [1 - \bar{n}_\beta(\omega_-)]} \right. \\
 &\quad \left. - \omega_+ \frac{[1 - \bar{n}_\alpha(\omega_+)] \sum_\beta \Gamma_\beta \bar{n}_\beta(\omega_+)}{\sum_\beta \Gamma_\beta [1 - \bar{n}_\beta(\omega_+)]} \right\} \frac{\sum_{\delta,\gamma} \Gamma_\delta \Gamma_\gamma [1 - \bar{n}_\delta(\omega_-)] [1 - \bar{n}_\gamma(\omega_+)]}{\sum_{\delta,\gamma} \Gamma_\delta \Gamma_\gamma [1 - \bar{n}_\delta(\omega_+)] \bar{n}_\gamma(\omega_-)}. \quad (4.58)
 \end{aligned}$$

We find that steady-state currents respect energy and particle conservation, i.e.,

$$J_N \equiv J_N^{(L)} = -J_N^{(R)} \quad \text{and} \quad J_E \equiv J_E^{(L)} = -J_E^{(R)}, \quad (4.59)$$

in accordance with Eq. (2.95). However, since the complete expressions for the currents in Eq. (4.57) and Eq. (4.58) are quite complicated, we start by investigating the currents in the limit of a single transition frequency only in order to gain a better physical insight. Effectively, this limit can be obtained by shifting the second transition energy to high values such that transport through this level is strongly suppressed. In consequence, we find steady-state currents involving the lowest transition energy only which read

$$\lim_{\omega_+ \rightarrow \infty} J_N^{(L)} = \frac{\Gamma_L \Gamma_R}{2(\Gamma_L + \Gamma_R)} [\bar{n}_L(\omega_-) - \bar{n}_R(\omega_-)], \quad (4.60)$$

$$\lim_{\omega_+ \rightarrow \infty} J_E^{(L)} = \omega_- \left[\lim_{\omega_+ \rightarrow \infty} J_N^{(L)} \right]. \quad (4.61)$$

Note that the exact currents through a system with a single transition frequency ω calculated in the BMS approximation are given by

$$J_N^{(L)} = \frac{\Gamma_L \Gamma_R}{\Gamma_L + \Gamma_R} [\bar{n}_L(\omega) - \bar{n}_R(\omega)], \quad J_N^{(L)} = \omega J_E^{(L)}. \quad (4.62)$$

Hence, by comparison, we find that the limit currents in Eq. (4.60) and Eq. (4.61) correspond to half the exact current through a system with a single transition frequency. The additional pre-factor arises due to the limiting procedure which disregards the correct normalization of the steady-state density matrix.

We observe that for systems with a single transition frequency, we enter the tight-coupling limit where energy- and particle current are proportional to each other. Furthermore, the particle current through a system with a single transition energy is proportional to the difference of the mean occupations of the corresponding energy level in the reservoirs. Hence, there will be always a finite particle and energy current as long as there is a nonvanishing difference in the occupations of the reservoirs. The steady-state currents only vanish if the mean occupation of the energy levels in the reservoirs are the same.

In order to analyze if this effect is also visible if more transition frequencies are present in the system, we plot the particle current through a double-dot system with two transition frequencies in Fig. 4.6 according to Eq. (4.55).

We observe two different regimes reflecting the different behavior of the mean occupations for energies below and above the Fermi energy. If at least one transition energy lies below the Fermi energy, as shown in panel (a) of Fig. 4.6, we observe a finite steady-state current which flows with the chemical potential bias but against the thermal bias. This is due to the fact that in the hotter reservoir the particles are excited to higher energy states. Since the density is fixed there are not enough particles to refill the depleted energy levels. The occupation in these levels decreases leading to a flow from the colder reservoir, where the energy levels are occupied, to the hotter reservoir. This behavior is a consequence of the mean occupation under the constraint of constant particle density. However, one obtains qualitatively the same result for an independent chemical potential as long as the condition $\omega_- - \mu < 0$ is fulfilled.

If all transition energies are above the Fermi energy, as shown in the panels (b) and (c) of Fig. 4.6, this behavior changes such that for a small reservoir temperatures the steady-state current flows against the chemical potential bias and with the thermal bias. However, if the temperatures are increased above a critical value the current flows against the thermal bias again.

To illustrate how the temperature dependent chemical potential affects the Fermi statistics such that increasing the temperature in one reservoir changes the direction of the particle current through a single transport channel, we sketch the mean occupations in both reservoirs for different temperatures in Fig. 4.7.

Moreover, in order to understand the emergence of the regions where the steady-state current vanishes, it is recommendable to study the case of a single system transition frequency first. Taking a look at Eq. (4.60), we see that the critical lines where the current vanishes are defined by the relation $\bar{n}_L(\omega_-) = \bar{n}_R(\omega_-)$. This is trivially fulfilled in equilibrium where $\Delta_\beta = \Delta_n = 0$.

$$\Delta_\beta = \beta_L - \beta_R = 0 \quad \text{and} \quad \Delta_\mu = \mu_L - \mu_R = 0. \quad (4.63)$$

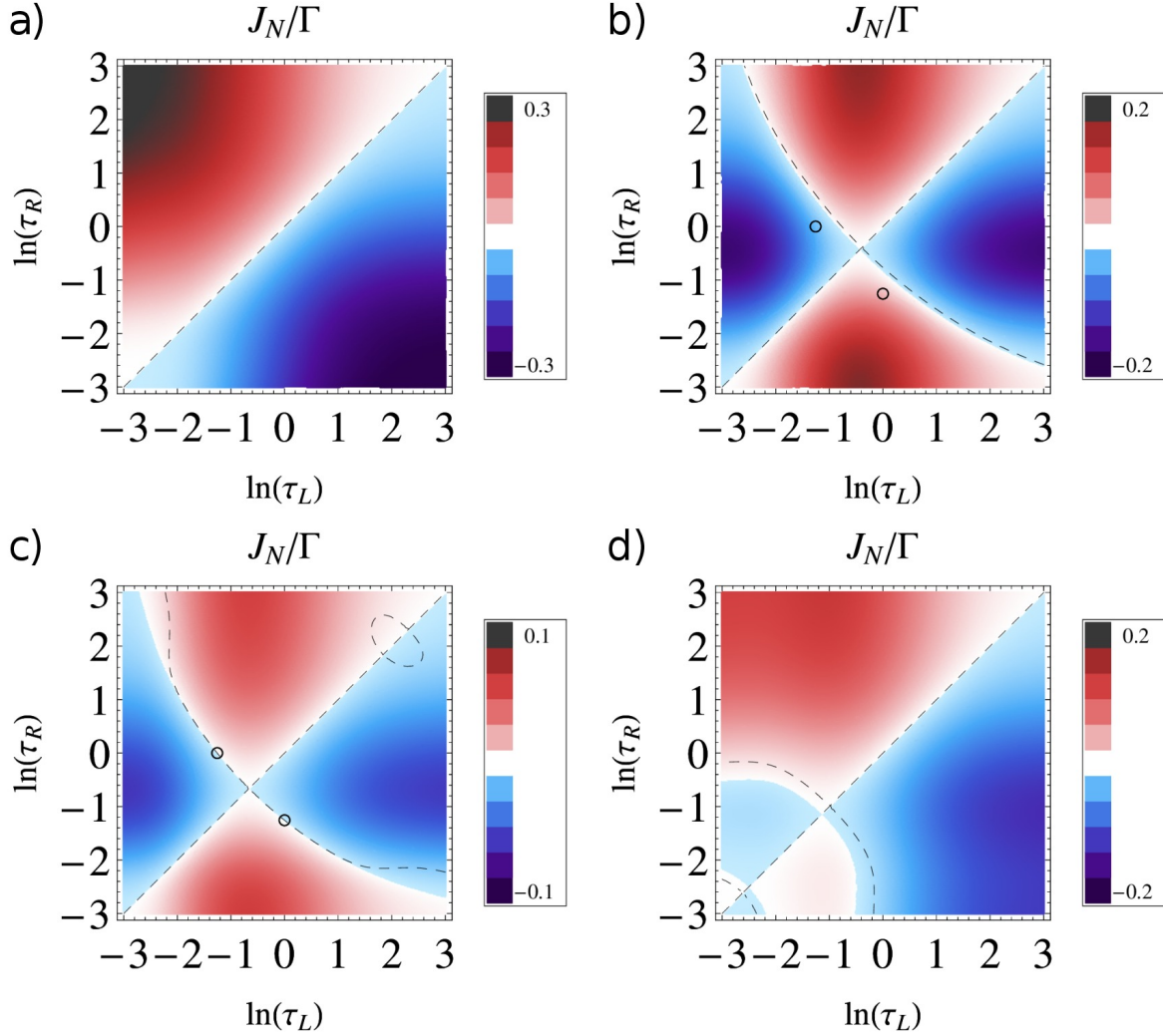


Figure 4.6: Logarithmic plot of the steady-state particle current through the fermionic system with different transition frequencies, versus the dimensionless temperatures $\tau_\alpha = T_\alpha/T_F$ of the reservoirs at fixed density. In the plots, we set $\varepsilon = 0.7E_F$ (a), $\varepsilon = 1.5E_F$ (b) and $\varepsilon = 1.2E_F$ (d) and use the same tunneling amplitude $g = 0.2E_F$. In plot (c), we use $\varepsilon = 11.3E_F$ and set the tunneling amplitude to $g = 10E_F$, such that the current can approximately be described by the single-level approximation from Eq. (4.60). For all plots the rates are set to $\Gamma_L = \Gamma_R = \Gamma$. The circles in the plots (b) and (c) correspond to the set of temperatures marked in the right panel of Fig. 4.3. The dashed curves indicate a vanishing of the corresponding energy current J_E .

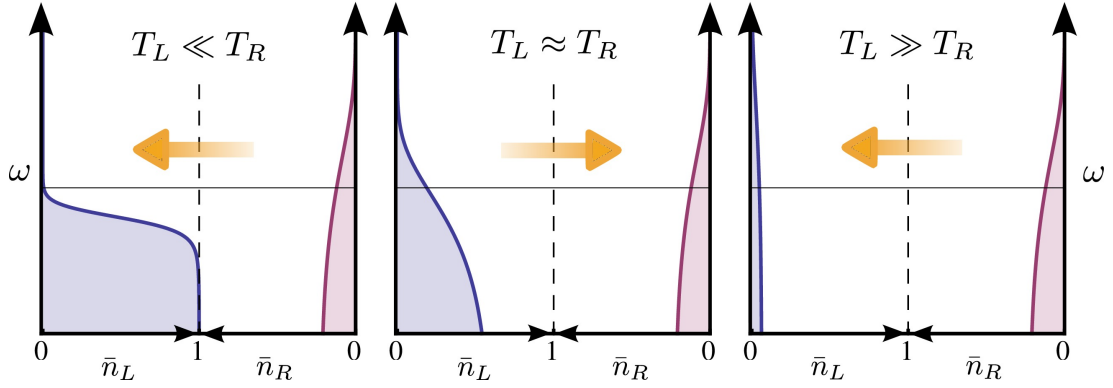


Figure 4.7: Sketch of the Fermi statistics \bar{n}_α in dependence of the frequency ω for different reservoir temperature configurations at constant, equal particle density. In all panels the temperature of the right reservoir T_R is fixed to T_F . The temperature of the left reservoir T_L increases from left to right. We show an explicit fixed transition energy of the system (thin, solid line) and indicates the maximum occupation in each lead (dashed line). The arrow inset (orange) reveals the direction of the particle flow according to the single-frequency limit result from Eq. (4.60).

Away from equilibrium, we find that the particle current between reservoirs with fixed mean particle density from Eq. (4.60), only vanishes if the mean occupation of a specific transition energy in the reservoirs takes on the same value for different temperatures. Comparing with the result presented in Fig. 4.3 we can immediately deduce that this condition can only be satisfied for transition frequencies above the Fermi energy. In this case one always finds a set of two different temperatures for the left and right reservoir where the current vanishes. As an example, we indicate such a set of temperatures in the right panel of Fig. 4.3 (circles) and show the corresponding points in the current plots in panel (b) and (c) of Fig. 4.6.

In panel (c), we chose the dot energy ε and the tunneling amplitude g in such a way that the transition energy ω_+ is shifted to high energies compared to ω_- . Thus, the corresponding particle current can be approximately described by the single-level limit given in Eq. (4.60). Comparing the currents plotted in the panels (b) and (c) in Fig. 4.6, we see that for a system with two transition frequencies (b) the line of vanishing particle current is shifted to higher temperatures compared to the effective single-level result from panel (c). This effect results from the additional transport channel which modifies the condition for a vanishing particle current. In fact, depending on the number and values of the transition frequencies in the system there can also be more lines where the particle current vanishes as indicated in panel (d)).

Finally, we note that the energy current J_E in general vanishes (dashed lines) for different parameters than the particle current J_N . Thus, we can observe a finite

energy current even for a vanishing particle current in a fermionic system with two transition frequencies. Moreover, in the upper right corner of panel (c), we even find a regime for high temperatures where the energy current flows against the particle current.

4.2.4 Linear transport coefficients

In this section, we calculate the linear transport coefficients for the fermionic transport setup with a temperature and particle density dependent chemical potential using the Onsager equations from Sec. 2.14.2. For reasons of brevity, we continue to use the wide-band limit with energy independent rates $\Gamma_\alpha(\omega) = \Gamma_\alpha$.

Using the results for the steady-state particle and energy currents from Eq. (4.57) and Eq. (4.58) and the derivative of the chemical potential with respect to temperature from Eq. (4.18), we can construct the generalized heat current \tilde{J}_Q according to Eq. (2.144). Linearizing the generalized heat current \tilde{J}_Q and the particle current J_N with respect to their affinities Δ_β and $\frac{\partial \mu}{\partial n} \Delta_n$, yields the corresponding Onsager matrix with the kinetic coefficients

$$\tilde{L}_{11} = \frac{\Gamma_L \Gamma_R}{\Gamma_L + \Gamma_R} \frac{[1 - \bar{n}(\omega_-)][1 - \bar{n}(\omega_+)]}{2[1 - \bar{n}(\omega_-)\bar{n}(\omega_+)]} \sum_{i \in \{+, -\}} \bar{n}(\omega_i) \left(\mu - T \frac{\partial \mu}{\partial T} - \omega_i \right)^2 \geq 0, \quad (4.64)$$

$$\tilde{L}_{12} = \tilde{L}_{21} = \frac{\Gamma_L \Gamma_R}{\Gamma_L + \Gamma_R} \frac{[1 - \bar{n}(\omega_-)][1 - \bar{n}(\omega_+)]}{2[1 - \bar{n}(\omega_-)\bar{n}(\omega_+)]} \sum_{i \in \{+, -\}} \bar{n}(\omega_i) \left(\mu - T \frac{\partial \mu}{\partial T} - \omega_i \right), \quad (4.65)$$

$$\tilde{L}_{22} = \frac{\Gamma_L \Gamma_R}{\Gamma_L + \Gamma_R} \frac{[1 - \bar{n}(\omega_-)][1 - \bar{n}(\omega_+)]}{2[1 - \bar{n}(\omega_-)\bar{n}(\omega_+)]} [\bar{n}(\omega_-) + \bar{n}(\omega_+)] \geq 0, \quad (4.66)$$

and the determinant

$$\tilde{D} = \left\{ \frac{\Gamma_L \Gamma_R}{\Gamma_L + \Gamma_R} \frac{[1 - \bar{n}(\omega_-)][1 - \bar{n}(\omega_+)]}{2[1 - \bar{n}(\omega_-)\bar{n}(\omega_+)]} \right\}^2 \bar{n}(\omega_-) \bar{n}(\omega_+) (\omega_- - \omega_+)^2 \geq 0. \quad (4.67)$$

Here, we drop the bath index of the mean occupations since the kinetic coefficients are evaluated in equilibrium. We see that the diagonal elements are strictly positive whereas the sign of the off-diagonal elements depends on the transition frequencies, temperature and particle density. With these matrix elements, we can calculate the linear transport coefficients following the procedure outlined in Sec. 2.14.2.

Motivated by the results of the previous paragraph, we mostly focus on the analysis of the transport properties for three different system configurations. The first configuration corresponds to a system with transition energies below the Fermi energy of the reservoirs. The second configuration corresponds to a system with transition energies above the Fermi energy of the reservoirs and in the third configuration, we analyze a system whose lowest transition energy is exactly equal to the Fermi energy of the reservoirs.

4.2.4.1 Matter conductance

Using the coefficient \tilde{L}_{22} from Eq. (4.66), we can calculate the matter conductance $\tilde{\sigma}$ in the wide-band limit with the help of Eq. (2.151) which results in the equation

$$\tilde{\sigma} = \frac{\Gamma_L \Gamma_R}{\Gamma_L + \Gamma_R} \frac{[1 - \bar{n}(\omega_-)][1 - \bar{n}(\omega_+)] [\bar{n}(\omega_-) + \bar{n}(\omega_+)]}{2T [1 - \bar{n}(\omega_-) \bar{n}(\omega_+)]} \geq 0. \quad (4.68)$$

From the above equation, we can immediately read off the limit for a single transition frequency which is obtained as $\omega_+ \rightarrow \infty$, i.e., $\bar{n}(\omega_+) \rightarrow 0$. We find that the respective expression coincides with

$$\lim_{\omega_+ \rightarrow \infty} \tilde{\sigma} = \frac{\Gamma_L \Gamma_R}{\Gamma_L + \Gamma_R} \frac{\bar{n}(\omega_-) [1 - \bar{n}(\omega_-)]}{2T}. \quad (4.69)$$

This is the well-known Coulomb blockade conductance peak for a single resonant level [196] up to a pre-factor 1/2 which results from the limiting procedure. Similarly, in the limit $g \rightarrow 0$, i.e., for $\omega_- \rightarrow \omega_+$, the matter conductance approaches the limiting value from Eq. (4.69). However, exactly at $g = 0$ the energies $\omega_- = \omega_+ = \varepsilon$ are degenerate and our BMS rate equation approach can not be applied. Furthermore, we note that the whole temperature and density dependence of the chemical potential enters only implicitly via the mean occupations of the energy levels in the reservoirs in compliance with Eq. (2.151).

In general, the fermionic matter conductance is proportional to the total number of particles $\bar{n}(\omega_-) + \bar{n}(\omega_+)$ that can participate in the transport. In addition, it is proportional to the number of available places in each energy level. This implies that free spaces in both energy levels are needed in order to have a finite particle transport through the system. From the discussion of the mean occupations in Sec. 4.1.1, we can immediately conclude that independent of the transition frequencies the matter conductance vanishes for high temperatures.

In the left panel of Fig. 4.8, we plot the matter conductance for a constant particle density as a function of the normalized temperature for different on-site energies ε and a constant tunneling amplitude g . For a configuration where at least one of the two transition energies lies below the Fermi energy of the reservoirs (dashed line), we observe a maximal conductance at a specific temperature which basically depends on the frequency ε . Decreasing the temperature below this characteristic temperature diminishes the conductance as the respective energy levels in the reservoirs become occupied. We observe a similar behavior for a configuration where both transition energies lie above the Fermi energy of the reservoirs (dot-dashed line). In this situation the conductance vanishes for decreasing temperature due to the fact that the energy levels in the reservoirs get exponentially depleted. Hence, the total number of particles available for transport is diminished.

Finally, we show the result for a configuration where the lower transition energy equals the Fermi energy of the reservoirs (solid line). Only in this case we observe a nonvanishing conductance as the temperature approaches 0. This is due to the fact

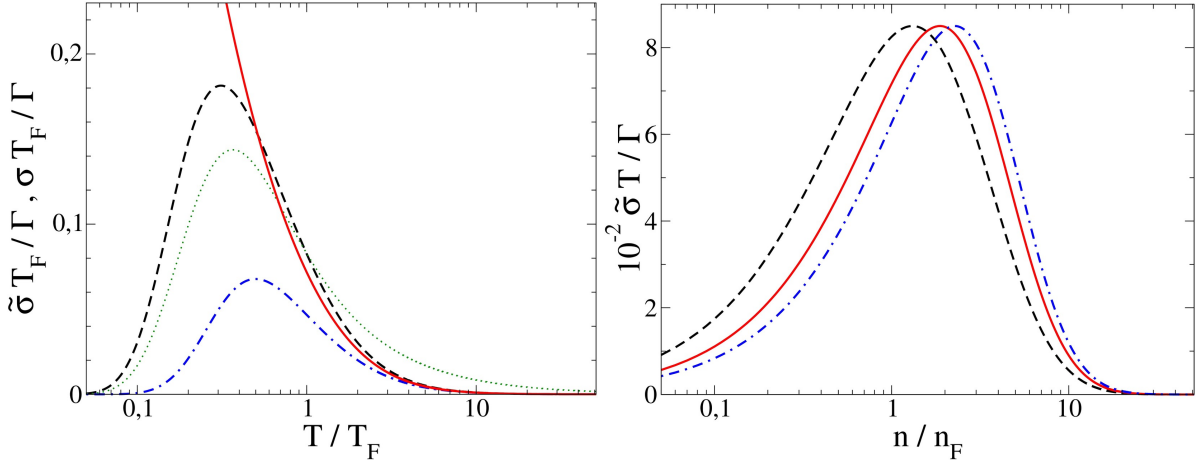


Figure 4.8: Plot of fermionic matter conductance $\tilde{\sigma}$ at a constant particle density (left) and at a constant temperature (right) versus the normalized temperature and particle density, respectively. In both plots we assume equal tunneling rates $\Gamma_L = \Gamma_R = \Gamma$. In the left panel, we use a constant coherent coupling strength of $g = 0.2E_F$ and the on-site energies $\varepsilon = 0.7E_F$ (dashed line), $\varepsilon = 2E_F$ (dot-dashed line) and $\varepsilon = 1.2E_F$ (solid line). In the right panel, we use a constant coherent coupling strength of $g = 0.2T$ and the on-site energies $\varepsilon = 0.7T$ (dashed line), $\varepsilon = 1.5T$ (dot-dashed line) and $\varepsilon = 1.2T$ (solid line). For the conductance σ with constant chemical potential, we use $\varepsilon = 1.2E_F$, $g = 0.2E_F$ and additionally set $\mu = 0.5E_F$ (thin, dotted line).

that the Fermi energy level in the reservoirs is at most half filled for vanishing temperature. Contrary, the other energy level is completely empty for vanishing temperature. Therefore, the corresponding matter conductance approaches for $T \ll T_F$ the value

$$\lim_{T \rightarrow 0} \tilde{\sigma}(\omega_- = E_F, \omega_+ > E_F) = \lim_{T \rightarrow 0} \frac{\Gamma}{16T}, \quad (4.70)$$

and particle transport is in principle possible. However, we observe that in this case the matter conductance $\tilde{\sigma}$ diverges like Γ/T which is obviously unphysical. We conjecture that this unphysical behavior stems from the break down of the Born-Markov-Secular master equation for $T \ll \Gamma$ [109].

As expected, in all three situations the matter conductance vanishes for increasing temperature due to the reduction of the occupation of the energy levels in the reservoirs in accordance with our findings presented in Fig. 4.3.

For comparison, we also plotted the conductance σ for a constant chemical potential (dotted line). In this situation, we find qualitatively the same behavior as for the temperature dependent matter conductance. For low temperatures the respective energy levels in the reservoirs are depleted and, hence, the conductance

vanishes. Contrary for high temperatures the energy levels are equally filled which leads to a vanishing net current. Thus, the modified matter conductance $\tilde{\sigma}$ basically follows σ . However, the high temperature behavior is changed due to the temperature dependence of the chemical potential.

In the right panel of Fig. 4.8, we plot the matter conductance for a constant temperature as a function of the normalized density for different on-site energies ε and a constant tunneling amplitude g . Independent of the transition frequencies the matter conductance vanishes for high densities since increasing the density increase the occupation of each energy level. Analogously, independent of the transition frequencies the conductance has to vanish as the temperature approaches zero since all energy levels are depleted at sufficiently low densities. In between there is a characteristic density where the matter conductance is highest. This characteristic density increases with increasing transition energy. Note, that we can not observe any divergences in this plot since the temperature is used to scale the energy of the transition frequencies and the chemical potential.

4.2.4.2 Heat conductance

Using the results from Eq. (4.66) and Eq. (4.67) in the definition in Eq. (2.152), we find that the heat conductance in the wide-band limit is given by

$$\tilde{\kappa} = \frac{\bar{n}(\omega_-) \bar{n}(\omega_+) (\omega_- - \omega_+)^2}{T [\bar{n}(\omega_-) + \bar{n}(\omega_+)]^2} \tilde{\sigma} \geq 0. \quad (4.71)$$

This expression has no explicit dependence on the chemical potential and, thus, formally corresponds to the thermal conductance for an independent chemical potential as shown in Sec. 2.14.2. Furthermore, we immediately see that the above equation obeys the Wiedemann-Franz law, i.e., $\tilde{\kappa} = T \tilde{L} \tilde{\sigma}$, with the dimensionless Lorenz number

$$\tilde{L} = \frac{\bar{n}(\omega_-) \bar{n}(\omega_+) (\omega_- - \omega_+)^2}{T^2 [\bar{n}(\omega_-) + \bar{n}(\omega_+)]^2} = \frac{4g^2}{T^2} \frac{\bar{n}(\omega_-) \bar{n}(\omega_+)}{[\bar{n}(\omega_-) + \bar{n}(\omega_+)]^2} \geq 0. \quad (4.72)$$

In the limit of a single transition frequency, i.e., for $\omega_+ \rightarrow \infty$ or $\omega_+ \rightarrow \omega_-$, the heat conductance $\tilde{\kappa}$ vanishes trivially because there is no pure heat flow through a single level without particle flow. Due to the proportionality from the Wiedemann-Franz law, we find that the heat conductance has similar properties as the matter conductance discussed within the previous paragraph concerning the dependence on the energy level occupations in the reservoirs. However, the heat conductance additionally is proportional to the occupation of each energy level, respectively. That implies that the thermal conductance vanishes as soon as one energy level is completely filled or empty, which is in contrast to the matter conductance where one can observe a finite transport even if one of the energy levels is completely empty.

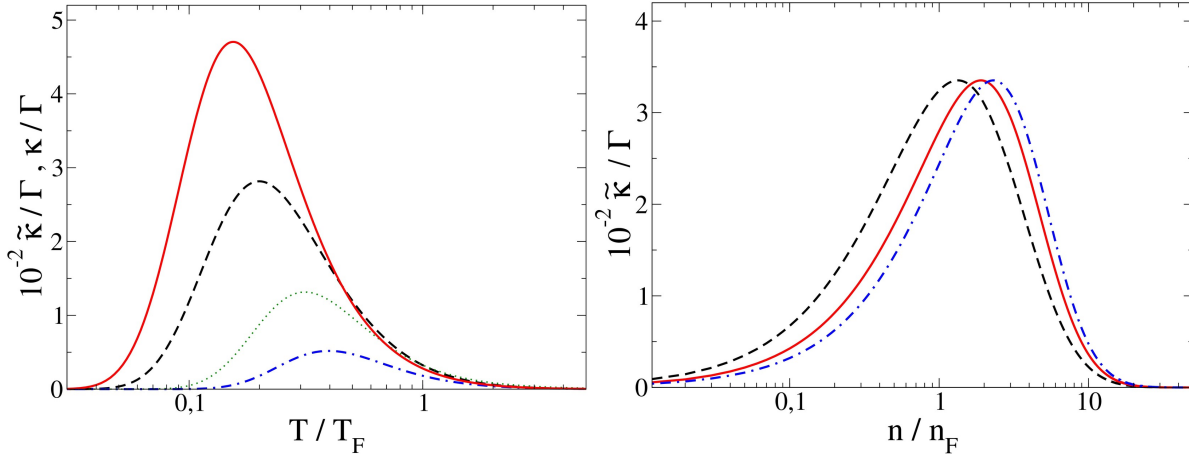


Figure 4.9: Plot of fermionic heat conductance $\tilde{\kappa}$ at a constant particle density (left) and at a constant temperature (right) versus the normalized temperature and particle density, respectively. In both plots we use equal tunnel rates $\Gamma_L = \Gamma_R = \Gamma$. In the left panel, we use a constant coherent coupling strength of $g = 0.2E_F$ and the on-site energies $\varepsilon = 0.7E_F$ (dashed line), $\varepsilon = 2E_F$ (dot-dashed line) and $\varepsilon = 1.2E_F$ (solid line). In the right panel, we use a constant coherent coupling strength of $g = 0.2T$ and the on-site energies $\varepsilon = 0.7T$ (dashed line), $\varepsilon = 1.5T$ (dot-dashed line) and $\varepsilon = 1.2T$ (solid line). For the heat conductance κ with constant chemical potential, we use $\varepsilon = 1.2E_F$, $g = 0.2E_F$ and additionally set $\mu = 0.5E_F$ (thin, dotted line).

This behavior emphasizes the fact that both transport channels are needed in order to transport a finite amount of heat without transporting particles.

In Fig. 4.9, we plot the thermal conductance at constant particle density versus the normalized temperature (left) and at constant temperature versus the normalized particle density (right) for different on-site energies and different tunneling amplitudes according to Eq. (4.71). For all considered configurations, we observe qualitatively a similar behavior as for the matter conductance. The heat transport is maximal at a characteristic temperature and density. This maximum is shifted to higher densities with increasing transition energies. For low densities and high temperatures the thermal conductance vanishes as the reservoir energy levels become less occupied. For high densities the heat conductance vanishes because the transition energies in both reservoirs become maximally occupied and the matter conductance vanishes. Analogously, for low temperatures the energy levels become either completely filled or empty. In both cases the matter conductance and hence the thermal conductance vanish. Therefore, we see that the thermal conductance basically follows the matter conductance.

The only qualitative difference occurs for the configuration where the lowest energy level equals the Fermi energy and the matter conductance diverges for low tem-

perature. This divergence does not occur for the heat conductance since it is also proportional to the occupation of the higher energy level which is depleted as the temperature approaches zero.

Finally, we want to point out that the heat conductance $\tilde{\kappa}$ as well as the matter conductance $\tilde{\sigma}$ are always positive. This results from the fact that the Onsager matrix is positive definite. Consequently, within the linear response theory, we can not resolve the negative conductances observed in the nonequilibrium currents in Fig. 4.6.

4.2.4.3 Thermopower

Besides analyzing the typical transport quantities measurable in an experiment like the currents and their associated conductances, another interesting application of transport setups is their potential use as power converters. Therefore, within this paragraph, we investigate the possibility to use the proposed setup in order to convert density differences into a thermal bias at vanishing matter current. Hence, we determine the analogue to the thermopower as defined in Eq. (2.155). Using the results from Eq. (4.65) and Eq. (4.66), we find for our setup the expression

$$\tilde{\Sigma} = \frac{1}{T} \frac{\bar{n}(\omega_-) \phi_- + \bar{n}(\omega_+) \phi_+}{\bar{n}(\omega_-) + \bar{n}(\omega_+)}, \quad (4.73)$$

where we introduced the abbreviations

$$\phi_i = \mu - T \frac{\partial \mu}{\partial T} - \omega_i = \phi_i(T, n), \quad (4.74)$$

which have the physical dimension of an energy and implicitly depend on temperature and particle density. We observe that the analog of the Peltier coefficient $\tilde{\Pi} = T\tilde{\Sigma}$ corresponding to Eq. (4.73) assumes the form of a weighted arithmetic mean of the energies ϕ_i . Here, the weights are given by the occupation of the energy levels in the reservoirs. From an energy balance consideration, we notice that the expressions ϕ_i defined in Eq. (4.74) describe the amount of energy that one particle traveling through a transport system with only a single transition energy ω_i takes from one reservoir to the other. The influence of the temperature dependent chemical potential explicitly enters this transported energy in form of the term $T\partial\mu/\partial T$. It basically describes the potential difference between the reservoirs that is induced by the applied temperature bias which the particle has to compensate in order to travel through the setup. Thus, we can formally recover the result for the conventional thermopower with an independent chemical potential by setting $\partial\mu/\partial T = 0$, since here no additional compensation is needed.

Contrary to the analog of the Peltier coefficient which considers the absolute averaged energy transported through the system, the Seebeck coefficient sets the averaged energy in relation to the temperature. Looking at the behavior of the energies

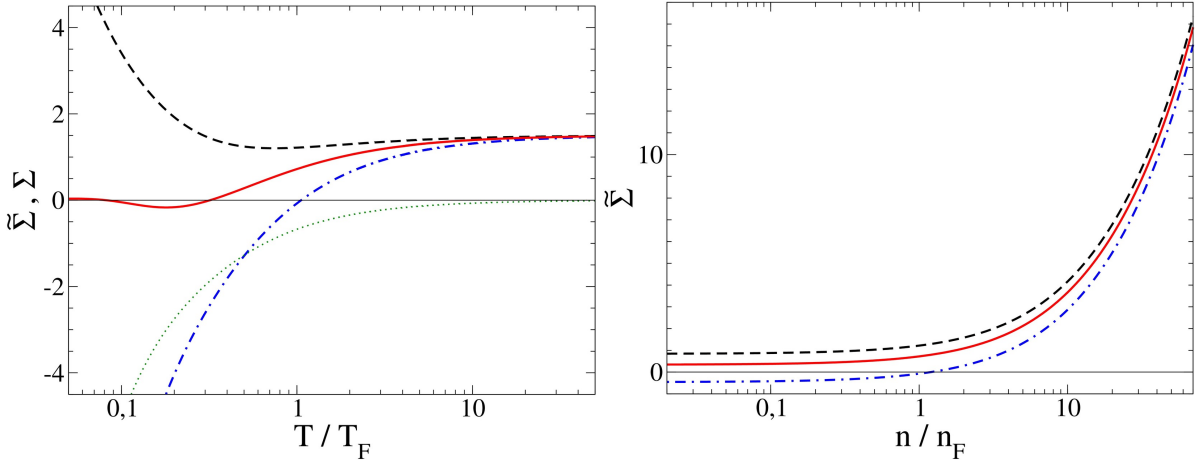


Figure 4.10: Plot of the density- and temperature-dependent fermionic thermopower $\tilde{\Sigma}$ and the conventional thermopower Σ versus the normalized temperature (left), and the normalized density (right), for an ideal Fermi gas. In the left panel, we use a constant coherent coupling strength of $g = 0.2E_F$ and the on-site energies $\varepsilon = 0.7E_F$ (dashed line), $\varepsilon = 2E_F$ (dot-dashed line) and $\varepsilon = 1.2E_F$ (solid line). In the right panel, we use a constant coherent coupling strength of $g = 0.2T$ and the on-site energies $\varepsilon = 0.7T$ (dashed line), $\varepsilon = 2T$ (dot-dashed line) and $\varepsilon = 1.2T$ (solid line). For the thermopower Σ with constant chemical potential, we use $\varepsilon = 1.2E_F$, $g = 0.2E_F$ and additionally set $\mu = 0.5E_F$ (thin, dotted line).

ϕ_i at high temperatures and low densities, we find that independent of the transition frequency they increase linearly with the temperature according to

$$\phi_i(T \gg T_F) = \phi_i(n \ll n_F) \approx \frac{3}{2}T - \omega_i. \quad (4.75)$$

We conclude that for high temperatures the analog to the Peltier coefficient increases linearly according to Eq. (4.75) whereas the analog to the thermopower $\tilde{\Sigma}$ assumes the constant value $3/2$. Contrary, in the limit of a vanishing temperature, we find

$$\phi_i(T \approx 0) \approx E_F - \omega_i, \quad (4.76)$$

i.e., the influence of the temperature dependence of the chemical potential ceases to play a role. This implies that the analog to the Peltier coefficient assumes a constant value for vanishing temperature, whose sign depends on the differences from Eq. (4.76).

In the left panel of Fig. 4.10, we plot the temperature dependence of the modified thermopower $\tilde{\Sigma}$ for different transition energies in the case of Fermi reservoirs

according to Eq. (4.73). When the temperature decreases, we observe different behavior for the modified thermopower depending on the transport system. If the lower transition energy is below the Fermi energy the modified thermopower remains positive for all temperatures. As the temperature approaches zero the analog to the Peltier coefficient approaches a constant positive value and, thus, the modified thermopower diverges like $1/T$. If the transition energies are above the Fermi energy, we observe a similar behavior but the coefficient becomes negative since below some critical temperature the transition frequencies exceed the chemical potentials. Only for the case when the lower transition energy equals the Fermi energy the average energy and hence the modified thermopower vanishes at $T = 0$.

As discussed before, for high temperatures the analog to the thermopower is dominated by the classical thermal energy contribution of $3/2k_B T$ per particle, leading to a constant positive value of the thermopower for high temperature, independent of the respective transition energies. This behavior can not be predicted if the chemical potential is treated as an independent parameter. In this conventional approach the thermopower vanishes for high temperatures independent of the transition frequencies (dotted line). Furthermore, the conventional thermopower never changes its sign as a function of the temperature. In this situation the sign is fixed by the choice of the constant chemical potential.

Finally, in the right panel of Fig. 4.10, we plot the dependence of the analog to the thermopower on the particle density in the reservoirs. We observe that in the limit of low densities the thermopower assumes constant values that depend on the transition frequencies according to

$$\lim_{n \rightarrow 0} \tilde{\Sigma} = \frac{1}{T} \left[\frac{3}{2} T - \omega_- \left(1 - \frac{1}{1 + e^{\frac{\omega_+ - \omega_-}{T}}} \right) - \omega_+ \left(\frac{1}{1 + e^{\frac{\omega_+ - \omega_-}{T}}} \right) \right]. \quad (4.77)$$

We find that for a small difference $\omega_+ - \omega_-$ the sign of the thermopower in the low density limit mainly depends on the dot energy ε . Approximately, if we assume that $[1 + e^{(\omega_+ - \omega_-)/T}]^{-1} \approx 1/2$, we find that the thermopower in the limit of small particle densities reads as

$$\lim_{n \rightarrow 0} \tilde{\Sigma} \approx \frac{3}{2} - \frac{\varepsilon}{T}, \quad \text{for} \quad \frac{2g}{T} \ll 1. \quad (4.78)$$

Hence, if the energy ε is smaller than $3/2T$ the thermopower assumes positive values whereas for higher frequencies it assumes negative values. This effect can be seen in the right panel of Fig. 4.10.

In the limit of very high densities the energies ϕ_i scale like

$$\phi_i(n \gg n_F) \sim n^{2/3}, \quad (4.79)$$

and, in consequence, the analog to the thermopower increases exponentially with the density. Both, the limits in Eq. (4.77) and in Eq. (4.79) imply that for high transition frequencies the modified thermopower in general changes its sign at a characteristic particle density.

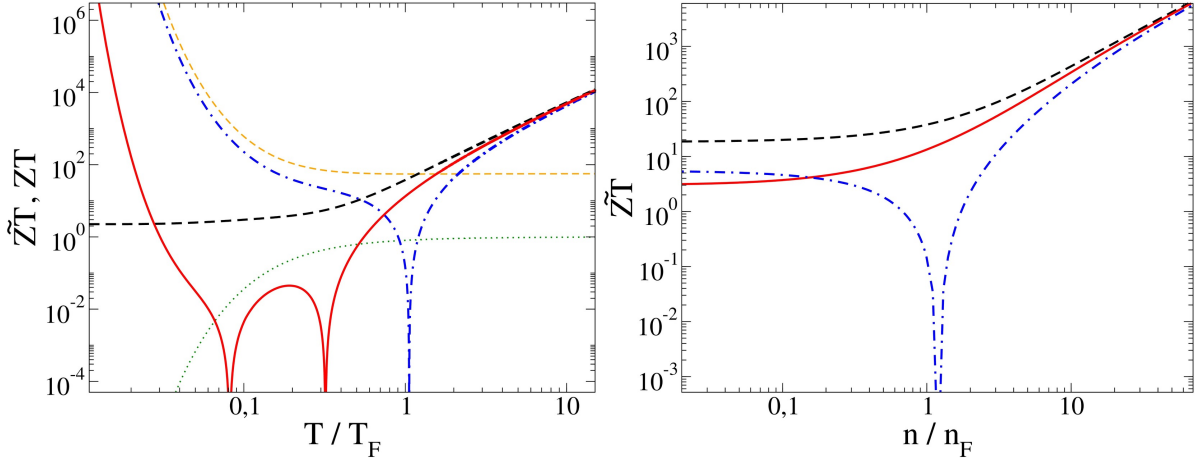


Figure 4.11: Plot of the fermionic figure-of-merit for dependent and constant chemical potential versus the normalized temperature (left) and versus the normalized particle density (right) for an ideal Fermi gas. In the left panel, we use a constant coherent coupling strength of $g = 0.2E_F$ and the on-site energies $\varepsilon = 0.7E_F$ (dashed line), $\varepsilon = 2E_F$ (dot-dashed line) and $\varepsilon = 1.2E_F$ (solid line). In the right panel, we use a constant coherent coupling strength of $g = 0.2T$ and the on-site energies $\varepsilon = 0.7T$ (dashed line), $\varepsilon = 2T$ (dot-dashed line) and $\varepsilon = 1.2T$ (solid line). For the figure-of-merit ZT with constant chemical potential, we use $\varepsilon = 1.2E_F$, $g = 0.2E_F$ and additionally set $\mu = 0.5E_F$ (thin, dotted line) and $\mu = -0.5E_F$ (thin, dashed line).

From the above analysis, we find that with the proposed fermionic transport setup the conversion of a density bias into a thermal bias is possible. However, we do not yet know how efficient this process can be. This question is addressed within the next subsection.

4.2.4.4 Thermodynamic performance

In order to investigate the efficiency of the conversion of a density bias into a thermal bias, we analyze the figure-of-merit for the thermodynamic device. This coefficient is defined in Eq. (2.157). Using the coefficients from Eq. (4.73) and Eq. (4.72), the figure-of-merit for the considered fermionic setup reads as

$$\tilde{Z}T = \frac{[\bar{n}(\omega_-)\phi_- + \bar{n}(\omega_+)\phi_+]^2}{\bar{n}(\omega_-)\bar{n}(\omega_+)(\omega_- - \omega_+)^2} \geq 0. \quad (4.80)$$

In the left panel of Fig. 4.11, we plot the linear response figure-of-merit in dependence of the normalized reservoir temperature for different on-site energies. We find that the figure-of-merit increases exponentially for high temperatures independent of the transition frequencies which is caused by the behavior outlined in

Eq. (4.75). In contrast, for a constant chemical potential the figure-of-merit approaches a constant value for high temperatures. Additionally, we see that there are specific temperatures where the figure-of-merit vanishes. These are the temperatures for which the linear response particle current vanishes and, hence, no power can be extracted. In accordance with Fig. 4.6, we find that the figure-of-merit vanishes at a single temperature when both frequencies lie above the Fermi energy, at two temperatures if the lower frequency equals the Fermi energy and never if both frequencies lie below the Fermi energy.

If the temperature approaches zero, we observe that the figure-of-merit increases again except for the situation where the transition frequencies lie below the Fermi energy of the reservoir (dashed line). In this case the figure-of-merit assumes a finite value

$$\lim_{T \rightarrow 0} \tilde{Z}T = \left(\frac{2E_F - \omega_- - \omega_+}{\omega_- - \omega_+} \right)^2 = \left(\frac{E_F - \varepsilon}{g} \right)^2, \text{ for } \omega_-, \omega_+ < E_F. \quad (4.81)$$

This is again caused by the fact that the relevant energy levels in the reservoirs are occupied for low temperatures.

In the right panel of Fig. 4.11, we additionally plot the figure-of-merit for a constant temperature versus the dimensionless particle density. For high densities we also observe an exponential increase independent of the transition frequencies, that is related to Eq. (4.79). In the limit of small densities, we observe that the figure-of-merit approaches a finite positive value which depends on the transition frequencies according to

$$\lim_{n \rightarrow 0} \tilde{Z}T = \left[\frac{e^{-\frac{\omega_- - \omega_+}{2T}} \left(\frac{3}{2}T - \omega_- \right) + e^{-\frac{\omega_- - \omega_+}{2T}} \left(\frac{3}{2}T - \omega_+ \right)}{\omega_+ - \omega_-} \right]^2. \quad (4.82)$$

In both panels of Fig. 4.11, we see that the conversion of a thermal bias into a potential bias is very efficient as high figure-of-merits can be reached for low and high temperatures and densities. Usually in experiments figure-of-merits of about $ZT \sim 2$ and higher are considered as efficient.

To quantitatively verify this effect, we additionally look out for the efficiency at maximum power [148, 197–199]. Inserting Eqs. (4.64)-(4.66) into the definition from Eq. (2.158) yields

$$\tilde{\eta} = \frac{\eta_C}{2} \left[\frac{\bar{n}(\omega_-)\phi_1 + \bar{n}(\omega_+)\phi_2}{\bar{n}(\omega_-) + \bar{n}(\omega_+)} \right] \left(2 \frac{\bar{n}(\omega_-)\phi_1^2 + \bar{n}(\omega_+)\phi_2^2}{\bar{n}(\omega_-)\phi_1 + \bar{n}(\omega_+)\phi_2} - \sqrt{\frac{\bar{n}(\omega_-)\phi_1^2 + \bar{n}(\omega_+)\phi_2^2}{\bar{n}(\omega_-) + \bar{n}(\omega_+)}} \right)^{-1}. \quad (4.83)$$

Some results for the efficiency at maximum power are plotted in Fig. 4.12 for the same parameters as the figure-of-merit in Fig. 4.11. We observe similar behavior for both performance measures. However, we can now confirm that for high temperatures and densities the thermocouple generates power very efficient independent of

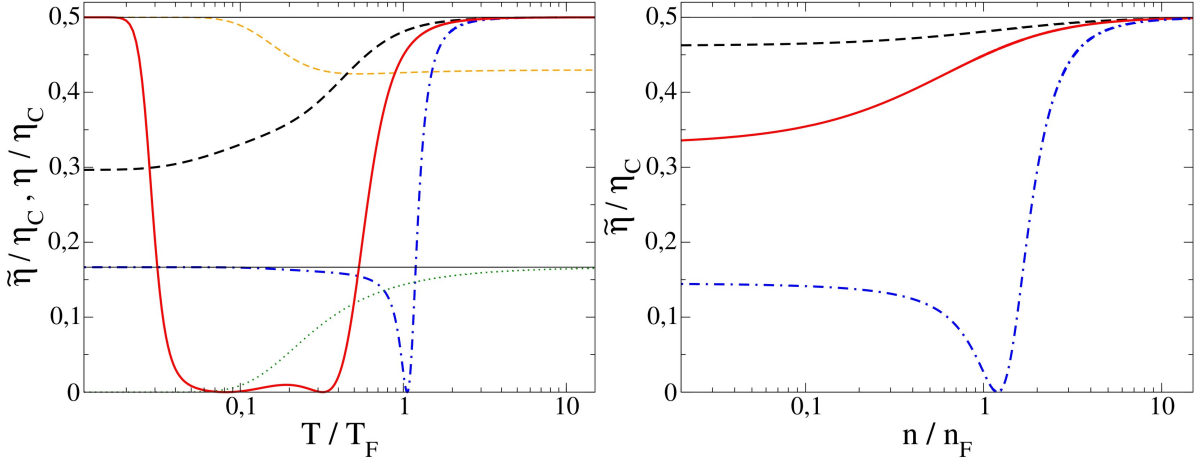


Figure 4.12: Plot of the fermionic efficiency at maximum power for dependent and constant chemical potential versus the normalized temperature (left) and versus the normalized particle density (right) for an ideal Fermi gas. In the left panel, we use a constant coherent coupling strength of $g = 0.2E_F$ and the on-site energies $\varepsilon = 0.7E_F$ (dashed line), $\varepsilon = 2E_F$ (dot-dashed line) and $\varepsilon = 1.2E_F$ (solid line). In the right panel, we use a constant coherent coupling strength of $g = 0.2T$ and the on-site energies $\varepsilon = 0.7T$ (dashed line), $\varepsilon = 2T$ (dot-dashed line) and $\varepsilon = 1.2T$ (solid line). For the efficiency at maximum power η with constant chemical potential, we use $\varepsilon = 1.2E_F$, $g = 0.2E_F$ and additionally set $\mu = 0.5E_F$ (thin, dotted line) and $\mu = -0.5E_F$ (thin, dashed line). The thin, solid lines shown in both panels correspond to the limit values $\eta_C/2$ and $\eta_C/6$.

the transition frequencies. This situation changes for small temperatures where the maximum efficiency depends on the transition frequencies. In this limit, we find that the efficiency at maximum power becomes

$$\lim_{T \rightarrow 0} \tilde{\eta} = \begin{cases} \frac{1}{6}\eta_C & , \text{ for } \omega_-, \omega_+ > E_F \\ \frac{1}{2}\eta_C & , \text{ for } \omega_- \leq E_F, \omega_+ > E_F \\ \frac{\eta_C}{2} \left(\frac{(E_F - \omega_-)^2 + (E_F - \omega_+)^2}{(E_F - \varepsilon)^2} - \sqrt{\frac{(E_F - \omega_-)^2 + (E_F - \omega_+)^2}{2(E_F - \varepsilon)^2}} \right)^{-1} & , \text{ for } \omega_-, \omega_+ < E_F \end{cases} \quad (4.84)$$

For the configuration where the lowest transition frequency equals the Fermi energy, we observe an increase of the efficiency for very small temperatures up to the maximum value of $\tilde{\eta}_{\max} = \eta_C/2$, where $\eta_C = \Delta_T/T$ is the Carnot efficiency. This is the optimum efficiency in linear response theory [137]. For the configuration where both transition frequencies lie above the Fermi energy, we observe that the efficiency at maximum power assumes a constant value of $\eta_C/6$ indicating a partial decoupling of particle and heat transport due to the depletion of the respective

energy levels in the reservoirs.

We also observe that the efficiency at maximum power assumes constant values in the limit of vanishing density that depend on the monitored transition frequencies according to

$$\lim_{n \rightarrow 0} \tilde{\eta} = \frac{4b^2\eta_C}{(a-b)^2 - b^2} \geq 0, \quad (4.85)$$

where we defined the abbreviations

$$\begin{aligned} a &= \frac{2}{T} \sqrt{\left(e^{\frac{\omega_-}{T}} + e^{\frac{\omega_+}{T}} \right) \left[e^{\frac{\omega_+}{T}} \left(\frac{3}{2}T - \omega_- \right)^2 + e^{\frac{\omega_-}{T}} \left(\frac{3}{2}T - \omega_+ \right)^2 \right]}, \\ b &= \frac{1}{2T} \left[e^{\frac{\omega_+}{T}} \left(\frac{3}{2}T - \omega_- \right) + e^{\frac{\omega_-}{T}} \left(\frac{3}{2}T - \omega_+ \right) \right]. \end{aligned} \quad (4.86)$$

Finally, we plot the efficiency at maximum power for constant chemical potentials in the left panel of Fig. 4.12 (thin lines). Here, we observe that this conventional approach underestimates the efficiency especially in the limit of high temperatures because the correct dependence of the chemical potential on the temperature is not taken into account.

4.3 Transport with ultracold bosons

Having analyzed the effect of a temperature and density dependent chemical potential in a fermionic transport setup in Sec. 4.2, we now focus on a transport setup involving bosonic reservoirs within the present section. As explained in Sec. 4.1, these bosonic reservoirs can undergo a quantum phase transition from a normal gas to a Bose-Einstein condensate. Therefore, contrary to the fermionic transport setup, here, we expect that this critical behavior of the reservoirs leads to characteristic signatures in the transport properties.

4.3.1 Transport system

We analyze the transport characteristics of a bosonic transport system as shown in Fig. 4.13. The bosonic transport system is described by the Hamiltonian

$$\hat{\mathcal{H}}_S^{\text{bose}} = \frac{U}{2} \hat{a}^\dagger \hat{a} (\hat{a}^\dagger \hat{a} - 1) + \Omega \hat{a}^\dagger \hat{a}. \quad (4.87)$$

Here, the operators \hat{a}^\dagger and \hat{a} which obey the commutator relations

$$[\hat{a}, \hat{a}^\dagger] = 1, [\hat{a}, \hat{a}] = [\hat{a}^\dagger, \hat{a}^\dagger] = 0, \quad (4.88)$$

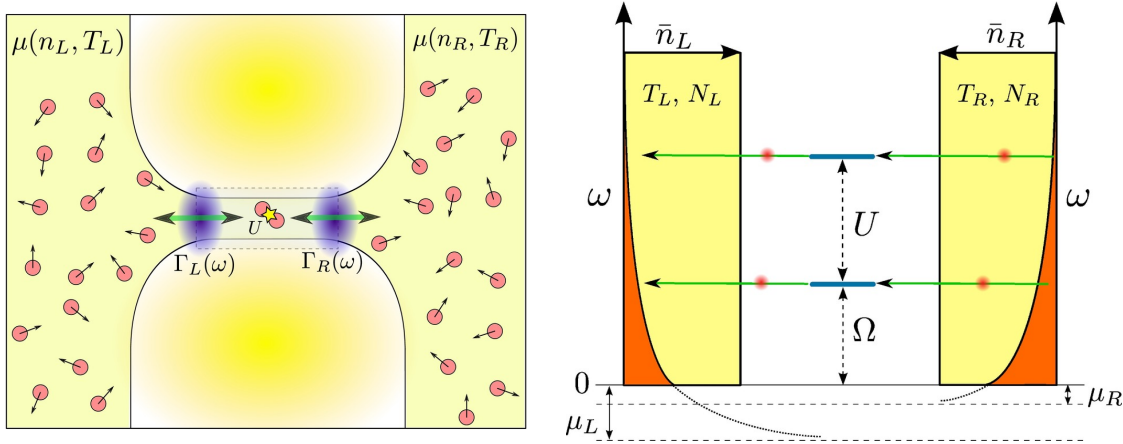


Figure 4.13: Left: Sketch of a bosonic transport setup. External lasers (blue, yellow) define the few-level quantum system (dashed box) between two clouds of ultracold atoms. Right: Sketch of the corresponding energy representation in the system eigenbasis. The reservoirs are characterized by their respective temperature T_ν and particle density n_ν , which define the chemical potentials μ_ν . The particle exchange between reservoirs and system is proportional to the rates $\Gamma_\nu(\omega)$. Each particle adds a potential energy Ω . If two particles are present in the system they interact with strength U . The two lowest transitions in the system are given by $\omega_1 = \Omega$ and $\omega_2 = U + \Omega$.

create and annihilate a Boson in the system, respectively. If more than one Boson is present in the system, they interact via a two-body interaction with interaction strength U . Note, that this Hamiltonian corresponds to a single lattice site of a Bose-Hubbard lattice [73, 200].

Obviously, the system Hamiltonian in Eq. (4.87) is diagonal in the local bosonic Fock basis, i.e.,

$$\hat{\mathcal{H}}_S^{\text{bose}} |n\rangle = E_n |n\rangle, \quad (4.89)$$

with corresponding energy eigenvalues

$$E_n = \frac{U}{2}n(n-1) + \Omega n. \quad (4.90)$$

Due to the particle interaction with interaction strength U , the above energy spectrum is nonlinear. Therefore, the suggested system generates, in principle, infinitely many nonequivalent transport channels.

Analogously to the transport setups discussed so far, the bosonic system is tunnel-coupled to the reservoirs via an interaction Hamiltonian that, due to the commuta-

tion relation $[\hat{a}, \hat{b}_{\alpha,k}^\dagger] = 0$, reads as

$$\hat{\mathcal{H}}_I = \sum_{\alpha,k} \left(t_{\alpha,k} \hat{a} \hat{b}_{\alpha,k}^\dagger + t_{\alpha,k}^* \hat{a}^\dagger \hat{b}_{\alpha,k} \right). \quad (4.91)$$

Here, the tunneling amplitude of a Boson hopping from the k -mode in reservoir α into the system or vice versa is proportional to $t_{\alpha,k}^*$ and $t_{\alpha,k}$, respectively. We can split this interaction Hamiltonian into a sum over direct products of system- and bath operators only, according to Eq. (2.9). We find the decomposition

$$\hat{\mathcal{H}}_I = \sum_{i \in \{1,2\}} \hat{A}_i \otimes \hat{B}_i, \quad (4.92)$$

where we introduce the bosonic system- and bath operators

$$\begin{aligned} \hat{A}_1 &= \hat{a}, & \hat{B}_1 &= \sum_{\alpha \in \{L,R\}} \sum_{k=0}^{\infty} t_{\alpha,k} \hat{b}_{\alpha,k}^\dagger, \\ \hat{A}_2 &= \hat{a}^\dagger, & \hat{B}_2 &= \sum_{\alpha \in \{L,R\}} \sum_{k=0}^{\infty} t_{\alpha,k}^* \hat{b}_{\alpha,k}. \end{aligned} \quad (4.93)$$

We assume that each reservoir is in its respective thermal equilibrium state as defined in Eq. (4.37). Now, the partition function of an ideal Bose gas enters this thermal state which can be calculated according to

$$\mathcal{Z}_\alpha = \text{Tr} \left\{ e^{-\beta_\alpha (\hat{\mathcal{H}}_\alpha - \mu_\alpha \hat{N}_\alpha)} \right\} = \prod_k \sum_{n_k=0}^{\infty} e^{-\beta_\alpha (\varepsilon_k^{(\alpha)} - \mu_\alpha) n_k} = \prod_k \frac{1}{1 - e^{-\beta_\alpha (\varepsilon_k - \mu_\alpha)}}. \quad (4.94)$$

Here, we assumed again that $\varepsilon_k^{(\alpha)} = \varepsilon_k$, i.e., that both reservoirs consist of the same type of particles with the same mass $m_\alpha = m$. We can use these bath properties to calculate the bath correlation functions according to Eq. (2.68). The only nonvanishing correlations are given by

$$C_{12}^{(\alpha)}(\tau) = \sum_k \bar{n}_\alpha(\varepsilon_k) |t_{\alpha,k}|^2 e^{i\varepsilon_k \tau} = \int_{-\infty}^{\infty} d\omega \rho^{(\alpha)}(\omega) \bar{n}_\alpha(\omega) e^{i\omega \tau}, \quad (4.95)$$

$$C_{21}^{(\alpha)}(\tau) = \sum_k [1 + \bar{n}_\alpha(\varepsilon_k)] |t_{\alpha,k}|^2 e^{-i\varepsilon_k \tau} = \int_{-\infty}^{\infty} d\omega \rho^{(\alpha)}(\omega) [1 + \bar{n}_\alpha(\omega)] e^{-i\omega \tau}, \quad (4.96)$$

where the mean occupation $\bar{n}_\alpha(\omega)$ for each bath is now given by the Bose-Einstein statistics defined as

$$\bar{n}_\alpha(\omega) = \frac{1}{e^{\beta_\alpha(\omega - \mu_\alpha)} - 1}, \quad (4.97)$$

in correspondence with Eq. (4.3). Additionally, in the above equations we used the density-of-states for each reservoir as defined in Eq. (4.42). Using these results, we can calculate the even Fourier transform bath correlation functions and obtain

$$\begin{aligned}\gamma_{12}^{(\alpha)}(-\omega) &= \Gamma_{\alpha}(\omega) \bar{n}_{\alpha}(\omega), \\ \gamma_{21}^{(\alpha)}(\omega) &= \Gamma_{\alpha}(\omega) [1 + \bar{n}_{\alpha}(\omega)],\end{aligned}\quad (4.98)$$

with the energy dependent rates $\Gamma_{\alpha}(\omega)$ defined in Eq. (4.44). We observe that each bath separately fulfills a local detailed balance condition again, i.e.,

$$\frac{\gamma_{12}^{(\alpha)}(-\omega)}{\gamma_{21}^{(\alpha)}(\omega)} = \frac{\bar{n}_{\alpha}(\omega)}{1 + \bar{n}_{\alpha}(\omega)} = e^{-\beta_{\alpha}(\omega - \mu_{\alpha})}.\quad (4.99)$$

For the sake of a brief notation, we work in the wide-band limit with $\Gamma_{\alpha}(\omega) = \Gamma_{\alpha}$ throughout the following sections.

4.3.2 Liouvillian

In order to derive the respective Liouvillian for the considered bosonic transport setup, we start by calculating the rate matrix from Eq. (2.54). Using the results derived in Sec. 4.3.1, we find for the rates the explicit expressions

$$\gamma_{ab,ba} = \sum_{\alpha} \left[\gamma_{12}^{(\alpha)}(\omega_{a,b}) |\langle a | \hat{A}_1 | b \rangle|^2 + \gamma_{21}^{(\alpha)}(\omega_{a,b}) |\langle b | \hat{A}_1 | a \rangle|^2 \right],\quad (4.100)$$

analogue to fermionic result from Eq. (4.46). Note, that here and in the following, we use the abbreviation $\omega_{i,j}$ for transition energies with respect to the bosonic eigenbasis as introduced in Eq. (2.39).

The eigenstates $|a\rangle$ and $|b\rangle$ correspond to local bosonic Fock states. Due to the effect of the system operators from Eq. (4.93) on these Fock states, the only nonvanishing transition rates are

$$\begin{aligned}\gamma_{n(n+1),(n+1)n} &= (n+1) \sum_{\alpha} \gamma_{12}^{(\alpha)}(-\omega_{n+1,n}), & \gamma_{(n-1)n,n(n-1)} &= n \sum_{\alpha} \gamma_{12}^{(\alpha)}(-\omega_{n,n-1}), \\ \gamma_{(n+1)n,n(n+1)} &= (n+1) \sum_{\alpha} \gamma_{21}^{(\alpha)}(\omega_{n+1,n}), & \gamma_{n(n-1),(n-1)n} &= n \sum_{\alpha} \gamma_{21}^{(\alpha)}(\omega_{n,n-1}).\end{aligned}\quad (4.101)$$

Inserting these results into the rate equation for the populations given in Eq. (2.54), we still need to calculate the summation over all possible populations n . For bosons this number is unbounded, i.e., $0 \leq n < \infty$, and hence the corresponding Liouvillian is infinitely large. This makes it in general impossible to solve the steady-state exactly. Except for some generic systems as for example the harmonic oscillator where the summation in Eq. (2.54) can be solved exactly.

For this reason, we truncate the system Hilbert space at small particle numbers. We explicitly consider in the following the case of a system where at most $n_{\max} = 2$

particles can enter. Then, we can calculate the sum in Eq. (2.54) and subsequently perform the Fourier transform according to Eq. (2.75). This leads to the corresponding equation in Liouville-space

$$\frac{\partial}{\partial t} \begin{pmatrix} \rho_0 \\ \rho_1 \\ \rho_2 \end{pmatrix} = [-\mathcal{W}_0 + \mathcal{W}_+(\chi, \eta) + \mathcal{W}_-(\chi, \eta)] \cdot \begin{pmatrix} \rho_0 \\ \rho_1 \\ \rho_2 \end{pmatrix}. \quad (4.102)$$

Here, the coherent evolution \mathcal{W}_0 and the jump terms \mathcal{W}_+ and \mathcal{W}_- in the wide-band limit $\Gamma_\alpha(\omega) = \Gamma_\alpha$ are given by

$$\mathcal{W}_0 = \sum_\alpha \Gamma_\alpha \begin{pmatrix} \bar{n}_\alpha(\omega_{1,0}) & 0 & 0 \\ 0 & 2\bar{n}_\alpha(\omega_{2,1}) + [1 + \bar{n}_\alpha(\omega_{1,0})] & 0 \\ 0 & 0 & 2(1 + \bar{n}_\alpha(\omega_{2,1})) \end{pmatrix}, \quad (4.103)$$

$$\mathcal{W}_+(\chi, \eta) = \sum_\alpha \Gamma_\alpha \begin{pmatrix} 0 & e^{i(\chi_\alpha - \eta_\alpha \omega_{1,0})} [1 + \bar{n}_\alpha(\omega_{1,0})] & 0 \\ 0 & 0 & 2e^{i(\chi_\alpha - \eta_\alpha \omega_{2,1})} [1 + \bar{n}_\alpha(\omega_{2,1})] \\ 0 & 0 & 0 \end{pmatrix}, \quad (4.104)$$

$$\mathcal{W}_-(\chi, \eta) = \sum_\alpha \Gamma_\alpha \begin{pmatrix} 0 & 0 & 0 \\ e^{-i(\chi_\alpha - \eta_\alpha \omega_{1,0})} \bar{n}_\alpha(\omega_{1,0}) & 0 & 0 \\ 0 & 2e^{-i(\chi_\alpha - \eta_\alpha \omega_{2,1})} \bar{n}_\alpha(\omega_{2,1}) & 0 \end{pmatrix}. \quad (4.105)$$

The steady-state of the system defined in Eq. (2.90) can then be calculated to

$$\bar{\rho} = \begin{pmatrix} \bar{\rho}_0 \\ \bar{\rho}_1 \\ \bar{\rho}_2 \end{pmatrix} = \frac{1}{2\theta} \begin{pmatrix} \gamma_{21,12} \gamma_{10,01} \\ \gamma_{21,12} \gamma_{01,10} \\ \gamma_{12,21} \gamma_{01,10} \end{pmatrix} = \frac{1}{\theta} \sum_{\alpha, \beta} \Gamma_\alpha \Gamma_\beta \begin{pmatrix} [1 + \bar{n}_\alpha(\omega_{1,0})] [1 + \bar{n}_\beta(\omega_{2,1})] \\ \bar{n}_\alpha(\omega_{1,0}) [1 + \bar{n}_\beta(\omega_{2,1})] \\ \bar{n}_\alpha(\omega_{1,0}) \bar{n}_\beta(\omega_{2,1}) \end{pmatrix}, \quad (4.106)$$

where the normalization constant θ is given by

$$\theta = \sum_{\alpha, \beta} \Gamma_\alpha \Gamma_\beta \{1 + \bar{n}_\beta(\omega_{2,1}) + \bar{n}_\alpha(\omega_{1,0}) [2 + 3\bar{n}_\beta(\omega_{2,1})]\}. \quad (4.107)$$

Considering the ratios

$$\frac{\bar{\rho}_1}{\bar{\rho}_0} = \frac{\gamma_{01,10}}{\gamma_{10,01}}, \quad \frac{\bar{\rho}_2}{\bar{\rho}_1} = \frac{\gamma_{12,21}}{\gamma_{21,12}}, \quad \frac{\bar{\rho}_2}{\bar{\rho}_0} = \frac{\bar{\rho}_1}{\bar{\rho}_0} \frac{\bar{\rho}_2}{\bar{\rho}_1}, \quad (4.108)$$

we find that they result in a global detailed balance relation, if only a single reservoir would be present.

4.3.3 Steady-state currents

Using the results from Eq. (4.101), we can now calculate the bosonic steady-state currents according to Eq. (2.93) and Eq. (2.94). We find that in general the steady-

state currents through the Bose system measured at reservoir α are given by

$$J_N^{(\alpha)} = - \sum_{n=0}^{\infty} (n+1) \mathcal{I}_n^{(\alpha)}, \quad (4.109)$$

$$J_E^{(\alpha)} = - \sum_{n=0}^{\infty} \omega_{n+1,n} (n+1) \mathcal{I}_n^{(\alpha)}, \quad (4.110)$$

with an infinite sum over all possible system populations n . Here, we use the wide-band limit $\Gamma_\alpha(\omega) = \Gamma_\alpha$ again and introduce the abbreviation

$$\mathcal{I}_n^{(\alpha)} = \Gamma_\alpha \{ [\bar{n}_\alpha(\omega_{n+1,n}) + 1] \bar{\rho}_{n+1} - \bar{n}_\alpha(\omega_{n+1,n}) \bar{\rho}_n \}. \quad (4.111)$$

As expected for the steady-state currents, we find that they respect particle and energy conservation analog to the fermionic currents in Eq. (4.59). Hence, we focus in the following on the left reservoir only and drop the bath index. As discussed in Sec. 4.3.2, we can not in general solve the infinite summation in the above expression. Therefore, we use the truncation scheme introduced in the previous section and restrict the bosonic Hilbert space to at most two particles. This gives rise to two distinct transition frequencies, which we label by

$$\begin{aligned} \omega_1 &\equiv \omega_{1,0} = E_1 - E_0 = \Omega, \\ \omega_2 &\equiv \omega_{2,1} = E_2 - E_1 = \Omega + U. \end{aligned} \quad (4.112)$$

With the restriction of the maximum particle number the steady-state currents in the wide-band limit are explicitly given by

$$\begin{aligned} \frac{J_N^{(\alpha)}}{\Gamma_\alpha} &= \left(\bar{n}_\alpha(\omega_1) + [2\bar{n}_\alpha(\omega_2) - \bar{n}_\alpha(\omega_1) - 1] \frac{\bar{\rho}_1}{\bar{\rho}_0} - 2[1 + \bar{n}_\alpha(\omega_2)] \frac{\bar{\rho}_2}{\bar{\rho}_0} \right) \bar{\rho}_0 \\ &= \left(\bar{n}_\alpha(\omega_1) + [2\bar{n}_\alpha(\omega_2) - \bar{n}_\alpha(\omega_1) - 1] \frac{\sum_\beta \gamma_{12}^{(\beta)}(-\omega_1)}{\sum_\beta \gamma_{21}^{(\beta)}(\omega_1)} \right. \\ &\quad \left. - 2[1 + \bar{n}_\alpha(\omega_2)] \frac{\sum_\beta \gamma_{12}^{(\beta)}(-\omega_1)}{\sum_\beta \gamma_{21}^{(\beta)}(\omega_1)} \frac{\sum_{\beta'} \gamma_{12}^{(\beta')}(-\omega_2)}{\sum_{\beta'} \gamma_{21}^{(\beta')}(\omega_2)} \right) \bar{\rho}_0 \\ &= \left(\bar{n}_\alpha(\omega_1) + [2\bar{n}_\alpha(\omega_2) - \bar{n}_\alpha(\omega_1) - 1] \frac{\sum_\beta \Gamma_\beta \bar{n}_\beta(\omega_1)}{\sum_\beta \Gamma_\beta [1 + \bar{n}_\beta(\omega_1)]} \right. \\ &\quad \left. - 2[1 + \bar{n}_\alpha(\omega_2)] \frac{\sum_{\beta,\gamma} \Gamma_\beta \Gamma_\gamma \bar{n}_\beta(\omega_1) \bar{n}_\gamma(\omega_2)}{\sum_{\beta,\gamma} \Gamma_\beta \Gamma_\gamma [1 + \bar{n}_\beta(\omega_1)] [1 + \bar{n}_\gamma(\omega_2)]} \right) \\ &\quad \times \frac{\sum_{\alpha',\beta'} \Gamma_{\alpha'} \Gamma_{\beta'} [1 + \bar{n}_{\alpha'}(\omega_1)] [1 + \bar{n}_{\beta'}(\omega_2)]}{\sum_{\alpha',\beta'} \Gamma_{\alpha'} \Gamma_{\beta'} \{1 + \bar{n}_{\beta'}(\omega_2) + \bar{n}_{\alpha'}(\omega_1) [2 + 3\bar{n}_{\beta'}(\omega_2)]\}}, \end{aligned} \quad (4.113)$$

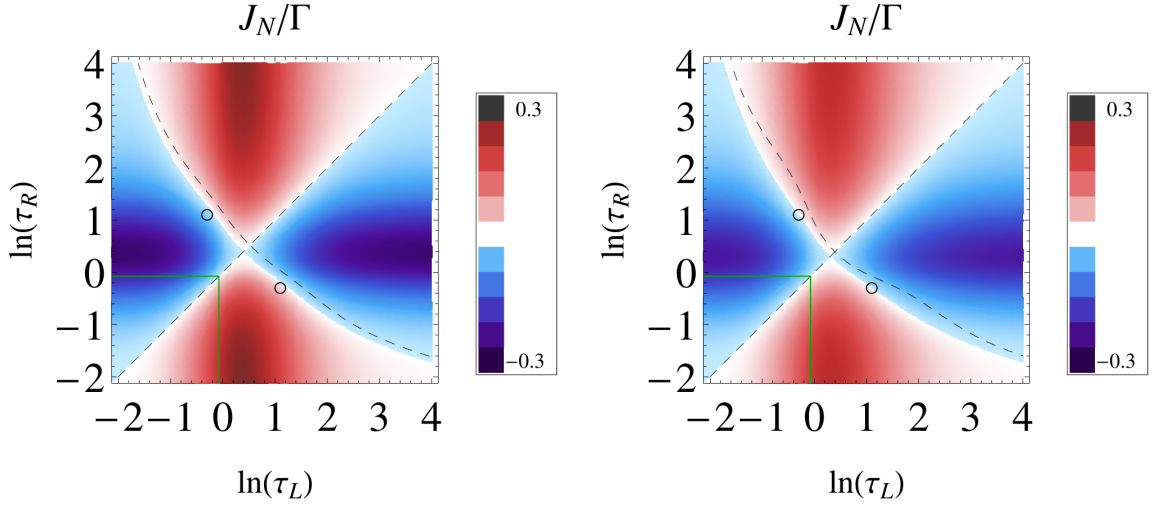


Figure 4.14: Logarithmic plot of the steady-state particle current of the bosonic system with different transition frequencies, versus the dimensionless temperatures of the reservoirs at fixed, equal density. In both plots, we set $\Omega = T_c$ and use equal tunneling rates $\Gamma_L = \Gamma_R = \Gamma$. For the particle interaction we assume $U = 0.01T_c$ (left panel) and $U = 10T_c$ (right panel). The solid lines (thin, green) indicate the on-set of Bose-Einstein condensation in both reservoirs. We also show where the corresponding steady-state energy currents vanish (dashed line).

$$\begin{aligned}
 \frac{J_E^{(\alpha)}}{\Gamma_\alpha} &= \omega_1 \left(\bar{n}_\alpha(\omega_1) + \left\{ 2 \frac{\omega_2}{\omega_1} \bar{n}_\alpha(\omega_2) - \bar{n}_\alpha(\omega_1) - 1 \right\} \frac{\bar{\rho}_1}{\bar{\rho}_0} - 2 \frac{\omega_2}{\omega_1} [\bar{n}_\alpha(\omega_2) + 1] \frac{\bar{\rho}_2}{\bar{\rho}_0} \right) \bar{\rho}_0 \\
 &= \omega_1 \left(\bar{n}_\alpha(\omega_1) + \left[2 \frac{\omega_2}{\omega_1} \bar{n}_\alpha(\omega_2) - \bar{n}_\alpha(\omega_1) - 1 \right] \frac{\sum_\beta \Gamma_\beta \bar{n}_\beta(\omega_1)}{\sum_\beta \Gamma_\beta [1 + \bar{n}_\beta(\omega_1)]} \right. \\
 &\quad \left. - 2 \frac{\omega_2}{\omega_1} [\bar{n}_\alpha(\omega_2) + 1] \frac{\sum_{\beta, \gamma} \Gamma_\beta \Gamma_\gamma \bar{n}_\beta(\omega_1) \bar{n}_\gamma(\omega_2)}{\sum_{\beta, \gamma} \Gamma_\beta \Gamma_\gamma [1 + \bar{n}_\beta(\omega_1)] [1 + \bar{n}_\gamma(\omega_2)]} \right) \\
 &\quad \times \frac{\sum_{\alpha', \beta'} \Gamma_{\alpha'} \Gamma_{\beta'} [1 + \bar{n}_{\alpha'}(\omega_1)] [1 + \bar{n}_{\beta'}(\omega_2)]}{\sum_{\alpha', \beta'} \Gamma_{\alpha'} \Gamma_{\beta'} \{1 + \bar{n}_{\beta'}(\omega_2) + \bar{n}_{\alpha'}(\omega_1) [2 + 3\bar{n}_{\beta'}(\omega_2)]\}}.
 \end{aligned} \tag{4.114}$$

In order to gain a better physical insight for the above currents, we first discuss the limit of a single transition frequency in the system only. Therefore, assuming a very strong particle interaction, i.e., $U \gg \{\Omega, T\}$, restricts the Hilbert space to at most one bosonic particle in the system. Thus, the system can be either empty or single occupied which gives rise to a single transition frequency Ω . In this case, we obtain the tight-binding limit, i.e., $\lim_{U \rightarrow \infty} J_E = \Omega \lim_{U \rightarrow \infty} J_N$, where the steady-state particle current takes on the form

$$\lim_{U \rightarrow \infty} J_N = \frac{\Gamma_L \Gamma_R [\bar{n}_L(\Omega) - \bar{n}_R(\Omega)]}{\Gamma_L [1 + 2\bar{n}_L(\Omega)] + \Gamma_R [1 + 2\bar{n}_R(\Omega)]}, \tag{4.115}$$

which coincides with the result found in Ref. [134] for a single bosonic transport channel. Analogous to the fermionic case, we find that the current through a transport channel with energy Ω is proportional to the difference in the corresponding mean occupations in the left and right reservoir. Nevertheless, in the bosonic case, we find a different normalization compared to the fermionic limit current in Eq. (4.60).

As an example we plotted the steady-state particle current for different transition energies in Fig. 4.14. We observe that the current amplitude is strongest if the interaction strength U is weak. Increasing the interaction strength shifts the corresponding transport channel to higher energies which are less occupied in the reservoirs. Therefore, the contribution of these transport channels to the current is diminished. Additionally, we see two lines where the steady-state particle current vanishes. The diagonal line reflects the thermodynamic equilibrium, i.e., if $\Delta_T = 0$. The reason for the emergence of the second line lies in the temperature dependence of the mean occupations as discussed for the fermionic setup in Sec. 4.2.3.

For the energy current, we find qualitatively the same behavior as for the particle current. However, depending on the system parameters the energy current can be finite even for vanishing particle current. We indicated the temperatures where the energy current vanishes by dashed lines in both plots of Fig. 4.14. We observe that the nonequilibrium lines where the energy current vanishes, are shifted to higher temperatures compared to the vanishing particle current. Contrary to the fermionic steady-state current plotted in Fig. 4.6, we do not observe a qualitative change in the bosonic particle current in dependence of the transition energies. This behavior stems from the fact that there is no equivalent of the Fermi energy and no Pauli exclusion principle in bosonic systems. Hence, the bosonic mean occupations look qualitatively the same for all energy levels (see Fig. 4.3). The thin, solid, green lines in Fig. 4.14 indicate the onset of Bose-Einstein in each reservoir, respectively. Within the condensate phase we observe a finite particle current, which results from the thermal fraction of the Bose gas. This thermal fraction decrease with temperature like $T^{3/2}$ and, therefore, the current exactly vanishes at $T = 0$.

In our BMS master equation approach the coherences decouple from the populations and, thus, can be neglected. However, if one enters the condensate phase the coherences between the particles become stronger with decreasing temperature. Therefore, the higher orders of the expansion from Eq. (2.23) should become important and the decoupling between coherences and populations is not expected to hold anymore. Hence, we do not expect that our results remain valid deep in the condensate phase.

4.3.4 Linear transport coefficients

Since in the tight-binding limit we can not calculate all the linear response transport coefficients, we consider in the following the truncation scheme presented in

the previous section, which is established by truncating the bosonic Hilbert space at a maximum number of two particles. The resulting steady-state currents from Eq. (4.113) and Eq. (4.114) can then be used to establish the Onsager system of equations according to Eq. (2.148). Using the wide-band limit $\Gamma_\alpha(\omega) = \Gamma_\alpha$ and linearizing the generalized heat current from Eq. (2.144) and the particle current from Eq. (4.113) with respect to their corresponding affinities results in the kinetic coefficients

$$\tilde{L}_{11} = \frac{\Gamma_L \Gamma_R \bar{n}(\omega_1) [1 + \bar{n}(\omega_2)] [1 + \bar{n}(\omega_1)] (\mu - T \frac{\partial \mu}{\partial T} - \omega_1)^2 + 2\bar{n}(\omega_2) (\mu - T \frac{\partial \mu}{\partial T} - \omega_2)^2}{\Gamma_L + \Gamma_R [1 + \bar{n}(\omega_2) + \bar{n}(\omega_1) [2 + 3\bar{n}(\omega_2)]]} \geq 0, \quad (4.116)$$

$$\tilde{L}_{12} = \frac{\Gamma_L \Gamma_R \bar{n}(\omega_1) [1 + \bar{n}(\omega_2)] [1 + \bar{n}(\omega_1)] (\mu - T \frac{\partial \mu}{\partial T} - \omega_1) + 2\bar{n}(\omega_2) (\mu - T \frac{\partial \mu}{\partial T} - \omega_2)}{\Gamma_L + \Gamma_R [1 + \bar{n}(\omega_2) + \bar{n}(\omega_1) [2 + 3\bar{n}(\omega_2)]]}, \quad (4.117)$$

$$\tilde{L}_{12} = \tilde{L}_{21}, \quad (4.118)$$

$$\tilde{L}_{22} = \frac{\Gamma_L \Gamma_R}{\Gamma_L + \Gamma_R} \frac{\bar{n}(\omega_1) [1 + \bar{n}(\omega_2)] [1 + \bar{n}(\omega_1) + 2\bar{n}(\omega_2)]}{1 + \bar{n}(\omega_2) + \bar{n}(\omega_1) [2 + 3\bar{n}(\omega_2)]} \geq 0, \quad (4.119)$$

and the determinant of the Onsager matrix becomes

$$\tilde{D} = 2 \left(\frac{\Gamma_L \Gamma_R}{\Gamma_L + \Gamma_R} \right)^2 \bar{n}(\omega_2) [1 + \bar{n}(\omega_1)] \left(\frac{\bar{n}(\omega_1) [1 + \bar{n}(\omega_2)] (\omega_1 - \omega_2)}{1 + \bar{n}(\omega_2) + \bar{n}(\omega_1) [2 + 3\bar{n}(\omega_2)]} \right)^2 \geq 0. \quad (4.120)$$

Here, we drop the bath index again since the kinetic coefficients presented above are all evaluated in equilibrium, i.e., the energy-levels in both reservoirs have the same mean occupations. With these results, we can calculate the linear transport coefficients following the procedure outlined in Sec. 2.14.2.

4.3.4.1 Matter conductance

First, we take a look at the linear response matter conductance for the bosonic system. Using the result from Eq. (4.119), we find that the bosonic matter conductance for the considered transport setup according to Eq. (2.151) reads as

$$\tilde{\sigma} = \frac{\Gamma_L \Gamma_R}{\Gamma_L + \Gamma_R} \frac{\bar{n}(\omega_1) [1 + \bar{n}(\omega_2)] [1 + \bar{n}(\omega_1) + 2\bar{n}(\omega_2)]}{T \{1 + \bar{n}(\omega_2) + \bar{n}(\omega_1) [2 + 3\bar{n}(\omega_2)]\}} \geq 0. \quad (4.121)$$

In Fig. 4.15, we plot this transport coefficient for different transition energies versus the normalized temperature (left) and the normalized particle density (right). Depending mostly on the lowest transition frequency Ω , the matter conductance has a maximum value at a finite temperature above the critical value T_c . Decreasing the lower transition frequency Ω shifts the maximum to smaller temperatures whereas increasing the transition frequency shifts the maximum away to higher

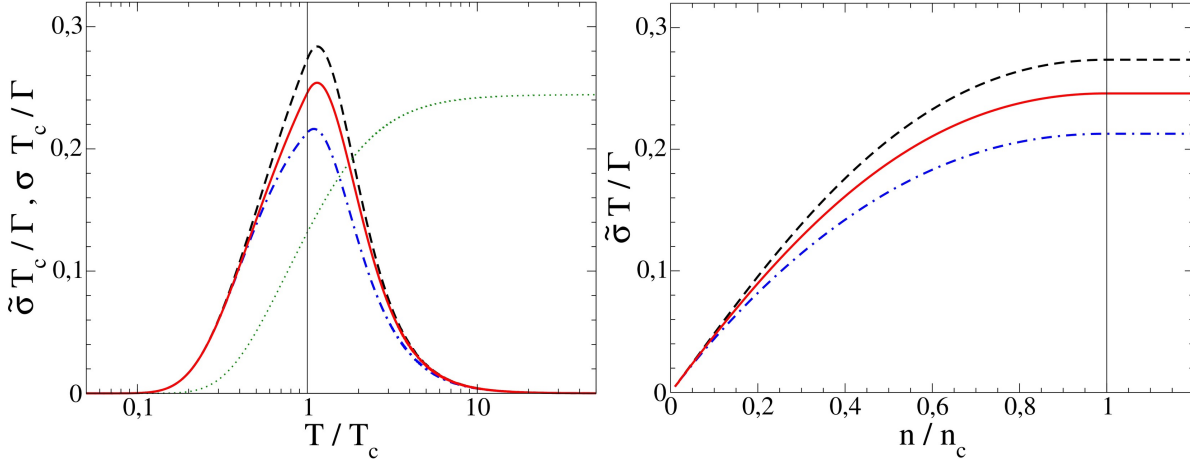


Figure 4.15: Bosonic matter conductance $\tilde{\sigma}$ at a constant particle density (left) and at a constant temperature (right) versus the normalized temperature and particle density, respectively. In both plots, we assume equal tunneling rates $\Gamma_L = \Gamma_R = \Gamma$. In the left panel, we use a constant on-site energy $\Omega = T_c$ and different interaction strengths $U = 0.5T_c$ (dashed line) and $U = T_c$ (solid line). In the right panel, we use a constant on-site energy of $\Omega = T$ and different particle interactions $U = 0.5T$ (dashed line) and $U = T$ (solid line). In both plots the dot-dashed lines correspond to the limit $U \rightarrow \infty$. For the conductance with constant chemical potential σ , we use $\Omega = T_c$, $U = T_c$ and additionally set $\mu = -0.5T_c$ (thin, dotted line).

temperatures. Increasing the temperature leads to a decrease of the matter conductance since the occupation of the transition energy level in the reservoirs is reduced. The influence of the second transport channel is mainly reflected in the maximum value of the transport coefficient. This value is increased if the transport channels are close together, i.e., if the interaction strength U is small. If the interaction strength is increased the respective transport channel is shifted to higher energies and contributes less to the current because of the lower occupations in the reservoir. Thus, the maximum conductance decreases to a minimum value resulting from the lower transport channel (dot-dashed line).

We can also determine this limit analytically which yields

$$\lim_{U \rightarrow \infty} \tilde{\sigma} = \frac{\Gamma_L \Gamma_R}{\Gamma_L + \Gamma_R} \frac{1}{2T \sinh\left(\frac{\Omega - \mu}{T}\right)}. \quad (4.122)$$

For comparison, we also included a plot for the conductance with constant chemical potential (thin, dotted line). Here, the conductance takes on a constant finite value

$$\lim_{T \rightarrow \infty} \sigma = \frac{1}{3} \left(\frac{1}{\omega_1 - \mu} + \frac{2}{\omega_2 - \mu} \right), \quad (4.123)$$

in the limit of high temperature. This is caused by the fact that for a constant chemical potential the occupations of energy levels in the reservoirs increase approximately linear with the temperature in the high temperature limit. If the temperature approaches zero the conductance vanishes due to the depletion of the transition energy levels in the reservoirs. Furthermore, we notice that due to the vanishing of the chemical potential at the critical temperature the matter conductance is non-analytic at $T = T_c$. This effect is more emphasized for smaller transition frequencies. This non-analytic behavior is well known from the heat capacity of the ideal Bose gas [201] which allows to characterize the Bose-Einstein condensation as a third-order phase-transition according to the Ehrenfest-classification of thermal phase-transitions.

In the right panel of Fig. 4.15, we plot the bosonic matter conductance for a constant temperature versus the normalized particle density for different transition energies. In the limit of small densities, we observe an almost linear increase of the conductance with the particle density. As the critical density is approached the slope decreases and exactly vanishes at the critical density. Here, the matter conductance assumes its maximum value given by

$$\tilde{\sigma}(n \geq n_C) = \frac{\Gamma_L \Gamma_R}{\Gamma_L + \Gamma_R} \frac{e^{\frac{\omega_2}{T}} \left[e^{\frac{\omega_1}{T}} \left(e^{\frac{\omega_2}{T}} + 1 \right) - 2 \right]}{T \left(1 - e^{\frac{\omega_1}{T}} \right) \left(1 - e^{\frac{\omega_2}{T}} \right) \left[e^{\frac{\omega_2}{T}} \left(e^{\frac{\omega_1}{T}} + 1 \right) + 1 \right]}. \quad (4.124)$$

For densities above the critical density the matter conductance remains constant since the occupations in this regime are independent of the particle density. All additional particles occupy the reservoir ground-state and, thus, do not contribute to the currents. As before the maximum value is mostly affected by the energy Ω . In general, we find that the smaller the energies Ω and U , the higher is the maximum matter conductance.

4.3.4.2 Heat conductance

Inserting the kinetic coefficient from Eq. (4.119) and the determinant of the Onsager matrix from Eq. (4.120) into the definition in Eq. (2.152), we find the bosonic heat conductance for the considered transport setup which reads as

$$\tilde{\kappa} = \frac{\Gamma_L \Gamma_R}{\Gamma_L + \Gamma_R} \frac{2\bar{n}(\omega_1) [1 + \bar{n}(\omega_1)] \bar{n}(\omega_2) [1 + \bar{n}(\omega_2)] (\omega_1 - \omega_2)^2}{T^2 [1 + \bar{n}(\omega_1) + 2\bar{n}(\omega_2)] \{1 + \bar{n}(\omega_2) + \bar{n}(\omega_1) [2 + 3\bar{n}(\omega_2)]\}} \geq 0. \quad (4.125)$$

Comparing this expression with the bosonic matter conductance from Eq. (4.121), we find that it fulfills the Wiedemann-Franz law with the bosonic density dependent Lorenz number

$$\tilde{L} = \frac{2[1 + \bar{n}(\omega_1)] \bar{n}(\omega_2) (\omega_1 - \omega_2)^2}{T^2 [1 + \bar{n}(\omega_1) + 2\bar{n}(\omega_2)]^2} = \frac{2U^2}{T^2} \frac{[1 + \bar{n}(\omega_1)] \bar{n}(\omega_2)}{[1 + \bar{n}(\omega_1) + 2\bar{n}(\omega_2)]^2} \geq 0, \quad (4.126)$$

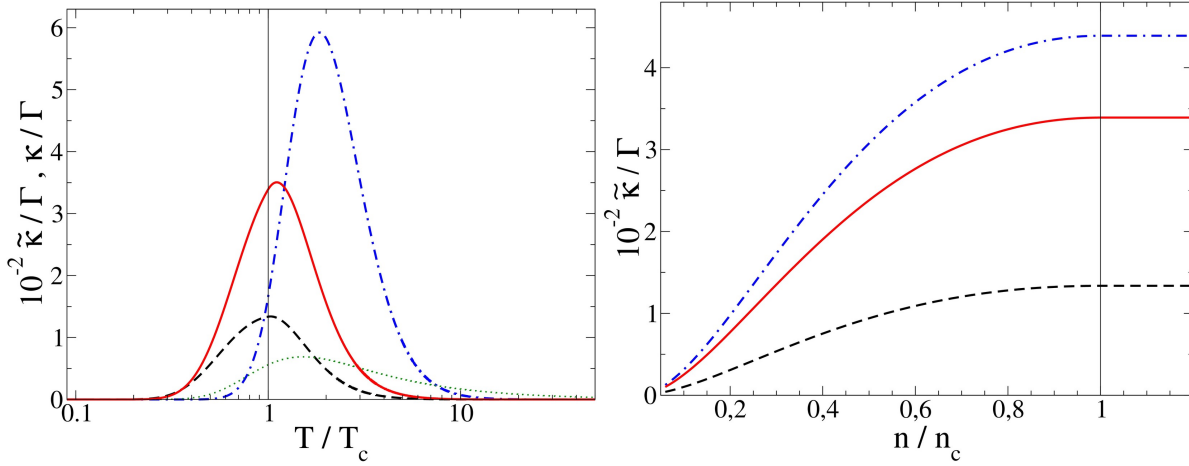


Figure 4.16: Left: Plot of bosonic heat conductance $\tilde{\kappa}$ at a constant particle density for $\Omega = T_c$ and different interaction strengths $U = 0.5T_c$ (dashed line), $U = T_c$ (solid line) and $U = 5T_c$ (dot-dashed line). Additionally, we plot the conventional heat conductance κ with constant chemical potential $\mu = -0.5T_c$ for $U = 0.5T_c$ (dotted line). Right: Plot of bosonic heat conductance $\tilde{\kappa}$ at a constant temperature for $\Omega = T$ and different interaction strengths $U = 0.5T$ (dashed line), $U = T$ (solid line) and $U = 5T$ (dot-dashed line). In both plots we assume equal tunneling rates $\Gamma_L = \Gamma_R = \Gamma$.

which is proportional to the square of the particle interaction strength.

In the right panel of Fig. 4.16, we plot the bosonic thermal conductance for different transition energies versus the normalized density. We observe that this transport coefficient increases with increasing density and reaches a maximum value at the critical density when Bose-Einstein condensation sets in. The value of the maximum depends on the transition energies of the system according to

$$\tilde{\kappa}(n \geq n_c) = \frac{\Gamma_L \Gamma_R}{\Gamma_L + \Gamma_R} \frac{2e^{\frac{\omega_1 + \omega_2}{T}} (\omega_1 - \omega_2)^2}{T^2 \left[e^{\frac{\omega_2}{T}} \left(1 + e^{\frac{\omega_1}{T}} \right) + 1 \right] \left[e^{\frac{\omega_1}{T}} \left(1 + e^{\frac{\omega_2}{T}} \right) - 2 \right]} \geq 0. \quad (4.127)$$

In general, there is a finite interaction strength that maximizes the heat conductance. For a low interaction strength the heat conductance is strongly decreased since it is proportional to $(\omega_1 - \omega_2)^2 = U^2$. For a high interaction strength the heat conductance is also diminished because the occupation of the upper transition energy is decreased. For densities above the critical value the thermal conductance remains constant since the thermal gas fraction in this phase is independent of the density and depends on the temperature only.

We also show the dependence of the thermal conductance on the normalized reservoir temperature in the left panel of Fig. 4.16. Here, we observe the vanishing of the thermal conductance for high and low temperatures. In between these limits the thermal conductance obtains a finite maximal value at a characteristic

temperature which depends on the system transition frequencies. Since the thermal conductance $\tilde{\kappa}$ is proportional to the matter conductance $\tilde{\sigma}$ according to the Wiedemann-Franz law, we also find that this transport coefficient is non-analytic at the critical temperature.

Comparing our density dependent transport coefficient with the conventional result for a constant chemical potential (dotted line), we find qualitatively the same behavior. However, the high temperature properties are slightly different. In fact, we observe that due to the temperature dependent chemical potential the modified coefficient $\tilde{\kappa}$ vanishes faster with increasing temperature than the conventional thermal conductance.

4.3.4.3 Thermopower

Using the results from Eq. (4.119) and Eq. (4.117) and the definition in Eq. (2.155), we can calculate the analog to the thermopower for the considered bosonic transport setup. In the wide-band limit this linear response transport coefficient reads as

$$\tilde{\Sigma} = \frac{[1 + \bar{n}(\omega_1)]\phi_1 + 2\bar{n}(\omega_2)\phi_2}{T[1 + \bar{n}(\omega_1) + 2\bar{n}(\omega_2)]}, \quad (4.128)$$

where we used the abbreviation ϕ_i as defined in Eq. (4.74).

In the left panel of Fig. 4.17, we plot the temperature dependence of this transport coefficient for different values of the interaction strength. Analogously to the fermionic case, we find that the modified Seebeck coefficient takes on a finite positive value in the high temperature limit where the average transported energy per particle becomes $3/2k_B T$. When the temperature is lowered the thermopower decreases. At a temperature where the chemical potential contribution starts to dominate over the transport channel energies, the modified thermopower changes its sign. When the temperature is decreased further the modified thermopower crosses the critical temperature of the phase transition continuously. However, at the critical temperature the modified thermopower is not analytic. Thus, the derivative with respect to temperature shows a jump when the condensate phase is entered. In the condensate phase the modified thermopower decreases further and diverges like $-1/T$ when the temperature approaches absolute zero. Hence, the Peltier coefficient $\tilde{\Pi}$ becomes constant as the temperature approaches zero and we find

$$\lim_{T \rightarrow 0} \tilde{\Pi} = -\omega_1 = -\Omega. \quad (4.129)$$

In general, the particle current is mainly influenced by the lower transport channel. Hence, the modified thermopower just weakly depends on the interaction strength U . For high and low values of the interaction strength the modified thermopower approaches the single frequency limit result (dashed line) which reads as

$$\lim_{U \rightarrow 0} \tilde{\Sigma} = \lim_{U \rightarrow \infty} \tilde{\Sigma} = \frac{\phi_1}{T} = \frac{\mu - T \frac{\partial \mu}{\partial T} - \omega_1}{T}. \quad (4.130)$$

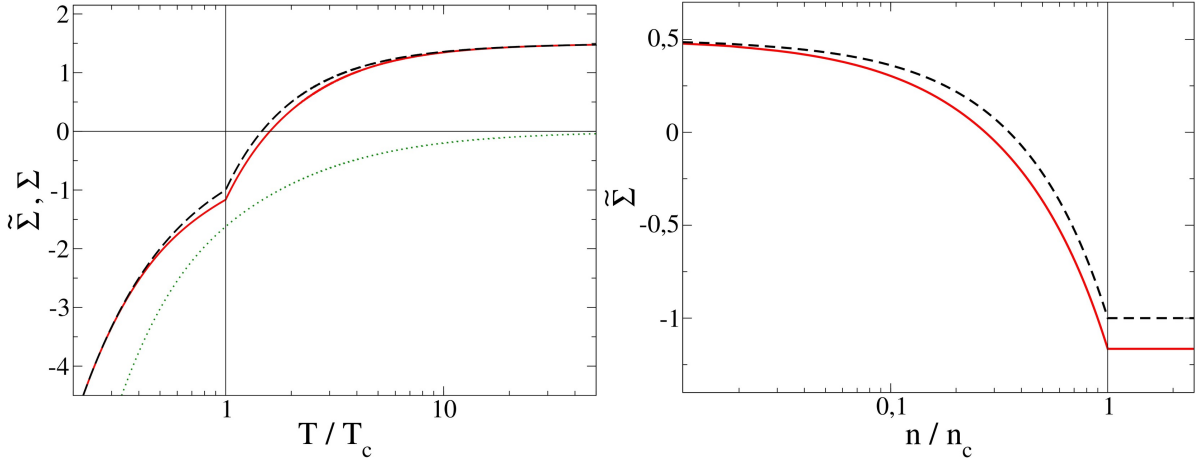


Figure 4.17: Plot of the density-dependent bosonic thermopower $\tilde{\Sigma}$ and conventional thermopower Σ , versus the normalized temperature (left) and the normalized density (right) for an ideal Bose gas. In the left panel, we use $\Omega = U = T_c$ (solid line). In the right panel, we set $\Omega = U = T$ (solid line). For the thermopower with constant chemical potential Σ , we additionally set $\mu = -0.5T_c$ (thin, dotted line). In both plots, we also show the limit curves for $U \rightarrow \infty$ (dashed line).

In between, there is a finite interaction strength that maximizes the modified thermopower at the critical temperature (solid line). However, the relative increase in the thermopower output is still small. On the contrary, the approach with a constant chemical potential predicts a vanishing thermopower for high temperatures (dotted line), and there is no change of sign of the thermopower in dependence of the reservoir temperature. Additionally, the conventional thermopower is continuous and differentiable at the critical temperature and, thus, it is not sensitive to the quantum phase transition of the ideal Bose gas.

Analogously to the behavior for decreasing temperature, we find a monotonous decrease of the thermopower with increasing particle density, which we show in the right panel of Fig. 4.17. For small densities the thermopower assumes a finite positive value given by

$$\lim_{n \rightarrow 0} \tilde{\Sigma} = \frac{3}{2} - \frac{\omega_1}{T}. \quad (4.131)$$

As the density is increased the thermopower decreases, eventually changes its sign and reaches its minimum at the critical density. For even higher densities this transport coefficient remains at the finite value

$$\tilde{\Sigma}(n \geq n_c) = \frac{\omega_1 - \omega_2}{T} \frac{2(1 - e^{\frac{\omega_1}{T}})}{2 - e^{\frac{\omega_1}{T}}(1 + e^{\frac{\omega_2}{T}})} - \frac{\omega_1}{T}, \quad (4.132)$$

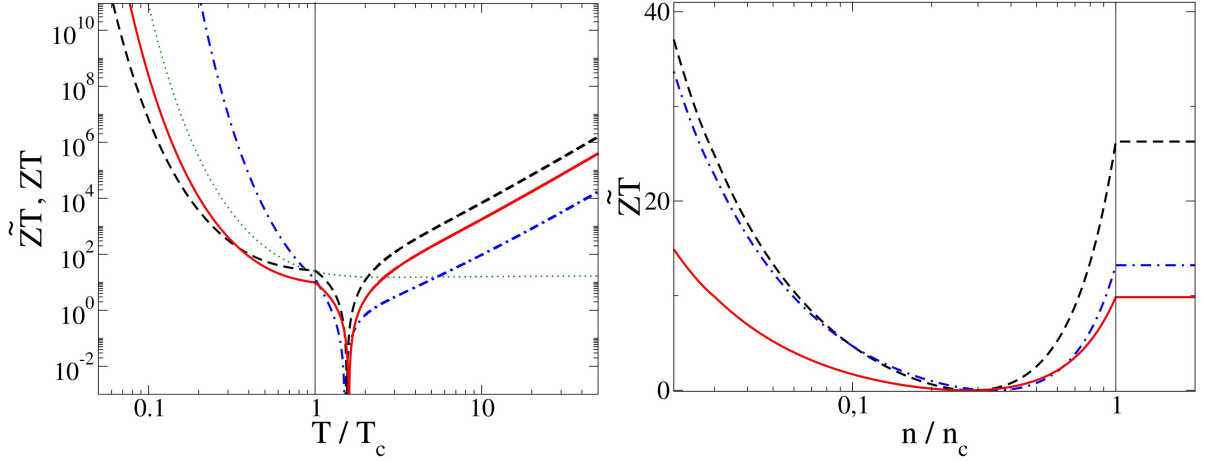


Figure 4.18: Plot of the bosonic figure-of-merit for constant density (left) and constant temperature (right), versus the normalized temperature and the normalized density for an ideal Bose gas. In the left panel, we use $\Omega = T_c$ and different interaction strengths $U = T_c$ (solid line), $U = 0.5T_c$ (dashed line) and $U = 5T_c$ (dot-dashed line). For the figure-of-merit ZT with constant chemical potential, we use $\Omega = U = T_c$ and additionally set $\mu = -0.5T_c$ (thin, dotted line). In the right panel, we set $\Omega = T$ and use $U = T$ (solid line), $U = 0.5T$ (dashed line) and $U = 5T$ (dot-dashed line).

since the chemical potential becomes independent of the particle density in the reservoirs. Note that the result from Eq. (4.132) relates to the modified thermopower at the critical temperature via

$$\tilde{\Sigma}(T = T_c) = \tilde{\Sigma}(n = n_c)|_{T=T_c}. \quad (4.133)$$

4.3.4.4 Thermodynamic performance

Finally, we analyze the figure-of-merit that characterizes the performance of the bosonic thermodynamic device. Inserting the results presented in Eq. (4.128) and Eq. (4.126) into the definition in Eq. (2.157), we find that the figure-of-merit is given by

$$\tilde{Z}T = \frac{\{[1 + \bar{n}(\omega_1)]\phi_1 + 2\bar{n}(\omega_2)\phi_2\}^2}{2[1 + \bar{n}(\omega_1)]\bar{n}(\omega_2)(\omega_1 - \omega_2)^2} \geq 0, \quad (4.134)$$

where we make use of the abbreviation ϕ_i as defined in Eq. (4.74). We plot some results of the bosonic figure-of-merit in Fig. 4.18. In the left panel of Fig. 4.18, we plot the temperature dependence of the figure-of-merit for different values of the interaction strength. We observe that the figure-of-merit vanishes for vanishing linear response particle current. At the critical temperature of the phase transition

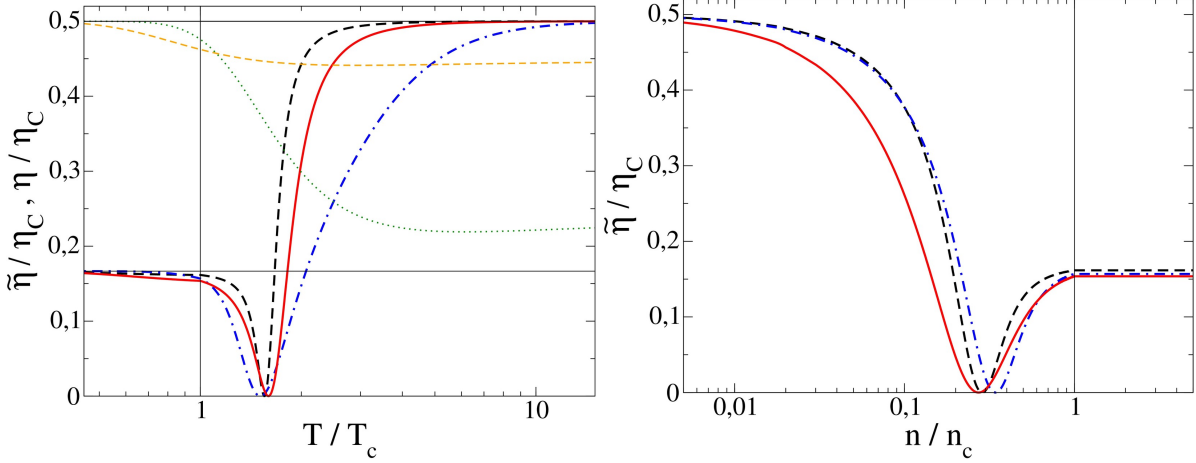


Figure 4.19: Plot of the bosonic efficiency at maximum power for a constant particle density (left) and a constant temperature (right), versus the normalized temperature and the normalized density, respectively. In the left panel, we use $\Omega = T_c$ and different interaction strengths $U = T_c$ (solid line), $U = 0.5T_c$ (dashed line) and $U = 5T_c$ (dot-dashed line). For the efficiency η with constant chemical potential, we use $U = T_c$ (thin, dashed line), $U = 5T_c$ (thin, dotted line) and additionally set $\mu = -0.5T_c$. In the right panel, we set $\Omega = T$ and use $U = T$ (solid line), $U = 0.5T$ (dashed line) and $U = 5T$ (dot-dashed line).

the figure-of merit is non-differentiable but continuous. In the limit of high and low temperatures the figure-of-merit increases exponentially. In general, we find the same qualitative behavior for different interaction strengths. However, in the condensate phase for $T < T_c$, the configuration with high interaction strength yield higher figure-of-merits, whereas in the normal phase for $T > T_c$, configurations with small interaction strengths yield higher figure-of-merit. At the transition temperature the figure-of-merit assumes the positive value

$$\tilde{Z}T(T = T_c) = \frac{\{[1 + \bar{n}(\omega_1)]\omega_1 + 2\bar{n}(\omega_2)\omega_2\}^2}{2[1 + \bar{n}(\omega_1)]\bar{n}(\omega_2)(\omega_1 - \omega_2)^2}. \quad (4.135)$$

For comparison, we also plot the figure-of-merit for a constant chemical potential (thin, dotted line). Again, we find that in this case the high temperature behavior is modified as the figure-of-merit becomes constant. Additionally, this quantity remains analytic when crossing the critical temperature.

In the right panel of Fig. 4.18, we plot the density dependence of the bosonic figure-of-merit at constant temperature. Again, we see that this quantity vanishes at the density where the particle current is zero. Apart from this point the figure-of-merit increases, both, for higher and lower densities. As the density is increased above the critical value n_c , the figure-of-merit remains constant since the chemical

potential becomes independent of the particle density.

For a quantitative analysis we also consider the efficiency at maximum power according to Eq. (2.158). Some results are plotted in Fig. 4.19 for the same parameters as in Fig. 4.18. Comparing with the figure-of-merit, we can confirm that the thermodynamic device becomes maximally efficient in the limit of high temperatures, i.e.,

$$\lim_{T \rightarrow \infty} \tilde{\eta} = \frac{1}{2} \eta_C, \quad (4.136)$$

independent of the transition frequencies. Moreover, we find that in the condensate phase the efficiency at maximum power also approaches a fixed finite value independent of the system energies which reads as

$$\lim_{T \rightarrow 0} \tilde{\eta} = \frac{1}{6} \eta_C. \quad (4.137)$$

These two limiting values for the efficiency at maximum power can also be recovered in the single-frequency limit where the transition energy ω_2 is shifted to high values and the efficiency becomes

$$\lim_{U \rightarrow \infty} \tilde{\eta} = \frac{\eta_C}{4 + 2 \operatorname{sgn}\left(T \frac{\partial \mu}{\partial T} - \mu + \Omega\right)} \geq 0, \quad (4.138)$$

where $\operatorname{sgn}(x)$ is the sign function as defined in Eq. (2.44). Hence, we find that, depending on the temperature and on the energy Ω the efficiency approaches one of the values from Eq. (4.136) and Eq. (4.137). A similar behavior can be observed in the case of a small particle density where we find

$$\lim_{n \rightarrow 0} \tilde{\eta} = \frac{\eta_C}{4 - 2 \operatorname{sgn}\left(\frac{3}{2} T - \Omega\right)} \geq 0. \quad (4.139)$$

Hence, for system energies smaller than the average thermal energy per particle, i.e., $\Omega < 3/2 k_B T$, the device works with half the Carnot efficiency which is the linear response optimum efficiency at maximum power. For energies that lie above this value the efficiency is reduced to $\eta_C/6$ and hardly changes in dependence of the particle density. Nevertheless, for all cases we find a non-analytic but continuous crossing at the critical temperature and particle density.

Chapter 5

Summary

In this thesis, we used a Markovian master equation approach to derive and investigate the steady-state transport properties of several few-level quantum system, that are weakly coupled to multiple surrounding reservoirs, which are held at different temperatures and/or chemical potentials.

In the first part of this thesis, we studied the electronic transport properties of a system of two parallel double-quantum dots which are subject to a charge-qubit impurity. This additional defect affects the electronic transport through the double-quantum dot structure. In particular, we investigated its effect on the steady-state particle currents in the ultra-strong and strong Coulomb blockade regimes with one electron in both or each double-quantum dot, respectively.

We find that the charge-qubit detuning gives rise to an asymmetry that prevents the closing of Coulomb diamonds and leads to negative differential conductance and a anti current-correlation in the low electron-number subspace. This result is in accordance with other theoretical [176, 202, 203] and experimental [204, 205] works which investigate highly asymmetric quantum dot structures. The width as well as the position of the gaps depend on the parameters of the charge-qubit. In the ultra-strong and strong Coulomb blockade regimes, we were able to extract analytic results for the steady-state current in the high-bias regime. Moreover, from the respective system energy eigenvalues, we could analytically determine the width and position of the gap in dependence of the parameters of the charge-qubit.

Additionally, we analyzed the purity of the reduced system steady-state density matrix and found that the purity of the system is preserved. Hence, for low enough temperatures it is possible to prepare the system in a pure eigenstate. In addition, the back-action on the charge-qubit allows us to render its eigenstates pure as well. Furthermore, we find that by carefully tuning the parameters in the system it is possible to influence the steady-state localization of the charge-qubit electron.

Finally, we studied the impact of the charge-qubit on the entanglement between the two transport channels. Here, we observe on the one hand a destruction of Bell states due to the charge-qubit tunneling amplitude J and detuning Ω . On the other hand, we find an increase of entanglement of the remaining eigenstates due to the modification parameter G . Besides investigating the entanglement in the Coulomb diamonds, we analyzed the generalized transport concurrence in the exterior of the

Coulomb diamond, and found that the entanglement is slightly decreased by the charge-qubit.

In the second part of this thesis, we calculated the steady-state particle- and energy fluxes and derived the linear response transport coefficients for a two-terminal transport setup with both, ultra-cold bosons and ultra-cold fermions. In particular, we took into account that in the framework of a grand-canonical ensemble theory the chemical potential of these reservoirs depends on their respective temperature and particle density.

We found that the non-linearity introduced by the temperature- and density dependent chemical potential strongly influences the steady-state particle and energy currents through the system. Since we keep the particle density in the reservoirs fixed, we always observe finite steady state currents through the system. Moreover, depending on the energy spectrum of the system we could observe multiple regimes where the steady-state currents flow with or against an externally applied thermal bias. This counterintuitive result stems from the temperature- and density-dependence of the mean occupations in the reservoirs induced by the chemical potential.

Subsequently, we established the respective Onsager system of equations from which we derived the linear response transport coefficients of the steady-state currents. A comparison of these coefficients with the ones obtained for a constant chemical potential, we noticed that the temperature- and density-dependent chemical potential yields modifications mainly for high temperatures. Furthermore, by comparing the results for fermionic and bosonic transport, we found clear signatures of criticality in the bosonic transport coefficients. This criticality relates to the thermal phase transition to a Bose-Einstein for low temperatures. Thus, we understand that transport measurements provide new tools to study critical phenomena in non-equilibrium setups in accordance with the findings in Ref. [32].

Finally, we investigated the potential utilization of the proposed setups as thermoelement by analyzing the figure-of-merit and efficiency at maximum power for both the bosonic and fermionic systems. In correspondence with experimental results [105], we found that high figure-of-merits at maximum power can be obtained in both systems. In a more detailed analysis we could in fact show that the maximal possible linear response efficiency can be reached in these systems. This suggests a possible application of transport setups using ultra-cold atomic gases in view of efficient thermopower devices.

Bibliography

- [1] S. de Groot and P. Mazur, *Non-equilibrium Thermodynamics*, Dover Books on Physics Series, 1st edition (Dover Publications, Amsterdam, 1984).
- [2] B. A. Grzybowski, *Chemistry in Motion: Reaction-Diffusion Systems for Micro- and Nanotechnology* (John Wiley & Sons, Singapore, 2009).
- [3] B. Perthame, *Transport Equations in Biology*, Frontiers in Mathematics (Springer, London, 2007).
- [4] H. Haug and S. W. Koch, *Quantum theory of the optical and electronic properties of semiconductors*, 4th edition (World Scientific, Singapore, 2004).
- [5] S. Schmitt-Rink, D. S. Chemla and D. A. B. Miller, "Linear and nonlinear optical properties of semiconductor quantum wells," *Adv. Phys.*, **38**, (1989) 89.
- [6] L. P. Kouwenhoven, D. G. Austing and S. Tarucha, "Few-electron quantum dots," *Rep. Prog. Phys.*, **64**, (2001) 701.
- [7] W. H. Lim, H. Huebl, L. H. Willems van Beveren, S. Rubanov, P. G. Spizzirri, S. J. Angus, R. G. Clark and A. S. Dzurak, "Electrostatically defined few-electron double quantum dot in silicon," *Appl. Phys. Lett.*, **94**, (2009) 173502.
- [8] J. Güttinger, F. Molitor, C. Stampfer, S. Schnez, A. Jacobsen, S. Dröscher, T. Ihn and K. Ensslin, "Transport through graphene quantum dots," *Rep. Prog. Phys.*, **75**, (2012) 126502.
- [9] A. Fujiwara, H. Inokawa, K. Yamazaki, H. Namatsu, Y. Takahashi, N. M. Zimmerman and S. B. Martin, "Single electron tunneling transistor with tunable barriers using silicon nanowire metal-oxide-semiconductor field-effect transistor," *Appl. Phys. Lett.*, **88**, (2006) 053121.
- [10] G. A. Steele, G. Gotz and L. P. Kouwenhoven, "Tunable few-electron double quantum dots and Klein tunnelling in ultraclean carbon nanotubes," *Nature Nanotechnology*, **4**, (2009) 363.
- [11] S. Nadj-Perge, V. S. Pribiag, J. W. G. van den Berg, K. Zuo, S. R. Plissard, E. P. A. M. Bakkers, S. M. Frolov and L. P. Kouwenhoven, "Spectroscopy of Spin-Orbit Quantum Bits in Indium Antimonide Nanowires," *Phys. Rev. Lett.*, **108**, (2012) 166801.

- [12] D. L. Klein, P. L. McEuen, J. E. B. Katari, R. Roth and A. P. Alivisatos, "An approach to electrical studies of single nanocrystals," *Appl. Phys. Lett.*, **68**, (1996) 2574.
- [13] K. J. Vahala, "Optical microcavities." *Nature*, **424**, (2003) 839.
- [14] B. J. van Wees, H. van Houten, C. W. J. Beenakker, J. G. Williamson, L. P. Kouwenhoven, D. van der Marel and C. T. Foxon, "Quantized conductance of point contacts in a two-dimensional electron gas," *Phys. Rev. Lett.*, **60**, (1988) 848.
- [15] M. Vanević, Y. V. Nazarov and W. Belzig, "Elementary Events of Electron Transfer in a Voltage-Driven Quantum Point Contact," *Phys. Rev. Lett.*, **99**, (2007) 076601.
- [16] W. G. van der Wiel, S. De Franceschi, J. M. Elzerman, T. Fujisawa, S. Tarucha and L. P. Kouwenhoven, "Electron transport through double quantum dots," *Rev. Mod. Phys.*, **75**, (2002) 1.
- [17] J. M. Elzerman, R. Hanson, J. S. Greidanus, L. H. Willems van Beveren, S. De Franceschi, L. M. K. Vandersypen, S. Tarucha and L. P. Kouwenhoven, "Few-electron quantum dot circuit with integrated charge read out," *Phys. Rev. B*, **67**, (2003) 161308.
- [18] E. A. Chekhovich, M. N. Makhonin, A. I. Tartakovskii, A. Yacoby, H. Bluhm, K. C. Nowack and L. M. K. Vandersypen, "Nuclear spin effects in semiconductor quantum dots," *Nature Materials*, **12**, (2013) 494.
- [19] F. R. Waugh, M. J. Berry, C. H. Crouch, C. Livermore, D. J. Mar, R. M. Westervelt, K. L. Campman and A. C. Gossard, "Measuring interactions between tunnel-coupled quantum dots," *Phys. Rev. B*, **53**, (1996) 1413.
- [20] L. Gaudreau, G. Granger, A. Kam, G. C. Aers, S. A. Studenikin, P. Zawadzki, M. Pioro-Ladrière, Z. R. Wasilewski and A. S. Sachrajda, "Coherent control of three-spin states in a triple quantum dot," *Nature Physics*, **8**, (2012) 54.
- [21] S. Tarucha, D. G. Austing, T. Honda, R. J. van der Hage and L. P. Kouwenhoven, "Shell Filling and Spin Effects in a Few Electron Quantum Dot," *Phys. Rev. Lett.*, **77**, (1996) 3613.
- [22] L. P. Kouwenhoven, C. M. Marcus, P. L. McEuen, S. Tarucha, R. M. Westervelt and N. S. Wingreen, "Electron transport in quantum dots," in "Proceedings of the NATO Advanced Study Institute on Mesoscopic Electron Transport," , *Series E: Applied Sciences*, volume 345, (Kluwer Academic Publishers, London, 1997).

-
- [23] H. Qin, S. Yasin and D. A. Williams, "Fabrication and characterization of a SiGe double quantum dot structure," *J. Vac. Sci. Technol. B*, **21**, (2003) 2852.
- [24] E. Cota, R. Aguado and G. Platero, "AC-Driven Double Quantum Dots as Spin Pumps," *AIP Conf. Proc.*, **772**, (2005) 1411.
- [25] S. J. Chorley, J. Frake, C. G. Smith, G. A. C. Jones and M. R. Buitelaar, "Quantized charge pumping through a carbon nanotube double quantum dot," *Appl. Phys. Lett.*, **100**, (2012) 143104.
- [26] O. Astafiev, S. Komiyama and T. Kutsuwa, "Double quantum dots as a high sensitive submillimeter-wave detector," *Appl. Phys. Lett.*, **79**, (2001) 1199.
- [27] B. Trauzettel, A. N. Jordan, C. W. J. Beenakker and M. Büttiker, "Parity meter for charge qubits: An efficient quantum entangler," *Phys. Rev. B*, **73**, (2006) 235331.
- [28] C. Barthel, D. J. Reilly, C. M. Marcus, M. P. Hanson and A. C. Gossard, "Rapid Single-Shot Measurement of a Singlet-Triplet Qubit," *Phys. Rev. Lett.*, **103**, (2009) 160503.
- [29] J. Boviatsis and E. Voutsinas, "Quantum Control and Entanglement of Two Electrons in a Double Quantum Dot Structure," *AIP Conf. Proc.*, **963**, (2007) 740.
- [30] G. Chen, G. Klimeck, S. Datta, G. Chen and W. A. Goddard, "Resonant tunneling through quantum-dot arrays," *Phys. Rev. B*, **50**, (1994) 8035.
- [31] M. J. Hartmann, F. G. S. L. Brandão and M. B. Plenio, "Strongly interacting polaritons in coupled arrays of cavities," *Nature Physics*, **2**, (2006) 849.
- [32] M. Vogl, G. Schaller and T. Brandes, "Criticality in Transport through the Quantum Ising Chain," *Phys. Rev. Lett.*, **109**, (2012) 240402.
- [33] T. H. Oosterkamp, T. Fujisawa, W. G. van der Wiel, K. Ishibashi, R. V. Hijman, S. Tarucha and L. P. Kouwenhoven, "Microwave spectroscopy of a quantum-dot molecule," *Nature*, **395**, (1998) 873.
- [34] M. Eriksson, M. Friesen, S. Coppersmith, R. Joynt, L. Klein, K. Slinker, C. Tahan, P. Mooney, J. Chu and S. Koester, "Spin-Based Quantum Dot Quantum Computing in Silicon," *Quantum Information Processing*, **3**, (2004) 133.
- [35] K. M. Fonseca-Romero, S. Kohler and P. Hänggi, "Coherence Stabilization of a Two-Qubit Gate by ac Fields," *Phys. Rev. Lett.*, **95**, (2005) 140502.
- [36] D. Zueco, F. Galve, S. Kohler and P. Hänggi, "Quantum router based on ac control of qubit chains," *Phys. Rev. A*, **80**, (2009) 042303.

- [37] D. Loss and D. P. DiVincenzo, "Quantum computation with quantum dots," *Phys. Rev. A*, **57**, (1998) 120.
- [38] B. E. Kane, "A silicon-based nuclear spin quantum computer," *Nature*, **393**, (1998) 133.
- [39] D. P. DiVincenzo, "The Physical Implementation of Quantum Computation," *Fortschr. Phys.*, **48**, (2000) 771.
- [40] M. Friesen, P. Rugheimer, D. E. Savage, M. G. Lagally, D. W. van der Weide, R. Joynt and M. A. Eriksson, "Practical design and simulation of silicon-based quantum-dot qubits," *Phys. Rev. B*, **67**, (2003) 121301.
- [41] R. H. Blick, D. Pfannkuche, R. J. Haug, K. v. Klitzing and K. Eberl, "Formation of a Coherent Mode in a Double Quantum Dot," *Phys. Rev. Lett.*, **80**, (1998) 4032.
- [42] D. Vion, A. Aassime, A. Cottet, P. Joyez, H. Pothier, C. Urbina, D. Esteve and M. H. Devoret, "Manipulating the Quantum State of an Electrical Circuit," *Science*, **296**, (2002) 886.
- [43] D. P. DiVincenzo, "Double Quantum Dot as a Quantum Bit," *Science*, **309**, (2005) 2173.
- [44] W. G. van der Wiel, M. Stopa, T. Koder, T. Hatano and S. Tarucha, "Semiconductor quantum dots for electron spin qubits," *New J. Phys.*, **8**, (2006) 28.
- [45] J. R. Petta, A. C. Johnson, J. M. Taylor, E. A. Laird, A. Yacoby, M. D. Lukin, C. M. Marcus, M. P. Hanson and A. C. Gossard, "Coherent Manipulation of Coupled Electron Spins in Semiconductor Quantum Dots," *Science*, **309**, (2005) 2180.
- [46] F. H. L. Koppens, C. Buizert, K. J. Tielrooij, I. T. Vink, K. C. Nowack, T. Meunier, L. P. Kouwenhoven and L. M. K. Vandersypen, "Driven coherent oscillations of a single electron spin in a quantum dot," *Nature*, **442**, (2006) 766.
- [47] Y. Dovzhenko, J. Stehlik, K. D. Petersson, J. R. Petta, H. Lu and A. C. Gossard, "Nonadiabatic quantum control of a semiconductor charge qubit," *Phys. Rev. B*, **84**, (2011) 161302.
- [48] K. D. Petersson, J. R. Petta, H. Lu and A. C. Gossard, "Quantum Coherence in a One-Electron Semiconductor Charge Qubit," *Phys. Rev. Lett.*, **105**, (2010) 246804.
- [49] K. C. Nowack, M. Shafiei, M. Laforest, G. E. D. K. Prawiroatmodjo, L. R. Schreiber, C. Reichl, W. Wegscheider and L. M. K. Vandersypen, "Single-Shot Correlations and Two-Qubit Gate of Solid-State Spins," *Science*, **333**, (2011) 1269.

-
- [50] M. J. Storcz, U. Hartmann, S. Kohler and F. K. Wilhelm, "Intrinsic phonon decoherence and quantum gates in coupled lateral quantum-dot charge qubits," *Phys. Rev. B*, **72**, (2005) 235321.
- [51] C. Emary, "Measuring the entanglement between double quantum dot charge qubits," *Phys. Rev. B*, **80**, (2009) 161309.
- [52] C.-M. Li, L.-Y. Hsu, Y.-N. Chen, D.-S. Chuu and T. Brandes, "Entanglement detection via the condition of quantum correlation," *Phys. Rev. A*, **76**, (2007) 032313.
- [53] G. M. Reuther, D. Zueco, P. Hänggi and S. Kohler, "Monitoring entanglement evolution and collective quantum dynamics," *Phys. Rev. B*, **83**, (2011) 014303.
- [54] C. Kloeffer and D. Loss, "Prospects for Spin-Based Quantum Computing in Quantum Dots," *Ann. Rev. Cond. Mat. Phys.*, **4**, (2013) 51.
- [55] N. Nguyen and S. Das Sarma, "Impurity effects on semiconductor quantum bits in coupled quantum dots," *Phys. Rev. B*, **83**, (2011) 1.
- [56] E. Barnes, J. Kestner, N. T. Nguyen and S. Das Sarma, "Screening of charged impurities with multielectron singlet-triplet spin qubits in quantum dots," *Phys. Rev. B*, **84**, (2011) 235309.
- [57] S. Chorley, G. Giavaras, J. Wabnig, G. Jones, C. Smith, G. Briggs and M. Buiteelaar, "Transport Spectroscopy of an Impurity Spin in a Carbon Nanotube Double Quantum Dot," *Phys. Rev. Lett.*, **106**, (2011) 2.
- [58] H.-K. Lo and S. Popescu, "Classical Communication Cost of Entanglement Manipulation: Is Entanglement an Interconvertible Resource?" *Phys. Rev. Lett.*, **83**, (1999) 1459.
- [59] R. Prevedel, M. Aspelmeyer, C. Brukner, A. Zeilinger and T. D. Jennewein, "Photonic entanglement as a resource in quantum computation and quantum communication," *J. Opt. Soc. Am. B*, **24**, (2007) 241.
- [60] M. H. Anderson, J. R. Ensher, M. R. Matthews, C. E. Wieman and E. A. Cornell, "Observation of Bose-Einstein Condensation in a Dilute Atomic Vapor," *Science*, **269**, (1995) 198.
- [61] K. B. Davis, M. O. Mewes, M. R. Andrews, N. J. van Druten, D. S. Durfee, D. M. Kurn and W. Ketterle, "Bose-Einstein Condensation in a Gas of Sodium Atoms," *Phys. Rev. Lett.*, **75**, (1995) 3969.
- [62] P. W. Courteille, V. S. Bagnato and V. I. Yukalov, "Bose-Einstein Condensation of Trapped Atomic Gases," *Laser Phys.*, **11**, (2001) 659.

- [63] M. Naraschewski, H. Wallis, A. Schenzle, J. I. Cirac and P. Zoller, “Interference of Bose condensates.” *Phys. Rev. A*, **54**, (1996) 2185.
- [64] M. R. Andrews, “Observation of Interference Between Two Bose Condensates,” *Science*, **275**, (1997) 637.
- [65] K. W. Madison, F. Chevy, W. Wohlleben and J. Dalibard, “Vortex Formation in a Stirred Bose-Einstein Condensate,” *Phys. Rev. Lett.*, **84**, (2000) 806.
- [66] J. R. Abo-Shaeer, C. Raman, J. M. Vogels and W. Ketterle, “Observation of vortex lattices in Bose-Einstein condensates.” *Science*, **292**, (2001) 476.
- [67] D. Stamper-Kurn, M. Andrews, A. Chikkatur, S. Inouye, H.-J. Miesner, J. Stenger and W. Ketterle, “Optical Confinement of a Bose-Einstein Condensate,” *Phys. Rev. Lett.*, **80**, (1998) 2027.
- [68] F. Schreck, L. Khaykovich, K. Corwin, G. Ferrari, T. Bourdel, J. Cubizolles and C. Salomon, “Quasipure Bose-Einstein Condensate Immersed in a Fermi Sea,” *Phys. Rev. Lett.*, **87**, (2001) 8.
- [69] T. van Zoest, N. Gaaloul, Y. Singh, H. Ahlers, W. Herr, S. T. Seidel, W. Ertmer, E. Rasel, M. Eckart, E. Kajari, S. Arnold, G. Nandi, W. P. Schleich, R. Walser, A. Vogel, K. Sengstock, K. Bongs, W. Lewoczko-Adamczyk, M. Schiemangk, T. Schuldt, A. Peters, T. Könnemann, H. Müntinga, C. Lämmerzahl, H. Dittus, T. Steinmetz, T. W. Hänsch and J. Reichel, “Bose-Einstein condensation in microgravity.” *Science*, **328**, (2010) 1540.
- [70] D. Jaksch, C. Bruder, J. I. Cirac, C. W. Gardiner and P. Zoller, “Cold Bosonic Atoms in Optical Lattices,” *Phys. Rev. Lett.*, **81**, (1998) 3108.
- [71] M. Greiner, O. Mandel, T. Esslinger, T. W. Hänsch and I. Bloch, “Quantum phase transition from a superfluid to a Mott insulator in a gas of ultracold atoms,” *Nature*, **415**, (2002) 39.
- [72] R. Jördens, N. Strohmaier, K. Günter, H. Moritz and T. Esslinger, “A Mott insulator of fermionic atoms in an optical lattice,” *Nature*, **455**, (2008) 204.
- [73] M. Fisher, P. Weichman, G. Grinstein and D. Fisher, “Boson localization and the superfluid-insulator transition,” *Phys. Rev. B*, **40**, (1989) 546.
- [74] D. Jaksch, H.-J. Briegel, J. Cirac, C. Gardiner and P. Zoller, “Entanglement of Atoms via Cold Controlled Collisions,” *Phys. Rev. Lett.*, **82**, (1999) 1975.
- [75] O. Mandel, M. Greiner, A. Widera, T. Rom, T. W. Hänsch and I. Bloch, “Controlled collisions for multi-particle entanglement of optically trapped atoms,” *Nature*, **425**, (2003) 937.

-
- [76] M. Riebe, H. Häffner, C. F. Roos, W. Hänsel, J. Benhelm, G. P. T. Lancaster, T. W. Körber, C. Becher, F. Schmidt-Kaler, D. F. V. James and R. Blatt, “Deterministic quantum teleportation with atoms,” *Nature*, **429**, (2004) 734.
- [77] C. Roos, G. Lancaster, M. Riebe, H. Häffner, W. Hänsel, S. Gulde, C. Becher, J. Eschner, F. Schmidt-Kaler and R. Blatt, “Bell States of Atoms with Ultralong Lifetimes and Their Tomographic State Analysis,” *Phys. Rev. Lett.*, **92**, (2004) 220402.
- [78] L. Sanchez-Palencia and L. Santos, “Bose-Einstein condensates in optical quasicrystal lattices,” *Phys. Rev. A*, **72**, (2005) 053607.
- [79] V. Ahufinger, L. Sanchez-Palencia, A. Kantian, A. Sanpera and M. Lewenstein, “Disordered ultracold atomic gases in optical lattices: A case study of Fermi-Bose mixtures,” *Phys. Rev. A*, **72**, (2005) 063616.
- [80] D. Clément, A. Varón, M. Hugbart, J. Retter, P. Bouyer, L. Sanchez-Palencia, D. Gangardt, G. Shlyapnikov and A. Aspect, “Suppression of Transport of an Interacting Elongated Bose-Einstein Condensate in a Random Potential,” *Phys. Rev. Lett.*, **95**, (2005) 170409.
- [81] K. V. Krutitsky, A. Pelster and R. Graham, “Mean-field phase diagram of disordered bosons in a lattice at nonzero temperature,” *New J. Phys.*, **8**, (2006) 187.
- [82] V. Yurovsky, A. Ben-Reuven, P. Julienne and C. Williams, “Atom loss and the formation of a molecular Bose-Einstein condensate by Feshbach resonance,” *Phys. Rev. A*, **62**, (2000) 043605.
- [83] S. Kokkelmans, H. Vissers and B. Verhaar, “Formation of a Bose condensate of stable molecules via a Feshbach resonance,” *Phys. Rev. A*, **63**, (2001) 031601.
- [84] D. Stadler, S. Krinner, J. Meineke, J.-P. Brantut and T. Esslinger, “Observing the drop of resistance in the flow of a superfluid Fermi gas,” *Nature*, **491**, (2012) 736.
- [85] C. Jurczak, B. Desruelle, K. Sengstock, J. Y. Courtois, C. I. Westbrook and A. Aspect, “Atomic Transport in an Optical Lattice: An Investigation through Polarization-Selective Intensity Correlations,” *Phys. Rev. Lett.*, **77**, (1996) 1727.
- [86] T. Gericke, P. Würtz, D. Reitz, T. Langen and H. Ott, “High-resolution scanning electron microscopy of an ultracold quantum gas,” *Nature Physics*, **4**, (2008) 949.
- [87] V. A. Brazhnyi, V. V. Konotop, V. M. Pérez-García and H. Ott, “Dissipation-Induced Coherent Structures in Bose-Einstein Condensates,” *Phys. Rev. Lett.*, **102**, (2009) 144101.

- [88] G. Barontini, R. Labouvie, F. Stubenrauch, A. Vogler, V. Guarrera and H. Ott, “Controlling the Dynamics of an Open Many-Body Quantum System with Localized Dissipation,” *Phys. Rev. Lett.*, **110**, (2013) 035302.
- [89] O. Mandel, M. Greiner, A. Widera, T. Rom, T. W. Hänsch and I. Bloch, “Coherent Transport of Neutral Atoms in Spin-Dependent Optical Lattice Potentials,” *Phys. Rev. Lett.*, **91**, (2003) 010407.
- [90] C.-C. Chien and M. Di Ventra, “Controlling transport of ultracold atoms in one-dimensional optical lattices with artificial gauge fields,” *Phys. Rev. A*, **87**, (2013) 023609.
- [91] C.-L. Hung, X. Zhang, N. Gemelke and C. Chin, “Slow Mass Transport and Statistical Evolution of an Atomic Gas across the Superfluid–Mott-Insulator Transition,” *Phys. Rev. Lett.*, **104**, (2010) 160403.
- [92] N. Strohmaier, Y. Takasu, K. Günter, R. Jördens, M. Köhl, H. Moritz and T. Esslinger, “Interaction-Controlled Transport of an Ultracold Fermi Gas,” *Phys. Rev. Lett.*, **99**, (2007) 220601.
- [93] H. Ott, E. de Mirandes, F. Ferlaino, G. Roati, G. Modugno and M. Inguscio, “Collisionally Induced Transport in Periodic Potentials,” *Phys. Rev. Lett.*, **92**, (2004) 160601.
- [94] U. Schneider, L. Hackermüller, J. P. Ronzheimer, S. Will, S. Braun, T. Best, I. Bloch, E. Demler, S. Mandt, D. Rasch and A. Rosch, “Fermionic transport and out-of-equilibrium dynamics in a homogeneous Hubbard model with ultracold atoms,” *Nature Physics*, **8**, (2012) 213.
- [95] S. Palzer, C. Zipkes, C. Sias and M. Köhl, “Quantum Transport through a Tonks-Girardeau Gas,” *Phys. Rev. Lett.*, **103**, (2009) 150601.
- [96] T. Salger, S. Kling, S. Denisov, A. V. Ponomarev, P. Hänggi and M. Weitz, “Tuning the Mobility of a Driven Bose-Einstein Condensate via Diabatic Floquet Bands,” *Phys. Rev. Lett.*, **110**, (2013) 135302.
- [97] M. Cramer, C. M. Dawson, J. Eisert and T. J. Osborne, “Exact Relaxation in a Class of Nonequilibrium Quantum Lattice Systems,” *Phys. Rev. Lett.*, **100**, (2008) 030602.
- [98] C.-C. Chien, M. Zwolak and M. Di Ventra, “Bosonic and fermionic transport phenomena of ultracold atoms in one-dimensional optical lattices,” *Phys. Rev. A*, **85**, (2012) 041601.
- [99] C.-C. Chien and M. Di Ventra, “Dynamical crossover between the infinite-volume and empty-lattice limits of ultra-cold fermions in 1D optical lattices,” *Eur. Phys. Lett.*, **99**, (2012) 40003.

-
- [100] C.-C. Chien, D. Gruss, M. Di Ventura and M. Zwolak, "Interaction-induced conducting / non-conducting transition of ultra-cold atoms in one-dimensional optical lattices," *New J. Phys.*, **15**, (2013) 063026.
- [101] M. Killi and A. Paramekanti, "Use of quantum quenches to probe the equilibrium current patterns of ultracold atoms in an optical lattice," *Phys. Rev. A*, **85**, (2012) 061606.
- [102] M. Bruderer and W. Belzig, "Mesoscopic transport of fermions through an engineered optical lattice connecting two reservoirs," *Phys. Rev. A*, **85**, (2012) 013623.
- [103] D. B. Gutman, Y. Gefen and A. D. Mirlin, "Cold bosons in the Landauer setup," *Phys. Rev. B*, **85**, (2012) 125102.
- [104] J.-P. Brantut, J. Meineke, D. Stadler, S. Krinner and T. Esslinger, "Conduction of Ultracold Fermions Through a Mesoscopic Channel," *Science*, **337**, (2012) 1069.
- [105] J.-P. Brantut, C. Grenier, J. Meineke, D. Stadler, S. Krinner, C. Kollath, T. Esslinger and A. Georges, "A thermoelectric heat engine with ultracold atoms," *Science*, **342**, (2013) 713.
- [106] S. Krinner, D. Stadler, J. Meineke, J.-P. Brantut and T. Esslinger, "Superfluidity with disorder in a thin film of quantum gas," *Phys. Rev. Lett.*, **110**, (2013) 100601.
- [107] A. Ivanov, G. Kordas, A. Komnik and S. Wimberger, "Bosonic transport through a chain of quantum dots," *Eur. Phys. B*, **86**, (2013) 345.
- [108] N. P. Proukakis and B. Jackson, "Finite-temperature models of Bose-Einstein condensation," *J. Phys. B: At. Mol. Opt. Phys.*, **41**, (2008) 203002.
- [109] H. P. Breuer and F. Petruccione, *The Theory of Open Quantum Systems* (Oxford University Press, Oxford, 2002).
- [110] R. K. Wangsness and F. Bloch, "The Dynamical Theory of Nuclear Induction," *Phys. Rev.*, **89**, (1953) 728.
- [111] A. G. Redfield, "On the Theory of Relaxation Processes," *IBM J. Res. Dev.*, **1**, (1957) 19.
- [112] A. G. Redfield, "The Theory of Relaxation Processes," *Adv. Magn. Reson.*, **1**, (1965) 1.
- [113] Y. Zhao and G. H. Chen, "Density matrix negativity for two oscillators in an Agarwal bath," *Phys. Rev. E*, **65**, (2002) 056120.

- [114] S. Stenholm and M. Jakob, "Open systems and time reversal," *J. Mod. Opt.*, **51**, (2004) 841.
- [115] T. Yu, L. Diósi, N. Gisin and W. T. Strunz, "Post-Markov master equation for the dynamics of open quantum systems," *Phys. Lett. A*, **265**, (2000) 331.
- [116] G. Lindblad, "On the generators of quantum dynamical semigroups," *Comm. Math. Phys.*, **48**, (1976) 119.
- [117] M. O. Scully and S. Zubairy, *Quantum Optics* (Cambridge University Press, Cambridge, 1997).
- [118] G. Schaller and T. Brandes, "Preservation of positivity by dynamical coarse graining," *Phys. Rev. A*, **78**, (2008) 022106.
- [119] R. Kubo, "Statistical-Mechanical Theory of Irreversible Processes. I. General Theory and Simple Applications to Magnetic and Conduction Problems," *J. Phys. Soc. Jpn.*, **12**, (1957) 570.
- [120] P. C. Martin and J. Schwinger, "Theory of Many-Particle Systems. I," *Phys. Rev.*, **115**, (1959) 1342.
- [121] H. Araki, D. Kastler, M. Takesaki and R. Haag, "Extension of KMS states and chemical potential," *Comm. Math. Phys.*, **53**, (1977) 97.
- [122] D. Segal, "Nonlinear thermal control in an N -terminal junction," *Phys. Rev. E*, **77**, (2008) 021103.
- [123] G. Schaller, "Quantum equilibration under constraints and transport balance," *Phys. Rev. E*, **83**, (2011) 031111.
- [124] M. Vogl, G. Schaller and T. Brandes, "Counting statistics of collective photon transmissions," *Ann. Phys.*, **326**, (2011) 2827.
- [125] J. L. Skinner and D. Hsu, "Pure dephasing of a two-level system," *J. Phys. Chem.*, **90**, (1986) 4931.
- [126] E. Pazy, "Calculation of pure dephasing for excitons in quantum dots," *Semicond. Sci. Tech.*, **17**, (2002) 1172.
- [127] A. Auffèves, D. Gerace, J.-M. Gérard, M. F. m. c. Santos, L. C. Andreani and J.-P. Poizat, "Controlling the dynamics of a coupled atom-cavity system by pure dephasing," *Phys. Rev. B*, **81**, (2010) 245419.
- [128] G. Schaller, G. Kießlich and T. Brandes, "Transport statistics of interacting double dot systems: Coherent and non-Markovian effects," *Phys. Rev. B*, **80**, (2009) 245107.

-
- [129] L. S. Levitov, H. Lee and G. B. Lesovik, "Electron counting statistics and coherent states of electric current," *J. Math. Phys.*, **37**, (1996) 4845.
- [130] L. Nicolin and D. Segal, "Quantum fluctuation theorem for heat exchange in the strong coupling regime," *Phys. Rev. B*, **84**, (2011) 161414.
- [131] D. A. Bagrets and Y. V. Nazarov, "Full counting statistics of charge transfer in Coulomb blockade systems," *Phys. Rev. B*, **67**, (2003) 085316.
- [132] C. M. Bender, D. C. Brody and B. K. Meister, "Quantum mechanical Carnot engine," *J. Phys. A: Math. Gen.*, **33**, (2000) 4427.
- [133] V. Jaksic and C.-A. Pillet, "Mathematical Theory of Non-Equilibrium Quantum Statistical Mechanics," *J. Stat. Phys.*, **108**, (2002) 787.
- [134] D. Segal and A. Nitzan, "Spin-Boson Thermal Rectifier," *Phys. Rev. Lett.*, **94**, (2005) 034301.
- [135] Y. Rezek, P. Salamon, K. H. Hoffmann and R. Kosloff, "The quantum refrigerator: The quest for absolute zero," *Eur. Phys. Lett.*, **85**, (2009) 30008.
- [136] E. Iyoda, Y. Utsumi and T. Kato, "Nonequilibrium Extension of Onsager Relations for Thermoelectric Effects in Mesoscopic Conductors," *J. Phys. Soc. Jpn.*, **79**, (2010) 045003.
- [137] M. Esposito, R. Kawai, K. Lindenberg and C. Van den Broeck, "Quantum-dot Carnot engine at maximum power," *Phys. Rev. E*, **81**, (2010) 041106.
- [138] M. Esposito and C. Van den Broeck, "Three faces of the second law. I. Master equation formulation," *Phys. Rev. E*, **82**, (2010) 011143.
- [139] H. B. Callen, *Thermodynamics and an Introduction to Thermostatistics*, 2nd edition (John Wiley & Sons, New York, 1985).
- [140] L. Onsager, "Reciprocal Relations in Irreversible Processes. I." *Phys. Rev.*, **37**, (1931) 405.
- [141] L. Onsager, "Reciprocal Relations in Irreversible Processes. II." *Phys. Rev.*, **38**, (1931) 2265.
- [142] K. Saito and Y. Utsumi, "Symmetry in full counting statistics, fluctuation theorem, and relations among nonlinear transport coefficients in the presence of a magnetic field," *Phys. Rev. B*, **78**, (2008) 115429.
- [143] H. B. G. Casimir, "On Onsager's Principle of Microscopic Reversibility," *Rev. Mod. Phys.*, **17**, (1945) 343.

- [144] M. Moreau, “On the derivation of the Onsager relations from the Master equation,” *Lett. Math. Phys.*, **1**, (1975) 7.
- [145] P. Hänggi, “Nonlinear fluctuations: The problem of deterministic limit and reconstruction of stochastic dynamics,” *Phys. Rev. A*, **25**, (1982) 1130.
- [146] M. Apostol, “Generalized theory of thermoelectric figure of merit,” *J. App. Phys.*, **104**, (2008) 053704.
- [147] R. Franz and G. Wiedemann, “Über die Wärmeleitfähigkeit von Metallen,” *Ann. Phys.*, **165**, (1853) 497.
- [148] C. Van den Broeck, “Thermodynamic Efficiency at Maximum Power,” *Phys. Rev. Lett.*, **95**, (2005) 190602.
- [149] F. L. Curzon and B. Ahlborn, “Efficiency of a Carnot engine at maximum power output,” *Am. J. Phys.*, **43**, (1975) 22.
- [150] J. Negele and H. Orland, *Quantum Many-particle Systems*, Advanced Books Classics (Westview Press, Boulder, 2008).
- [151] C. Nietner, G. Schaller, C. Pörtl and T. Brandes, “Dynamics of interacting transport qubits,” *Phys. Rev. B*, **85**, (2012) 245431.
- [152] G. Schaller, G. Kießlich and T. Brandes, “Low-dimensional detector model for full counting statistics: Trajectories, back action, and fidelity,” *Phys. Rev. B*, **82**, (2010) 041303.
- [153] C. Livermore, C. H. Crouch, R. M. Westervelt, K. L. Campman and A. C. Gossard, “The Coulomb Blockade in Coupled Quantum Dots,” *Science*, **274**, (1996) 1332.
- [154] K. Saito, S. Takesue and S. Miyashita, “Thermal conduction in a quantum system,” *Phys. Rev. E*, **54**, (1996) 2404.
- [155] A. M. Chang, “The Kondo Effect and Controlled Spin Entanglement in Coupled Double-Quantum-Dots,” *AIP Conf. Proc.*, **777**, (2005) 100.
- [156] D. I. Tsomokos, M. J. Hartmann, S. F. Huelga and M. B. Plenio, “Entanglement dynamics in chains of qubits with noise and disorder,” *New J. Phys.*, **9**, (2007) 79.
- [157] T. A. Costi and V. Zlatić, “Thermoelectric transport through strongly correlated quantum dots,” *Phys. Rev. B*, **81**, (2010) 235127.
- [158] P. Jordan and E. Wigner, “Über das Paulische Äquivalenzverbot,” *Z. Phys.*, **47**, (1928) 631.

-
- [159] C. D. Batista and G. Ortiz, "Generalized Jordan-Wigner Transformations," *Phys. Rev. Lett.*, **86**, (2001) 1082.
- [160] P. A. Cain, H. Ahmed, D. A. Williams and J. M. Bonar, "Hole transport through single and double SiGe quantum dots," *Appl. Phys. Lett.*, **77**, (2000) 3415.
- [161] E. G. Emiroglu, D. G. Hasko and D. A. Williams, "Isolated double quantum dot capacitively coupled to a single quantum dot single-electron transistor in silicon," *Appl. Phys. Lett.*, **83**, (2003) 3942.
- [162] F. Chi and S.-S. Li, "Current-voltage characteristics in strongly correlated double quantum dots," *J. App. Phys.*, **97**, 123704.
- [163] J. Gorman, D. G. Hasko and D. A. Williams, "Charge-Qubit Operation of an Isolated Double Quantum Dot," *Phys. Rev. Lett.*, **95**, (2005) 090502.
- [164] H. W. Liu, T. Fujisawa, Y. Ono, H. Inokawa, A. Fujiwara, K. Takashina and Y. Hirayama, "Pauli-spin-blockade transport through a silicon double quantum dot," *Phys. Rev. B*, **77**, (2008) 073310.
- [165] P. L. McEuen, E. B. Foxman, U. Meirav, M. A. Kastner, Y. Meir, N. S. Wingreen and S. J. Wind, "Transport spectroscopy of a Coulomb island in the quantum Hall regime," *Phys. Rev. Lett.*, **66**, (1991) 1926.
- [166] J. Weis, R. J. Haug, K. v. Klitzing and K. Ploog, "Transport spectroscopy of a confined electron system under a gate tip," *Phys. Rev. B*, **46**, (1992) 12837.
- [167] D. Pfannkuche and S. E. Ulloa, "Selection Rules for Transport Excitation Spectroscopy of Few-Electron Quantum Dots," *Phys. Rev. Lett.*, **74**, (1995) 1194.
- [168] T. A. Fulton and G. J. Dolan, "Observation of single-electron charging effects in small tunnel junctions," *Phys. Rev. Lett.*, **59**, (1987) 109.
- [169] H. Grabert, M. H. Devoret and North Atlantic Treaty Organization: Scientific Affairs Division, *Single charge tunneling: Coulomb blockade phenomena in nanostructures*, NATO ASI Series: B, Vol. 294, volume 5 (Plenum Press, York, 1992).
- [170] E. Prati, M. D. Michielis, M. Belli, S. Cocco, M. Fanciulli, D. Kotekar-Patil, M. Ruoff, D. P. Kern, D. A. Wharam, J. Verduijn, G. C. Tettamanzi, S. Rogge, B. Roche, R. Wacquez, X. Jehl, M. Vinet and M. Sanquer, "Few electron limit of n-type metal oxide semiconductor single electron transistors," *Nanotechnology*, **23**, (2012) 215204.
- [171] C. Lacroix, "Density of states for the Anderson model," *J. Phys. F: Met. Phys.*, **11**, (1981) 2389.

- [172] Y. Meir, N. S. Wingreen and P. A. Lee, "Transport through a strongly interacting electron system: Theory of periodic conductance oscillations," *Phys. Rev. Lett.*, **66**, (1991) 3048.
- [173] B. Song, D. A. Ryndyk and G. Cuniberti, "Molecular junctions in the Coulomb blockade regime: Rectification and nesting," *Phys. Rev. B*, **76**, (2007) 045408.
- [174] A. Cottet, W. Belzig and C. Bruder, "Positive cross-correlations due to dynamical channel blockade in a three-terminal quantum dot," *Phys. Rev. B*, **70**, (2004) 115315.
- [175] J. Fransson, "Non-equilibrium triplet blockade in parallel coupled quantum dots," *New J. Phys.*, **8**, (2006) 114.
- [176] V. H. Nguyen and V. L. Nguyen, "Coulomb blockade, current and shot noise in parallel double metallic quantum dot structures," *J. Phys.: Condens. Matter*, **19**, (2007) 026220.
- [177] R. Y. Yuan, R. Z. Wang and H. Yan, "Spin-polarized transport in a coupled-double-quantum-dot system with ferromagnetic electrodes," *J. Phys.: Condens. Matter*, **19**, (2007) 376215.
- [178] F. G. S. L. Brandão and M. B. Plenio, "Entanglement theory and the second law of thermodynamics," *Nature*, **4**, (2008) 873 .
- [179] N. A. Peters, T.-C. Wei and P. G. Kwiat, "Mixed-state sensitivity of several quantum-information benchmarks," *Phys. Rev. A*, **70**, (2004) 052309.
- [180] R. F. Werner, "Quantum states with Einstein-Podolsky-Rosen correlations admitting a hidden-variable model," *Phys. Rev. A*, **40**, (1989) 4277.
- [181] A. N. Jordan and M. Büttiker, "Entanglement Energetics at Zero Temperature," *Phys. Rev. Lett.*, **92**, (2004) 247901.
- [182] W. K. Wootters, "Entanglement of Formation of an Arbitrary State of Two Qubits," *Phys. Rev. Lett.*, **80**, (1998) 2245.
- [183] J. Bell, "On the Einstein-Podolsky-Rosen paradox," *Physics*, **1**, (1964) 195.
- [184] L. D. Contreras-Pulido and F. Rojas, "Dynamical entanglement formation and dissipation effects in two double quantum dots," *J. Phys.: Condens. Matter*, **18**, (2006) 9771.
- [185] M. Steffen, M. Ansmann, R. C. Bialczak, N. Katz, E. Lucero, R. McDermott, M. Neeley, E. M. Weig, A. N. Cleland and J. M. Martinis, "Measurement of the Entanglement of two superconducting Qubits via State Tomography," *Science*, **313**, (2006) 1423.

-
- [186] C. Nietner, G. Schaller and T. Brandes, "Transport with ultra-cold atoms at constant density," *Phys. Rev. A*, **89**, (2013) 013605.
- [187] C. Nietner and A. Pelster, "Ginzburg-Landau theory for the Jaynes-Cummings-Hubbard model," *Phys. Rev. A*, **85**, (2012) 043831.
- [188] G. B. Arfken, H. J. Weber and F. E. Harris, *Mathematical methods for Physicists*, 7th edition (Academic Press, Oxford, 2013).
- [189] D. Bednarczyk and J. Bednarczyk, "The Approximation of the Fermie-Dirac integral $F_{1/2}$," *Phys. Lett. A*, **64**, (1978) 409.
- [190] X. Aymerich-Humet, F. Serra-Mestres and J. Millán, "An analytic approximation for the Fermi-Dirac integral $F_{3/2}$," *Solid-State Electron.*, **24**, (1981) 981.
- [191] J. S. Blakemore, "Approximations for Fermi-Dirac integrals, especially the function $F_{1/2}$ used to describe electron density in a semiconductor," *Solid-State Electronics*, **25**, (1982) 1067.
- [192] X. Aymerich-Humet, F. Serra-Mestres and J. Millán, "A generalized approximation of the Fermi-Dirac integrals," *J. App. Phys.*, **54**, (1983) 2850.
- [193] M. Taher and A. Atti, "Approximations for Fermi-Dirac integrals $F_j(x)$," *Solid-State Electron.*, **37**, (1994) 1677.
- [194] S. Biswas and D. Jana, "Thermodynamics of quantum gases for the entire range of temperature," *Eur. J. Phys.*, **33**, (2012) 1527.
- [195] U. Harbola, M. Esposito and S. Mukamel, "Quantum master equation for electron transport through quantum dots and single molecules," *Phys. Rev. B*, **74**, (2006) 235309.
- [196] C. W. J. Beenakker, "Theory of Coulomb-blockade oscillations in the conductance of a quantum dot," *Phys. Rev. B*, **44**, (1991) 1646.
- [197] M. Esposito, K. Lindenberg and C. Van den Broeck, "Universality of Efficiency at Maximum Power," *Phys. Rev. Lett.*, **102**, (2009) 130602.
- [198] M. Esposito, K. Lindenberg and C. V. den Broeck, "Thermoelectric efficiency at maximum power in a quantum dot," *Eur. Phys. Lett.*, **85**, (2009) 60010.
- [199] C. Van den Broeck and K. Lindenberg, "Efficiency at maximum power for classical particle transport," *Phys. Rev. E*, **86**, (2012) 041144.
- [200] M. P. A. Fisher, G. Grinstein and S. M. Girvin, "Presence of quantum diffusion in two dimensions: Universal resistance at the superconductor-insulator transition," *Phys. Rev. Lett.*, **64**, (1990) 587.

- [201] L. Pitaevskii and S. Stringari, *Bose-Einstein Condensation*, International Series of Monographs on Physics (Oxford University Press, Oxford, 2003).
- [202] J. Fransson and O. Eriksson, "Asymmetric negative differential conductance in double quantum dots," *J. Phys.: Condens. Matter*, **16**, (2004) L85.
- [203] V. H. Nguyen, V. L. Nguyen and H. N. Nguyen, "Negative differential conductance in metallic double quantum dot structures," *J. Phys.: Condens. Matter*, **17**, (2005) 1157.
- [204] J. C. Chen, A. M. Chang and M. R. Melloch, "Transition between Quantum States in a Parallel-Coupled Double Quantum Dot," *Phys. Rev. Lett.*, **92**, (2004) 176801.
- [205] L.-J. Wang, G.-P. Guo, D. Wei, G. Cao, T. Tu, M. Xiao, G.-C. Guo and A. M. Chang, "Gates controlled parallel-coupled double quantum dot on both single layer and bilayer graphene," *Appl. Phys. Lett.*, **99**, 112117.

List of figures

1.1	Quantum dots defined in a $2D$ electron gas and a InSb nanowire.	2
1.2	Bose-Einstein condensate and transport setup for ultracold atoms. . .	4
2.1	Sketch of the system-bath decomposition.	7
2.2	Sketch of a multi-terminal setup.	20
3.1	Coupled double-quantum dots with charge impurity.	40
3.2	Steady-state currents.	47
3.3	Differential steady-state currents.	48
3.4	IV -plot of the steady-state currents.	55
3.5	Gap between the Coulomb diamonds versus the CQB parameters. . . .	57
3.6	Position of the Coulomb diamond gap versus the CQB parameters. . .	58
3.7	Purity of the steady-state density matrix.	60
3.8	Purity of the CQB for $U_x/U_\perp = 1$	61
3.9	Purity of the CQB for $U_x/U_\perp = 0.7$	62
3.10	Concurrence plots.	64
4.1	Conventional mean occupations.	69
4.2	Temperature dependence of the chemical potential	71
4.3	Mean occupation with dependent chemical potential	72
4.4	Bosonic ground-state occupation	75
4.5	Fermionic transport setup	76
4.6	Fermionic steady-state currents for constant particle density.	83
4.7	Sketch of the Fermi statistics for different fixed temperatures.	84
4.8	Fermionic matter conductance.	87
4.9	Fermionic heat conductance.	89
4.10	Fermionic analog to the thermopower	91
4.11	Fermionic figure-of-merit	93
4.12	Fermionic efficiency at maximum power	95
4.13	Bosonic transport setup	97
4.14	Bosonic steady-state currents for constant particle density.	102
4.15	Bosonic matter conductance.	105
4.16	Bosonic heat conductance.	107
4.17	Bosonic analog to the thermopower	109
4.18	Bosonic figure-of-merit	110
4.19	Bosonic efficiency at maximum power	111

Acknowledgements

Scientific research, and especially such a copious one like a doctoral thesis, is never the work of a single person. Therefore, at this point I want to take the opportunity to express my greatest gratitude to the people that enabled me to compile this thesis.

First of all, I would like to thank my honorific supervisor Prof. Dr. Tobias Brandes for his scientific advice and his constant and patient support over the last three years. I am very thankful for all the interesting and constructive discussions and for always motivating me to pursue my own ideas. Without his encouraging and inspiring care this work could not have been done. He also offered me the opportunity to visit numerous conferences and workshops and discuss my ideas with many scientific visitors of international renown.

Moreover, I want to thank Dr. Gernot Schaller who taught me a lot about master equations and full-counting statistics, and always took time to discuss my questions and problems. His countless stimulating suggestions and ideas greatly influenced the direction and results of my research.

Additionally, I am grateful to Prof. Dr. Andreas Wacker who agreed to be the second referee of this thesis, and to Prof. Dr. Otto Dopfer who agreed to be the chairman of my thesis defense.

Furthermore, I would like to thank all the people of our group and the Institute of Theoretical Physics at the Technische Universität Berlin. Especially, the former members Dr. Malte Vogl and Dr. Christina Pölt with whom I had a lot of very enlightening discussions about transport master equations and full-counting statistics, and Dr. Anja Metelmann, who did not only support me with her advice but also with a lot of relaxing coffee breaks and some social distractions.

Also, I want to express my deep appreciation to Dr. Victor Bastidas, who was the most comfortable room mate I could imagine, Mathias Hayn, who knows me for quite some years now and always has been a supportive, reliable and incentive fellow student, and Wassilij Kopylov and Philipp Strasberg for proofreading this thesis. Of course, I also thank all of my other colleagues for their interesting discussions and for providing such a pleasant and inspiring atmosphere in our group.

Last but not least, I thank the GRK 1558 and the SFB 910 for their financial support of this thesis.